Peptide-Based Molecular Transformations for Tuning the Structure and Properties of Chiral Gold Nanoparticle Single Helices

by

Soumitra Mokashi Punekar

B.Sc., University of Delhi, 2012

M.Sc., Indian Institute of Technology Bombay, 2014

Submitted to the Graduate Faculty of

The Kenneth P. Dietrich School of Arts and Sciences in partial fulfillment

of the requirements for the degree of

Doctor of Philosophy

University of Pittsburgh

2019

UNIVERSITY OF PITTSBURGH

DIETRICH SCHOOL OF ARTS AND SCIENCES

This dissertation was presented

by

Soumitra Mokashi Punekar

It was defended on

July 29, 2019

and approved by

W. Seth Childers, Assistant Professor, Department of Chemistry

Haitao Liu, Associate Professor, Department of Chemistry

Tiffany Walsh, Professor, Institute of Frontier Materials, Deakin University

Thesis Advisor: Nathaniel L. Rosi, Professor, Department of Chemistry

Peptide-Based Molecular Transformations for Tuning the

Structure and Properties of Chiral Gold Nanoparticle Single Helices

Soumitra Mokashi Punekar, PhD

University of Pittsburgh, 2019

Helical gold nanoparticle (AuNP) superstructures have generated tremendous research interest due to wide-ranging applications in metamaterial optics, chiral sensing, detection, and several other fields. These optical materials consist of plasmonic AuNPs arranged in a helical topology, giving rise to unique chiroptical properties that depend on the structural parameters of the helix. This dissertation describes advances in systematically modulating the structural features and consequently adjusting the chiroptical properties of single-helical AuNP superstructures. The modifications to the single-helical nanoscale architecture are achieved via small molecular transformations within a gold-binding peptide assembly agent, and in one case, addition of external additives.

Specifically, in Chapter 2, I present a rational strategy to adjust the helical pitch of AuNP single helices by tuning the aliphatic tail length within a family of peptide conjugate molecules. I demonstrate that the helical pitch increases and the chiroptical signal intensity decreases with an increase in aliphatic tail length. In Chapter 3, I focus on the N-terminus amino acid segment within the peptide sequence as means of further adjusting assembly metrics and helical pitch length. Via a single amino acid mutation within a class of peptide conjugates, I achieve an overall decrease in the average helical pitch of single-helical superstructures. Chapter 4 describes the adjustment of particle size within single-helical superstructures by tuning peptide-NP interaction via C-terminus

peptide sequence modification. Key amino acid-NP interactions are identified, via theoretical simulations, that ultimately affect the size of component particles within helical superstructures. These molecular alterations yield single helices comprising larger particles that exhibit intense chiroptical signal. Finally, in Chapter 5, I screen a series of cetyltrimethylammonium bromide (CTAB) analogs to control the shape of constituent particles within helical superstructures. I outline selection criteria (CTAB tail length and concentration) necessary for the deliberate conversion of small particles within the single-helical superstructures to anisotropic (prisms and polygonal) particles.

Overall, the advances presented in this dissertation highlight multiple levels of control over the nanoscale architecture and properties of one particular type of chiral superstructures. This is a significant step in constructing designed chiral NP assemblies which are essential for serving myriad potential applications.

Table of Contents

List of Tables

List of Figures

Preface

As I think back to all my years of being a student, I feel a deep sense of gratitude for all the people and opportunities that in ways, big and small, have impacted my academic journey so far. Graduate school in particular has been a truly remarkable experience. I would like to take this opportunity to thank those individuals who have helped me develop an interest in science and also helped me navigate through the sudden turns and unexpected twists of life.

First, I want to extend my heartfelt gratitude and deepest thanks to my advisor, Prof. Nat Rosi. Nat is truly an outstanding mentor and a visionary scientist. He has been instrumental in my growth as a researcher, and has had a huge impact on my scientific writing. Nat has a kind heart and always wishes the best for his students. I am extremely grateful for his guidance and support over the years.

I have benefited greatly from my dissertation committee members: Prof. Haitao Liu, Prof. Seth Childers, and Prof. Tiffany Walsh. Through their interesting scientific questions, I have had the opportunity to think more deeply about my research. Prof. Tiffany Walsh has been an outstanding collaborator. It has been a real pleasure to work with her.

I would like to thank the many current and past members of the Rosi research group who have always supported me. Dr. Andrea Merg and Dr. Chong Liu were senior graduate students when I joined the group. They laid out an outstanding blueprint for how to be successful in graduate school. Tianyi Luo is one of the most intelligent graduate students I have ever met. His work ethic and scientific temperament are unparalleled. Yicheng Zhou, Patrick Muldoon, Zack Schulte, Sydney Brooks, Mattheus De Souza, Yeon Kwon, and Camera Hogan are great colleagues. It has been an awesome experience working with all of them.

In addition to people I interacted with during my PhD, I would like to acknowledge the teachers and professors from India who helped me cultivate an interest in science. These people are the reason I pursued a PhD in chemistry. Prof. K. V. Srikanth is the smartest professor I have encountered. He has been a terrific mentor through the years. I will always be grateful for his support. I loved my chemistry courses at IIT Bombay and at the University of Delhi and I am grateful to so many professors at these institutions. Prof. Gharpure and Prof. Kaliappan at IIT Bombay, and Prof. Anju Srivastav and Prof. C. K. Seth at the University of Delhi are very inspiring professors. Lastly, I want to thank my high school teachers from Kendriya Vidyalaya and mentors Dr. Mrinmoy Saha and Dr. Sourav Das who at very early stages helped me appreciate and understand fundamental chemistry.

Words of thanks do not even compare to how indebted I feel to my family. My parents, Ravi and Rohini Mokashi Punekar, provided me and my sister with a very happy childhood and countless opportunities. My parents always encouraged me to find joy in what I was learning and studying. Since my late teens, I have envisioned that one day I too could be a professor like them. They are my source of inspiration and a guiding light to help me stay humble and be kind. For the last five years, while in Pittsburgh, we have communicated via video calls. Every day, I wish I lived closer to them. My sister, Prachi Mokashi, and my brother-in-law, Rohit Iyer, are both film makers. They introduced me to many eye-opening movies, documentaries, and TV shows. My sister always makes it a point to check on me and continues to treat me like her baby brother. I feel extremely blessed and fortunate to have all of them in my life. I hope I give back at least one percent of what they do for me. I love them all so much!

Finally, I would like to thank a very special person that I met during graduate school. Haley Grimm (soon to be Dr. Grimm) is a fellow chemistry graduate student and an exceptional young scientist. Haley not only helped me with my science but also introduced me to so many things outside the lab. If not for her, I would not be the biggest Indian fan of American football and I also wouldn't have experienced many aspects of American culture. I am also very thankful to her parents, Bruce and Janice Grimm, for always making me feel welcome. Haley has been my constant source of support and I am so fortunate to have her in my life. I love you, Haley!

My time in Pittsburgh is filled with so many great memories. It's a great city to live in and has a very unique culture. The chemistry department has become my second home in Pittsburgh. I came here not knowing too much about the department and now I find myself very much a part of its fabric. It has been an incredible journey and I will always cherish my time at the University of Pittsburgh. H2P!

1.0 Introduction

This chapter, written in collaboration with Sydney C. Brooks, Yicheng Zhou, and Nathaniel L. Rosi*, is part of a *review article in preparation*.

1.1 Plasmonic Chirality

The concept of chirality and symmetry has long been a fascinating subject for a diverse range of disciplines. Chiral objects are defined as non-superimposable conformations that are mirror images of each other-much like a pair of left and right hands. In fact, the word chiral derives from the Greek χειρ (kheir), which translates to "hand". From a biological standpoint, the majority of the biomolecules in living beings exist only in one particular configuration (**Figure 1**). For example, amino acids within large protein and peptide molecules exist only in the L-form (left-handed).

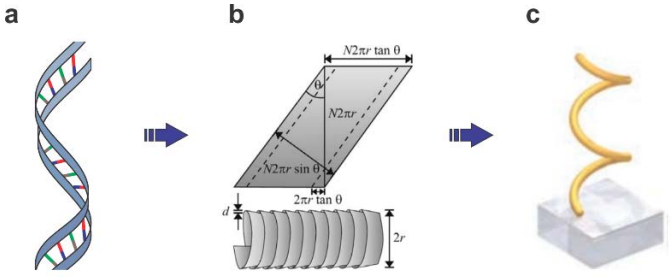

Figure 1. Comparison between biomolecular chirality and nanomaterial chirality. (a) Cartoon representation of a chiral double stranded DNA molecule that exhibits helical morphology. (b) Conceptual design of an artificial chiral helical metamaterial as envisioned by Pendry in 2004. Image adapted with permission from ref. 2. Copyright 2004 American Association for the Advancement of Science (AAAS). (c) Top-down lithographic construction of a chiral gold helix. Image adapted with permission from ref. 3. Copyright 2009 AAAS.

It has long been considered that the phenomenon of homochirality (predominant occurrence of one configuration) could also be linked to the origin of life.[1] These phenomena have inspired chemists and biologists to isolate, synthesize, and study the properties of chiral molecules, termed enantiomers.

Compared to molecular chirality, plasmonic chirality is a relatively new research discipline and falls under the broad umbrella of materials chemistry. Research interest in chiral metallic structures has escalated rapidly since the early 2000s due to visionary papers that either predicted or demonstrated the potential applications of these materials.[2,3] For example, in 2004, Pendry reported that chiral metamaterials could be used to achieve negative refraction (**Figure 1**).[2] Following this seminal work, other reports showed that chiral metamaterials lead to circular dichroism (CD),[4] negative phase velocities,[5] and intense gyrotropy.[6] These properties can be harnessed to build a library of optical materials including 'perfect lenses',[7] circular polarizers,[3] chiroptical sensors,[8] and negative refractive index metamaterials.[9,10] In addition to these optical applications, chiral metallic structures have recently been explored as materials for the detection of biomolecular disease precursors,[11] chiral catalysis,[12] and chiral separation.[13] Methods of synthesizing plasmonic chiral materials and ways of tuning their properties continue to be an exciting research challenge.

1.2 Chiral Nanoparticle Assemblies and Chiroptical Properties

Chiral metallic structures can be constructed either via top-down lithography or bottom-up synthesis. Bottom-up synthesis entails the assembly of individual achiral nanoparticles (NPs) into chiral configurations and is ideal for constructing chiral metallic NP assemblies due to high

synthetic tunability, programmability, and optimal cost. Before highlighting the various chiral geometries that have been constructed from the bottom up, I discuss below the properties of individual metallic NPs and the circular dichroism property associated with chiral NP assemblies.

1.2.1 Localized Surface Plasmon Resonance and Circular Dichroism

At the nanoscale, individual metallic particles (e.g. gold NPs (AuNPs)) exhibit unique optical properties due to i) higher surface to volume ratio, and ii) the geometric confinement of electrons. Localized surface plasmon resonance (LSPR) is one of the hallmark properties of metallic NPs.[14] LSPR is the condition of resonant oscillation of surface electrons on a NP, achieved when the frequency of incident photons equals the natural frequency of oscillating surface electrons. In addition to the size, shape, composition, and dielectric environment of the metallic NP,[15,16] the LSPR also depends on their assembly/aggregation state.[17] Therefore, when metallic NPs are arranged in a chiral geometry, the coupling of individual plasmons leads to collective plasmon oscillation across the overall chiral architecture.[18]

Circular dichroism (CD) spectroscopy is a form of light absorption spectroscopy. It is used for detecting and differentiating between two chiral enantiomeric species. Enantiomers with opposite chirality interact differently with left-handed and right-handed circularly polarized light. This differential absorption, termed as CD, can either be negative or positive depending on the extent of absorption of left-handed versus right-handed circularly polarized light. Most chiral molecules exhibit weak CD signals that typically lie in the UV region. This property makes the detection of chiral molecules more challenging. In contrast to molecular chirality, plasmonic chiral assemblies can exhibit enhanced optical chirality in the visible region at the frequency of the LSPR (**Figure 2**).[18,19] Chiral NP assemblies, wherein the coupled plasmons oscillate along the chiral

architecture, exhibit differential absorption of left and right-handed circularly polarized light. In general, the figure of merit used to assess, measure, and compare the chiroptical response of chiral NP assemblies is the *g*-factor (anisotropy factor).[20,21,22] The *g*-factor is defined as the ratio of the molar circular dichroism to the molar extinction and is used extensively to compare the optical activity of various chiral systems. It is important to note that the *g*-factor is an intensive property and therefore independent of the sample concentration and the path length of the cuvette used for measurements.

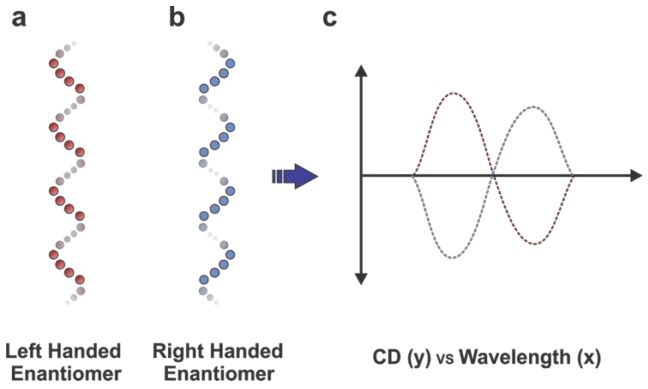

Figure 2. Chiral plasmonic NP assemblies interact differently with circularly polarized light. (a) Cartoon representation of (a) left-handed helical NP assembly shown in red, and (b) right-handed helical NP assembly, shown in blue. (c) CD signature of the chiral NP assemblies differ based on their handedness (red curve: left-handed helix, blue curve: right-handed helix).

In light of these properties and several potential applications, research groups have developed synthetic methods aimed at the construction of chiral plasmonic materials. Below, I highlight the major accomplishments in the synthesis of various chiral morphologies, with special emphasis on helical NP superstructures and their properties.

1.2.2 Pioneering Work on the Synthesis of Chiral Nanomaterials and Theoretical Investigations into their Chiroptical Properties

To my knowledge, Mann et al., in 1996, reported one of the earliest examples of a chiral NP assembly.[23] They demonstrated that AuNPs could be helically templated onto biolipid tubules. However, the AuNPs were not very well-ordered. In 2002, Stupp and coworkers used organic templates to nucleate and grow well-ordered CdS helices.[24] Fu et al. described the synthesis of double-helical arrays of AuNPs on peptide fibrils in 2003.[25] In 2008, the Rosi laboratory developed an assembly platform for preparing helical NP superstructures. As a first example of the NP assembly strategy, they showed that designed peptide conjugate molecules can direct the synthesis and assembly of well-defined double-helical AuNP assemblies.[26]

Since those early studies, numerous chiral NP geometries have been reported.[27-32] Nucleic acids are often used to direct the assembly of NPs into chiral configurations.[33] For example, in 2009, Yan and coworkers used DNA tubules to form left-handed helices of AuNPs[34] while Alivisatos and coworkers used nucleic acids to link AuNPs into an asymmetric chiral NP tetrahedron.[27] One of the first papers to experimentally study the chiroptical properties of these materials was published by Kotov and coworkers in 2009.[35] In this report, they used a DNA polymerization approach to construct chiral trimers and tetramers that exhibited chiroptical CD response (**Figure 3**).

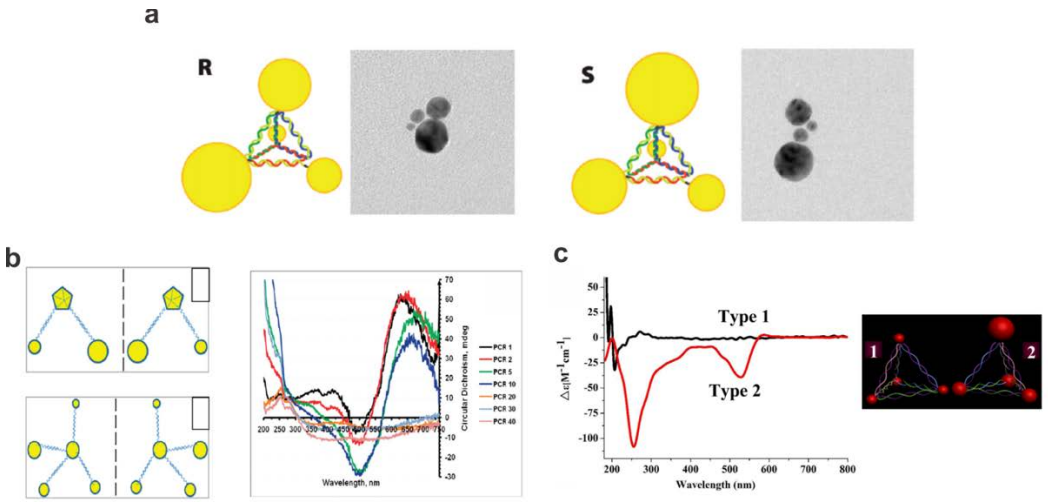

Figure 3. Examples of non-helical chiral AuNP assemblies. (a) Construction of R/S chiral pyrimidal architectures of spherical AuNPs assembled using DNA strands. Images adapted with permission from ref. 27. Copyright 2009 American Chemical Society. (b) Chiral trimer and tetramer assemblies of AuNPs, organized via DNA polymerase chain reaction, that exhibit plasmonic chirality. Images adapted with permission from ref. 35. Copyright 2009 American Chemical Society. (c) CD profile of chiral pyramidal AuNP assemblies. Images adapted with permission from ref. 31. Copyright 2012 American Chemical Society.

Theoretical investigations describing the plasmonic chiroptical properties of chiral NP assemblies have proceeded in parallel with the experimental studies and serve as a basis for interpreting experimental data and designing new structures with optimized properties.[18,19,36] Govorov and coworkers have shown that intense CD signals are observed for NPs arranged in a helical fashion and that the CD signature of helical assemblies depends on the assembly geometry and NP composition.[37] Specifically, these studies establish that i) helix pitch and helix radius, ii) number of particles per helical turn, and iii) particle dimensions (size and shape) all influence the chiroptical readout. These theoretical studies, in concert with experimental advances in NP assembly, have helped propel this field of study forward.

1.2.3 Helical NP Assemblies (2010-2015)

Following the theoretical studies on the chiroptical properties of helical NP assemblies, synthetic efforts to construct these materials moved to the forefront (**Figure 4**). In 2011, Liz-Marzan's group showed that gold nanorods could be arranged onto chiral helical fibers composed of self-assembled chiral anthraquinone-based oxalamide molecules.[21] The nanorods were attached onto the fibers via non-covalent interactions. In this case, the handedness of the self-assembled fibers was controlled via the chirality of the anthraquinone-based assembly agent. These helical assemblies exhibit very intense chiroptical signal with large *g*-factor values. Concurrently, Ding and coworkers demonstrated that AuNP helices could be fabricated by first assembling two parallel AuNP one-dimensional chains on DNA origami sheets followed by rolling up the sheets via the introduction of short folding DNA strands.[38] They further revealed that the yield and spatial organization of the AuNPs on the DNA origami sheets improved by using smaller particle sizes. Chen and coworkers, also in 2011, synthesized double-helical assemblies of Au-Ag alloy nanowires starting from Au-Ag nanowires.[39] Upon introducing external metal ions (Pd^{2+}, Pt^{2+}, Au^{3+}) to pre-synthesized Au-Ag nanowires, they observed winding of nanowires to produce double-helical architectures. This was a unique demonstration wherein chiral helical nanostructures composed of two different plasmonic metals were synthesized. In 2012, Leidl and coworkers reported the first example of using DNA origami to template the assembly of AuNPs into both left and right-handed chiral single helices.[40] *g*-factor equal to 0.025 was reported in this paper. Multiple additional origami-based methods have since been reported.[32,41-43] In 2014, Klajn's group demonstrated that large arrays of magnetite nanocrystals could be self-assembled into helical superstructures in a template-free manner.[44] The formation of template free helical superstructures comprising magnetite nanocrystals is attributed to both van der Waals forces and

magnetic dipole interactions. Interestingly, since the helices are assembled on a solid substrate, neighboring helices adopt similar handedness to achieve maximum packing efficiency. In 2015, the Kotov lab reported yet another method of influencing the handedness of helical NP assemblies. They prepared self-assembled CdTe twisted nanoribbons where the handedness of the ribbon was controlled by circularly polarized light.[45] Left-handed circularly polarized light lead to the formation of left-handed CdTe nanoribbons while right-handed circularly polarized light lead to the formation of right-handed CdTe nanoribbons. In addition to these methods, several other assembly approaches for constructing helical nanostructures have emerged including polymer,[46,47] mechanical confinement,[48] and inorganic/organic scaffold-based methods.[49]

In 2013, the Rosi group further expanded on their NP assembly platform for adjusting the structure and properties of AuNP double helices.[50] They developed a diverse family of AuNP double-helical superstructures by employing designed peptide-conjugate molecules that differed in the chirality of the component amino acids. Peptide conjugates containing L-amino acids direct the assembly of left-handed double helices while conjugates containing D-amino acids direct the assembly of right-handed double helices. Further, the right-handed and left-handed double helices exhibit mirror-image CD signatures. This report was the first example to demonstrate that the molecular structure of peptide conjugate molecules could be adjusted to tailor the structure and properties of helical superstructures. In the subsequent sections, I describe in detail, the peptide-based assembly strategy for constructing AuNP helical superstructures.

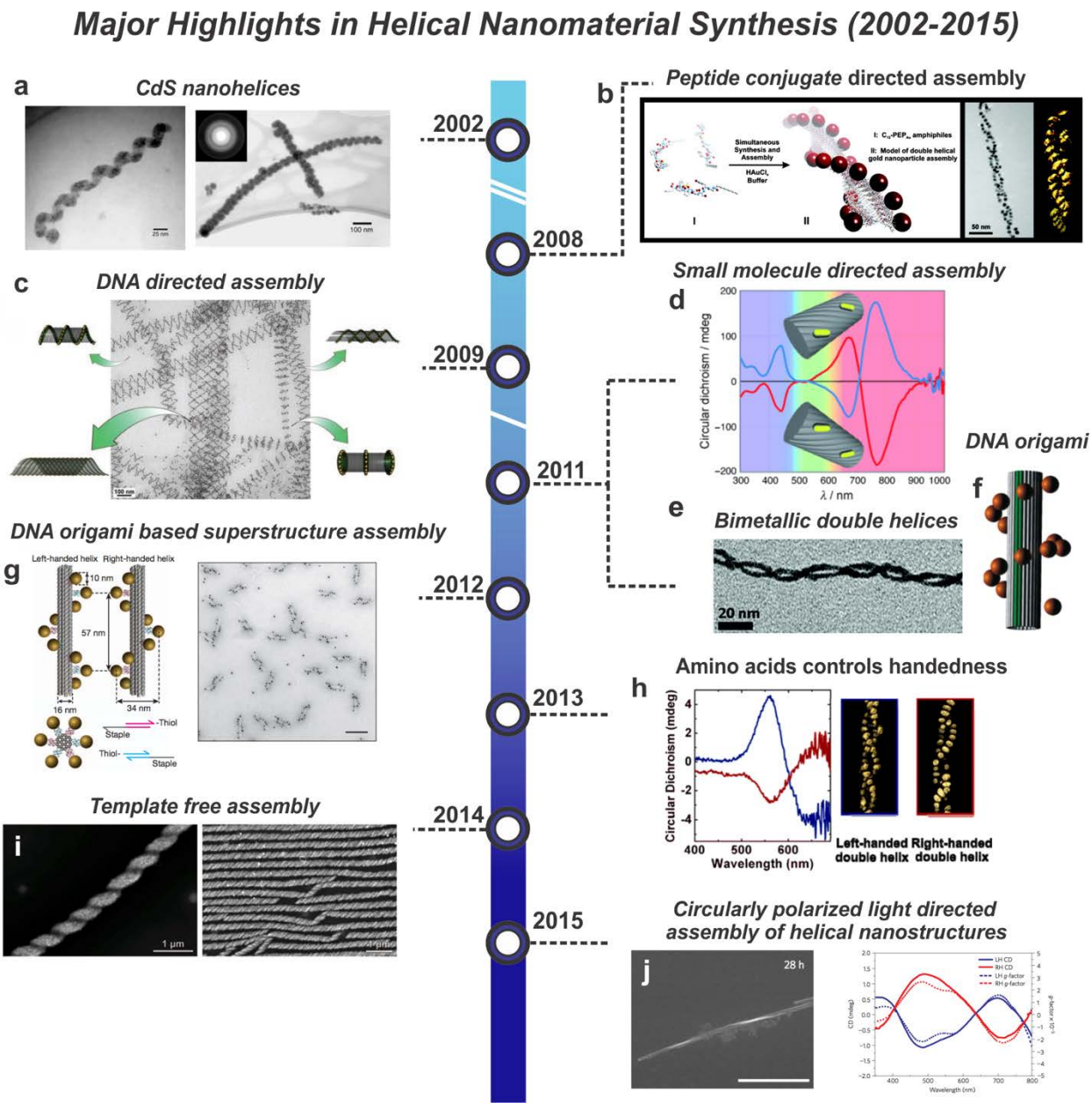

Figure 4. Major highlights in the synthesis of helical nanostructures between 2002-2015. (a) TEM images of CdS helical assemblies assembled on dendron rodcoils. Images adapted with permission from ref. 24. Copyright 2002 Wiley. (b) TEM image and electron tomography of double-helical assemblies of AuNPs assembled via designed peptide conjugates. Images adapted with permission from ref. 26. Copyright 2008 American Chemical Society. (c) TEM images reveal helical AuNP superstructures assembled using DNA tiles. Images adapted with permission from ref. 34. Copyright 2009 AAAS. (d) Gold nanorods templated on oxalimide-based fibers yield helical superstructures where control over handedness is dictated by the chirality of oxalimide assembly agent. Images adapted with

permission from ref. 21. Copyright 2011 Wiley. (e) Bimetallic nanowire double helices consisting of Au-Ag alloy. Images adapted with permission from ref. 39. Copyright 2011 American Chemical Society. (f) AuNP single helices constructed using DNA origami sheets. Images adapted with permission from ref. 38. Copyright 2011 American Chemical Society. (g) DNA origami is employed to control the handedness and chiroptical properties of AuNP single helices. Images adapted with permission from ref. 40. Copyright 2012 Nature Publishing Group. (h) Construction of left-handed and right-handed AuNP double helices using peptide conjugates. The structure and chiroptical proeprties are controlled via the chirality of the amino acids. Images adapted with permission from ref. 50. Copyright 2013 American Chemical Society. (i) Template-free assembly of magnetite nanocrystals into helical superstructures. Images adapted with permission from ref. 44. Copyright 2014 AAAS. (j) CdTe nanohelices prepared using circularly polarized light. The chirality of the nanohelices is controlled via the handedness of the circularly polarized light. Images adapted with permission from ref. 45. Copyright 2015 Nature Publishing Group.

1.3 Peptide-Based Method for Assembling Helical NP Superstructures

The NP assembly methodology developed by the Rosi group derives from two related research disciplines: i) peptide self-assembly, achieved via sequence manipulation and tuning peptide constitution, and ii) peptide-based NP synthesis, which relies on exploiting peptide sequences, discovered via *in vitro* evolution, that recognize and bind inorganic surfaces.

1.3.1 Peptide Assembly and Inorganic Surface Recognition

Peptides exhibit unique primary sequence-dependent self-assembly. Several covalent and non-covalent interactions such as disulfide linkages, hydrogen bonding, π-π stacking, electrostatic and hydrophobic interactions can exist between the constituent amino acids. The nature of these forces influence the secondary structure (e.g. α-helices, β-sheet) of peptides as well as promote

their self-assembly.[51,52] Peptide assembly can also be affected by modifying either the N- or C-termini with hydrophobic groups. Peptide conjugate molecules that consist of hydrophilic peptide sequences tethered to a hydrophobic group, such as a fatty acid chain, can self-assemble in aqueous media.[53] Over the years, several supramolecular self-assembled architectures (e.g. fibers, micelles, tubes, sheets) have been achieved by adjusting the molecular structure of peptide conjugate molecules (**Figure 5**).[54,55]

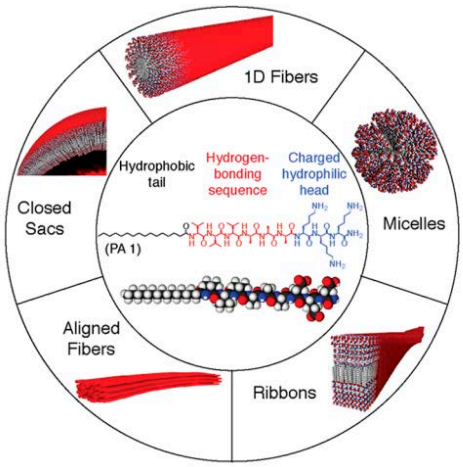

Figure 5. Molecular structure of peptide conjugate molecules can be adjusted to access various self-assembled architectures. Images adapted with permission from ref. 55. Copyright 2017 American Chemical Society.

In 2001, the Stupp lab reported the first example of a peptide conjugate molecule capable of forming supramolecular fibrous nanostructures. This system consisted of a hydrophilic peptide sequence containing cysteine residues attached to a hydrophobic aliphatic tail.[53] These molecules self-assemble at specific pH values due to intermolecular hydrophobic interactions as well as intermolecular disulfide linkages. The Gazit group, in 2003, reported self-assembled peptide nanotubes formed from diphenylalanine.[56] Formed via hydrogen-bonding and aromatic side-chain interactions, the nanotubes were used as scaffold materials for casting silver nanowires. Several other supramolecular morphologies including vesicles, nanofibers have been assembled using the

diphenylalanine building unit.[57] These assemblies have a variety of applications in bioimaging, drug delivery, and sensing.[57] Amyloid peptides, that form neuretic plaque associated with neurodegenerative diseases such as Alzheimer's disease, self-assemble into fibers in aqueous media.[58,59,60] Research groups have conducted extensive work on understanding their self-assembly pathway. For example, Lynn and coworkers have reported that short fragments of Alzheimer's disease-causing peptides such as CH_3CO-KLVFFAE-NH_2 form fiber assemblies in aqueous solution due to electrostatic and hydrogen bonding interactions.[61] These studies provide new insights into the origins and causes of several neurodegenerative diseases. Stimuli-responsive peptide-based nanomaterials have also been developed. Adams and coworkers have demonstrated that the gelation of naphthalene-functionalized dipeptide molecules can be controlled chemically by introducing a lactone-based small molecule trigger.[62] Stupp and coworkers have reported peptide amphiphile assemblies consisting of photo-labile moiety, 2-nitrobenzyl, that exhibit reconfigurable self-assembled morphologies upon exposure to light.[63] Finally, the Ulijn group has shown the formation of transient conducting nanostructures formed from naphthalene diimide tyrosine diesters that form in the presence of enzymes.[64] These results have established peptide self-assembled structures as potential components in smart, responsive materials (**Figure 6**). It is important to note that in all the examples mentioned above, the structure and function of self-assembled peptide-based nanostructures is determined ultimately by the interplay of molecular forces between their constituent building blocks.

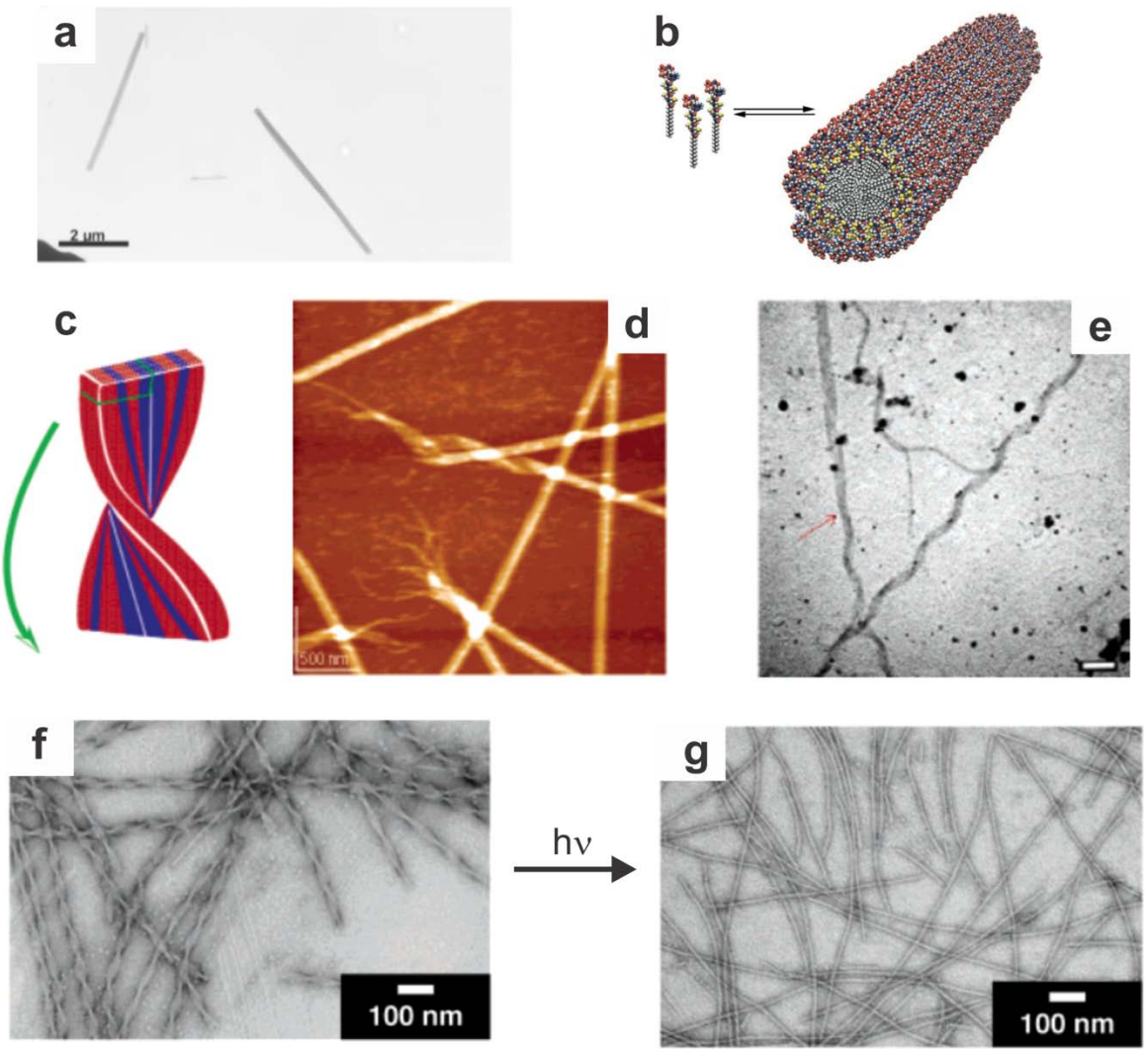

Figure 6. Various examples of peptide-based fibrous nanomaterials. (a) TEM image of nanotubes formed via diphenylalanine (FF) self-assembly. Images adapted with permission from ref. 56. Copyright 2003 AAAS. (b) Cartoon representation of peptide conjugate, containing both hydrophilic and hydrophobic segments, that self assemble into nanotubes. Images adapted with permission from ref. 53. Copyright 2001 AAAS. (c) Illustration representing twisted 1D fibers formed from amyloid peptides responsible for causing neurodegenerative diseases. (d) AFM image and (e) TEM image of twisted fibers formed from amyloid peptide, CH_3CO-KLVFFAE-NH_2. Images adapted with permission from ref. 61. Copyright 2003 American Chemical Society. Peptide conjugate containing photo-labile group self-assembles into (f) twisted 1D fibers. Upon exposure to UV light, cleavage of photo-labile moiety leads to transformation of twisted fibers into (g) cylindrical fibers. Images adapted with permission from ref. 63. Copyright 2008 American Chemical Society.

In addition to self-assembly, peptides are also versatile agents for inorganic substrate-binding. Phage display techniques are used to identify and isolate peptide sequences that recognize and associate to specific inorganic surfaces.[65] Belcher and coworkers have developed combinatorial phage-display techniques which evolve peptides that bind to a range of inorganic surfaces with high specificity depending on orientation and composition.[66] Furthermore, in many cases, these polypeptide sequences exhibit sequence specific inorganic binding.[67] Peptides identified from such methods can also be used to precisely control the shape and size of NPs. For example, Naik and coworkers have used AYSSGAPPMPPF, a peptide sequence identified and evolved through phage-display methods to have an affinity for gold and silver (111) surfaces, to synthesize water-stable, monodisperse AuNPs coated with AYSSGAPPMPPF (**Figure 7**).[68]

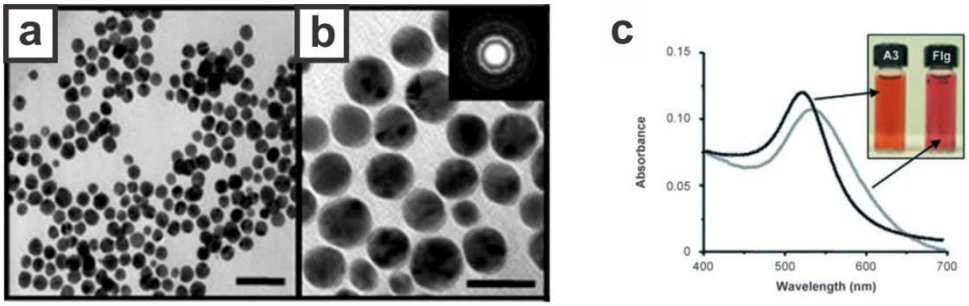

Figure 7. Peptide sequence AYSSGAPPMPPF, discovered through phage display methods, binds to AuNP surfaces. (a, b) TEM images reveal spherical AuNPs prepared in the presence of AYSSGAPPMPPF. The particle surface is stabilized via peptide capping. (c) LSPR absorption of peptide-capped AuNPs. Images adapted with permission from ref. 68. Copyright 2005 Wiley.

The gold-binding peptide sequence, AYSSGAPPMPPF, referred to here as PEP_{Au}, has been the subject of extensive theoretical and experimental research. Researchers have examined the role played by individual amino acids in gold surface binding. For example, molecular dynamics study performed by Carri and coworkers reveal that the interaction of PEP_{Au} on an infinite Au(111) surface can be understood as a combination of diffusion, anchoring, crawling,

and binding processes.[69] These studies identify tyrosine, methionine, and phenylalanine as strong binding residues, serine as an anchoring amino acid, and glycine and alanine as key amino acids that provide flexibility to the peptide backbone. The role of several gold-binding peptides, including PEP_{Au}, in the synthesis of discrete AuNPs was elucidated by Walsh and coworkers in 2016.[70] This study provided an atomic-scale picture of PEP_{Au} adsorbed on the surface of individual AuNPs and concluded that the size of discrete AuNPs is dictated by the extent of peptide adsorption on the NP surface. In addition to tyrosine, methionine, and phenylalanine which act as strong binding residues, the binding interaction of all amino acids in PEP_{Au} is calculated theoretically via replica-exchange with solute tempering molecular dynamics simulations (**Figure 8**).

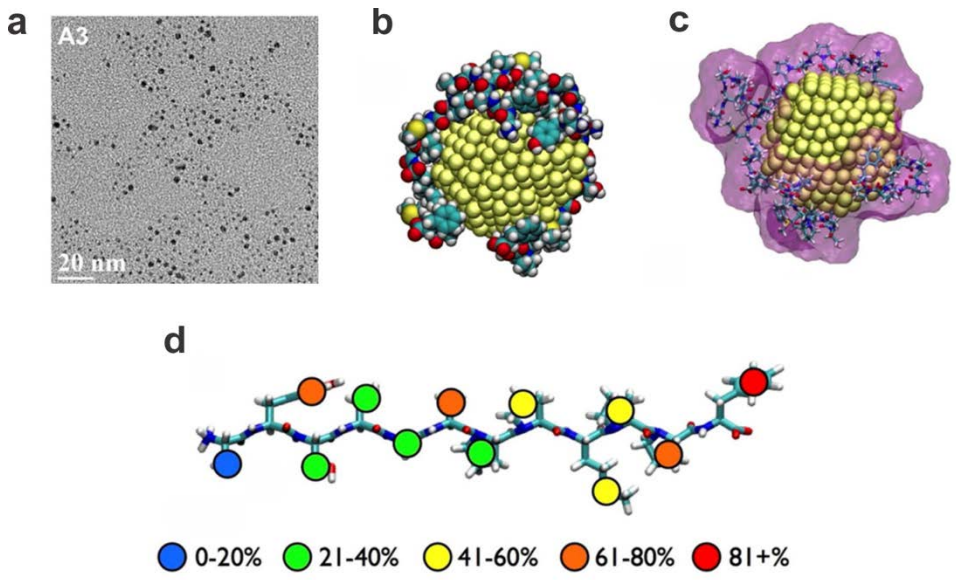

Figure 8. Experimental and theoretical study of PEP_{Au}-based AuNP synthesis. (a) TEM image of AuNPs synthesized in the presence of aqueous $HAuCl_4$, $NaBH_4$, and PEP_{Au}. (b) Typical configuration of PEP_{Au} adsorbed on AuNP surface obtained via theoretical modelling. (c) Exposed surface within PEP_{Au} capped AuNP. (d) Average degree of amino acid-AuNP surface contact within PEP_{Au} sequence. Left to right, N-terminus to C-terminus. Images adapted with permission from ref. 70. Copyright 2016 American Chemical Society.

1.3.2 Peptide-Based Method for Constructing AuNP Superstructures

Inspired by these properties of peptides, the Rosi group has developed peptide-based methods for constructing structurally complex assemblies of AuNPs.[26,71-75] The central building unit in this methodology is the peptide conjugates (R-PEP_{Au}), where R is either an aliphatic or aromatic organic tail attached to the PEP_{Au} sequence. By tuning the hydrophobic R group and peptide sequence, these peptide conjugates can assemble into different supramolecular architectures including spheres (e.g. micelles or vesicles),[74] twisted ribbons,[26] and helical coils.[22] Moreover, in the presence of a gold ion source and reducing agent, these peptide conjugates bind to NPs and direct their assembly into complex superstructures, including hollow spheres,[72] 1D assemblies,[75] and helical superstructures.[22] In the next section, I present, as a representative example of this methodology, AuNP single-helical superstructures that form the basis of my research projects.

1.3.3 Chiral Single-Helical Superstructures

Recently, the Rosi group has applied the peptide-based method to construct single-helical AuNP superstructures,[22] which exhibit intense chiroptical response in the visible region. Peptide conjugate, C_{18}-($PEP_{Au}^{M\text{-}ox}$)$_2$, where M-ox indicates methionine sulfoxide, was shown to direct the assembly of AuNP single helices (**Figure 9**). Transmission electron microscopy (TEM) and cryogenic electron tomography (cryo-ET) proved that these single-helical superstructures consist of oblong AuNPs with an aspect ratio of ~1.8 and have a helical pitch length of ~95 nm. Atomic force microscopy (AFM) revealed that C_{18}-($PEP_{Au}^{M\text{-}ox}$)$_2$ assembles into helical peptide fibers having similar pitch length. In the presence of gold ions and reducing agent, C_{18}-($PEP_{Au}^{M\text{-}ox}$)$_2$ binds

to and assembles AuNPs onto the outer surface of the helical coil to produce single-helical superstructures. Both Fourier transform infrared (FTIR) spectroscopy and circular dichroism (CD) spectroscopy revealed that C_{18}-($PEP_{Au}^{M\text{-}ox}$)$_2$ displays both β-sheet and polyproline II (PPII) secondary structures. Further, X-ray diffraction (XRD), and solid-state NMR (ssNMR) indicate that these helical coils exhibit both cross-β and polyproline II (PPII) secondary structures.

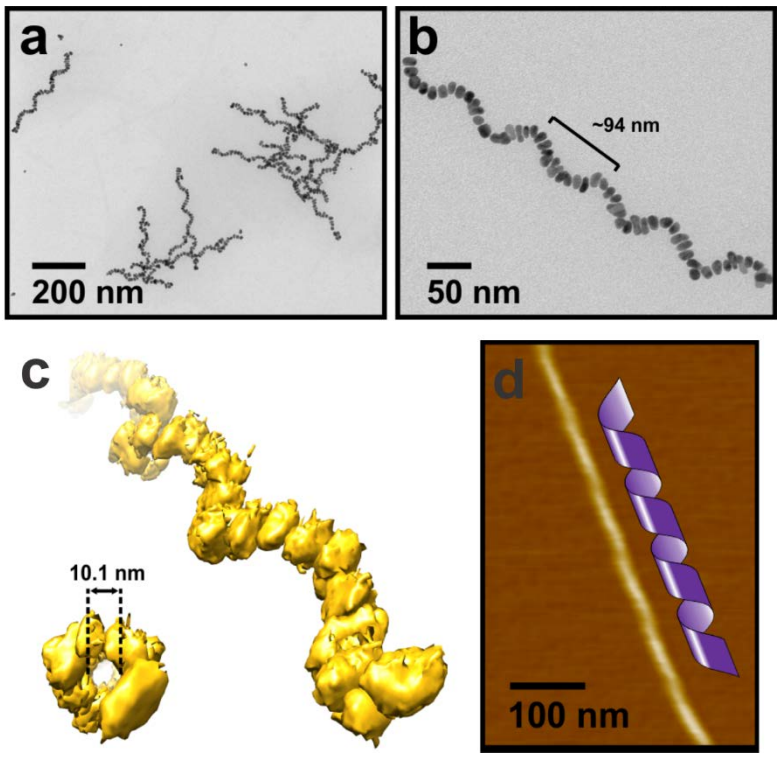

Figure 9. C_{18}-($PEP_{Au}^{M\text{-}ox}$)$_2$-directed synthesis of chiral AuNP single helices. (a, b) TEM images of AuNP single-helical superstructures. (c) cryo-ET 3D reconstruction of the single helices reveals their left-handed helicity as well as the internal diameter where the fiber resides. (d) AFM microscopy reveals that C_{18}-($PEP_{Au}^{M\text{-}ox}$)$_2$ self-assembles into left-handed helical ribbons. Images adapted with permission from ref. 22. Copyright 2016 American Chemical Society.

In accordance with these microscopic and spectroscopic results, an assembly model was proposed for C_{18}-($PEP_{Au}^{M\text{-}ox}$)$_2$ (**Figure 10**). According to the model, the helical coil consists of a monolayer of C_{18}-($PEP_{Au}^{M\text{-}ox}$)$_2$ arranged normal to the surface of the helical tape. The PPII helix and negatively charged phenylalanine residue at the peptides' C-termini are exposed to aqueous

buffer, while the N-terminus amino acids assemble into β-sheet secondary structure. Since the assembly model predicts a monolayer of C_{18}-$(PEP_{Au}{}^{M\text{-}ox})_2$, the aliphatic tails are assumed to be relatively ordered and packed at the inner surface of the helical coil via hydrophobic interactions. This allows the aliphatic tails to be shielded from the aqueous buffer.

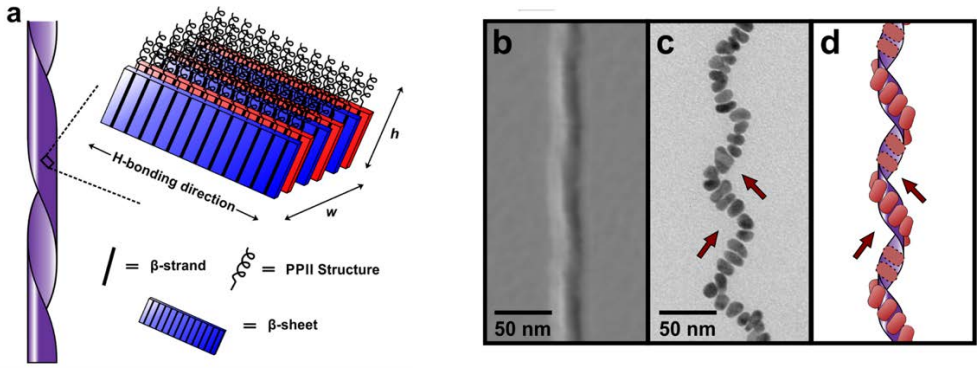

Figure 10. C_{18}-$(PEP_{Au}{}^{M\text{-}ox})_2$ assembly model. (a) β-sheets lie perpendicular to helical fiber surface, while PPII helices are exposed to the aqueous media. (b) AFM amplitude image of C_{18}-$(PEP_{Au}{}^{M\text{-}ox})_2$ helical ribbons, (c) TEM image of single helices synthesized via C_{18}-$(PEP_{Au}{}^{M\text{-}ox})_2$, (d) Proposed assembly model includes the attachment of AuNPs onto the outer surface of the helical fiber. The arrows indicate directional orientation of NPs within the single-helical superstructures. Images adapted with permission from ref. 22. Copyright 2016 American Chemical Society.

1.4 Research Objectives and Overall Challenge

The field of helical NP assemblies has made significant advances in the discovery, design, and synthesis of new helical morphologies. As elaborated previously, several new helical superstructures were synthesized from 2010-2015. However, in this period, there have been very few studies that describe systematic structure and property adjustment in any one type of topology. This is particularly important in the case of helical structures because the optical properties of these materials can be varied by adjusting the structural parameters of the helix.

As mentioned previously, the applications of these materials ultimately depend on their chiroptical properties. Therefore, there is a pressing need to develop a set of design principles for rationally tailoring the structural parameters and optical properties of helical superstructures, such as: i) **helical pitch length**, ii) **NP size**, and iii) **NP shape**.

Before I joined the Rosi laboratory in 2015, the basic AuNP assembly agent was primarily R-PEP_{Au}. In the context of adjusting the structural parameters of helical superstructures, small molecular transformations to the R group and the PEP_{Au} sequence had not been investigated. In this PhD dissertation, I present my work on making small alterations to the molecular structure of C_{18}-$(PEP_{Au}^{M\text{-}ox})_2$ in order to adjust the structural features and chiroptical activity of the AuNP single-helical superstructures (**Figure 11**).

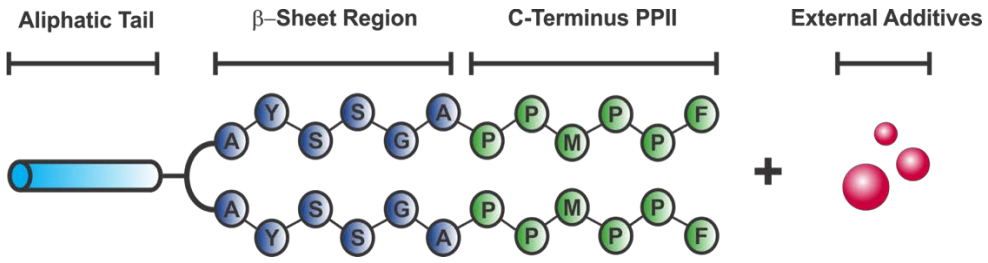

Figure 11. Tunable molecular handles for adjusting the nanoscale structure and chiroptical properties of AuNP single helices.

In Chapter 2, I present an effective strategy to systematically increase the helical pitch of single-helical superstructures by varying the aliphatic tail length of the peptide conjugates (*J. Am. Chem. Soc.* **2017**). In Chapter 3, I detail a β-sheet modification strategy to decrease the average helical pitch of single helices (*manuscript in preparation*). In Chapter 4, I determine that the position and oxidation state of the methionine residue within the C-terminus region is an important molecular handle to tune the size of the component NP within the helices. The experimental studies

in this project are complemented by theoretical simulations that measure the binding interaction of modified peptides with Au surface (*manuscript in preparation*). Finally, in Chapter 5, I describe a new synthetic strategy to influence NP shape of component particles within single-helical superstructures. I show that the shape of the constituent particles within the single helices can be modulated by adding external surfactants, and that the identity and concentration of the added surfactants are important factors in influencing particle shape (*Part. Part Syst. Charact.* **2019**).

2.0 Systematic Adjustment of Pitch and Particle Dimensions Within a Family of Chiral Plasmonic AuNP Single Helices

This work written in collaboration with Andrea Merg and Nathaniel L. Rosi, is reprinted with permission from the *Journal of the American Chemical Society* **2017**, *139*, 15043-15048. Copyright 2017, American Chemical Society. The supporting information is found in Appendix A.

Dr. Andrea Merg helped characterize the peptide conjugate assemblies and developed the peptide conjugate assembly model.

2.1 Introduction

As discussed in Chapter 1, chiral plasmonic NP superstructures represent a growing class of optoelectronic materials that exhibit enhanced optical chirality in the visible region arising from the chiral topological arrangement of NPs.[32,76] These materials hold immense promise as building blocks for chiroptical sensors,[30,41,77] circular polarizers,[3,78] and optical metamaterials.[2] While various unique chiral NP superstructures have been prepared (e.g., helices, toroids, tetrahedra, etc.),[27,28,79] reports detailing the systematic adjustment of structure and properties in any given structure type are limited.[40,73,80] Deliberate modulation, fine adjustment, and ultimately optimization of these properties, for applications, require precise control over NP placement and

spatial organization. Therefore, the current outstanding challenge in this field is to achieve definitive control over structure and properties of a particular chiral NP superstructure.

Since theoretical studies reveal that helical NP superstructures are ideal architectures for exhibiting strong chiroptical activity,[18] we are motivated not only to construct helical NP superstructures but also to deliberately alter their structures, in a straightforward fashion, to tune their properties. Realization of these goals hinges on robust assembly methods that permit rational, hypothesis-driven structure design.

As mentioned in chapter 1, in our NP assembly method, the peptide conjugate assembly serves as the underlying scaffold that defines the NP superstructure morphology. Because the NPs are grown in situ during the assembly process, this method may also allow for control over NP size and dimensions during the synthesis and assembly process. This stands in contrast to other common NP assembly methods in which NPs and scaffold materials are prepared independently and thereafter linker together to yield NP superstructures.[40] We postulate that this intrinsic feature may be exploited to simultaneously control multiple levels of structure in chiral NP assemblies (e.g. helical pitch, particle size, and particle aspect ratio).

The self-assembly of peptide conjugates is highly dependent on their chemical constitution.[81] In principle, small modifications to the peptide conjugate could influence the structural parameters of the conjugate assembly and therefore the resulting NP superstructure. In this chapter, we investigate how aliphatic tail length (C_x) within C_{18}-$(PEP_{Au}{}^{M\text{-}ox})_2$ influences single helix structural parameters. We demonstrate that differences of only 2 CH_2 units dramatically affect the length of the helical pitch and the NP dimensions within a family of AuNP single helices.

We postulate that helical ribbons constructed from conjugates with longer, more hydrophobic aliphatic tails may approach a closed cylindrical micelle structure, which would

reduce unfavorable interactions between the aliphatic tails and the aqueous assembly media. Our hypothesis is that this morphological transition can be induced either via a decrease in pitch length while maintaining constant ribbon width or via an increase in ribbon width, which can potentially lead to an increase in pitch length (**Figure 12**). Either of these assembly routes can ultimately affect the helical pitch length of the resultant NP single-helical assembly, leading to a family of helical superstructures with tunable optical properties (**Figure 12**).

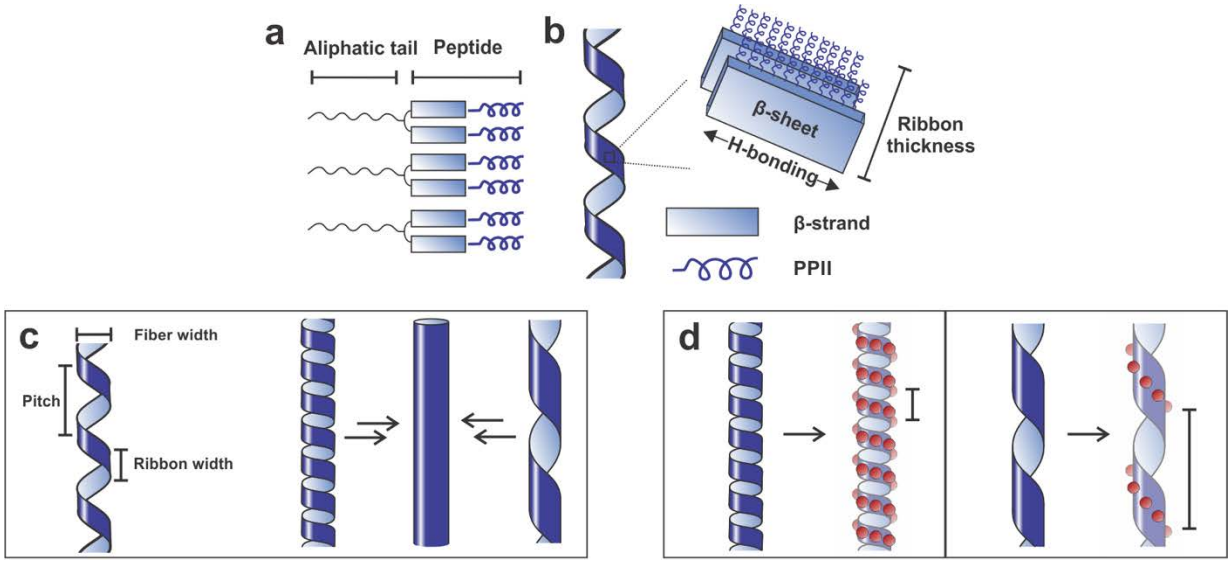

Figure 12. Helical ribbon assembly of C_{18}-$(PEP_{Au}^{M\text{-}ox})_2$. (a) Cartoon representation of C_{18}-$(PEP_{Au}^{M\text{-}ox})_2$ molecules forming a monolayer. (b) Assembly model of C_{18}-$(PEP_{Au}^{M\text{-}ox})_2$ helical ribbons. (c) Morphological features of the helical ribbon assembly and the postulated change in helical ribbon morpholgy with increasing aliphatic tail length. (d) Illustration showing how modifications to the helical ribbon morphology may affect the helical pitch of AuNP single helices.

2.2 Results and Discussion

To comprehensively test our hypothesis, a family of peptide conjugates varying in aliphatic tail length was synthesized: C_x-$(PEP_{Au}^{M\text{-}ox})_2$ where x = 14, 16, 18, 20, and 22 (**Figure S31, Table**

S1, Figure S32). Hereafter, each conjugate is referred to by its aliphatic tail length (e.g., C_{18}-$(PEP_{Au}^{M\text{-}ox})_2$ = C_{18}). We began by studying the assembly behavior of each peptide conjugate. Each conjugate was dissolved in 0.1 M HEPES (4-2-hydroxylethyl)-1-piperzainethanesulfonic acid) buffer (pH = 7.3) and allowed to sit at room temperature before transmission electron microscopy (TEM) analysis. With the exception of C_{14}, all peptide conjugates assembled into fibers (**Figure 13**). Even in the presence of Ca^{2+}, which is known to promote assembly,[82] C_{14} did not assemble; its hydrophilic (peptide) to hydrophobic (aliphatic tail) ratio is presumably too large to result in assembly in the HEPES medium. From TEM, the measured fiber widths of $C_{16\text{-}22}$ are 7.9 ± 0.8 nm, 8.7 ± 0.9 nm, 9.9 ± 1.5 nm and 9.7 ± 1.2 nm, respectively.

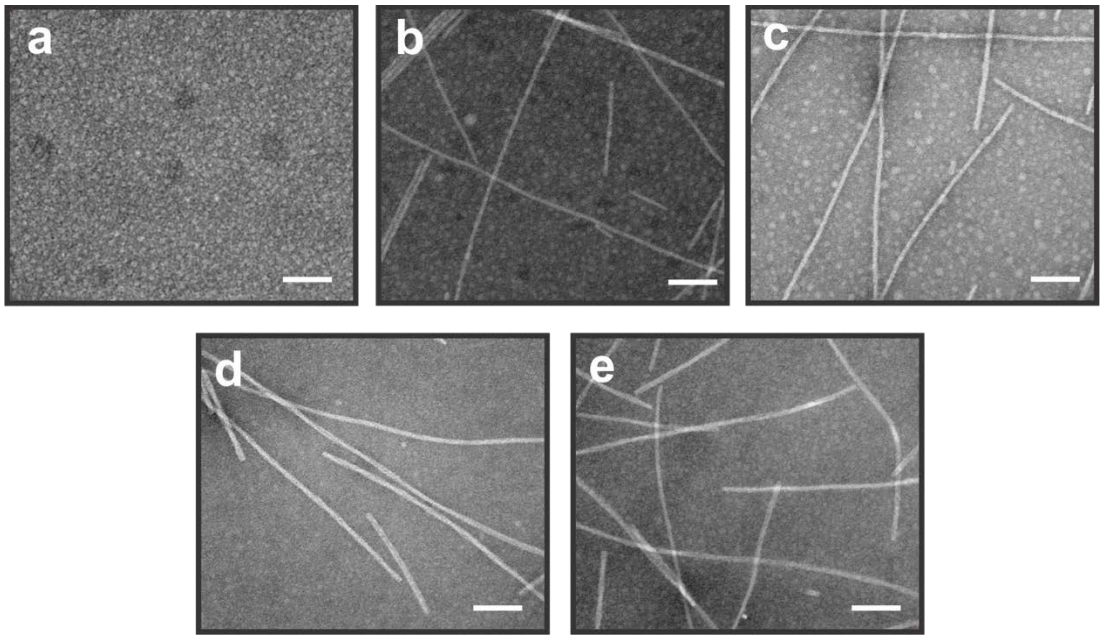

Figure 13. Fiber assembly not observed for (a) C_{14}. Fibers observed in the case of (b) C_{16}, (c) C_{18}, (d) C_{20}, (e) C_{22}.

Atomic force microscopy (AFM) was employed to discern the morphology of the peptide conjugates fibers. AFM images of $C_{16\text{-}22}$ revealed left-handed helical ribbons. The measured average ribbon width and pitch increases with aliphatic tail length (**Figure 14, Figure S33-S35**).

The ribbon thickness of $C_{16\text{-}22}$ fiber assemblies is ~3-4 nm (**Figure S33**), which is roughly equal to the length of the peptide head group after considering its secondary structure (**Table S2**). Fiber width data obtained from TEM analysis and ribbon height data exclude the possibility of $C_{16\text{-}22}$ packing into a bilayer configuration. The microscopic evidence suggests that all observed fibers are helical ribbons where the ribbon consists of a monolayer of assembled peptide conjugate molecules, consistent with our previously reported model.

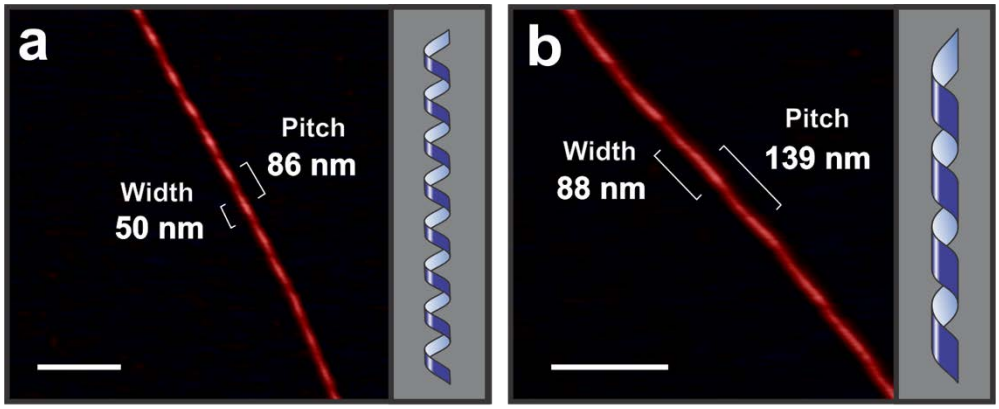

c

Peptide Conjugate	Ribbon Width (nm)	Pitch Length (nm)
C_{16}-$(PEP_{Au}^{M\text{-}ox})_2$	47 ± 6	82 ± 5
C_{18}-$(PEP_{Au}^{M\text{-}ox})_2$	55 ± 12	91 ± 8
C_{20}-$(PEP_{Au}^{M\text{-}ox})_2$	71 ± 9	103 ± 12
C_{22}-$(PEP_{Au}^{M\text{-}ox})_2$	87 ± 9	132 ± 16

Figure 14. Effect of aliphatic tail length on helical ribbon morphology. AFM images of (a) C_{16} and (b) C_{22} helical ribbons, showing differences in ribbon width and pitch length (scale bar = 200 nm). (c) Average ribbon width and pitch lengths of $C_{16\text{-}22}$ (based on 50 counts).

Examining the intermolecular structure of peptide conjugate assemblies is paramount to understanding their assembly.[83] For $C_{16\text{-}22}$ fibers, Fourier transform infrared (FTIR) spectra revealed symmetric and asymmetric C-H stretches at ~2850 cm^{-1} and 2920-2923 cm^{-1}, respectively, indicating ordered packing of aliphatic tails (**Figure S37a**, **Table S3**).[84] Amide I

bands at 1630 cm^{-1} are in line with β-sheet secondary structure (**Figure S37b**).[85] Consistent with TEM results that showed no fiber assembly, C_{14} does not display β-sheet character.

Circular dichroism (CD) spectroscopy was used to further probe the secondary structure. A negative peak at ~205 nm is indicative of polyproline II (PPII) conformation in solution[86,87] and a negative peak at ~215 nm is indicative of β-sheet conformation.[83] CD spectra of the peptide conjugates were collected both in the presence and the absence of Ca^{2+} ions. Ca^{2+} was added to mimic NP assembly conditions where Au ions are present. Ca^{2+} is known to promote assembly of peptide conjugate molecules by capping the negatively charged C-terminus. In the absence of Ca^{2+}, C_{16} and C_{22} display both PPII and β-sheet character (**Figure 15a**). However, in the presence of 1 mM $CaCl_2$, C_{18} exhibits pronounced β-sheet structure and the emergence of β-sheet structure is evident for C_{16} (**Figure 15b**). C_{14} shows only PPII structure both in the absence and presence of Ca^{2+} (**Figure S38**). We conclude from these data that $C_{18\text{-}22}$ assemble into fibers more readily and therefore exhibit greater β-sheet character than C_{16}.

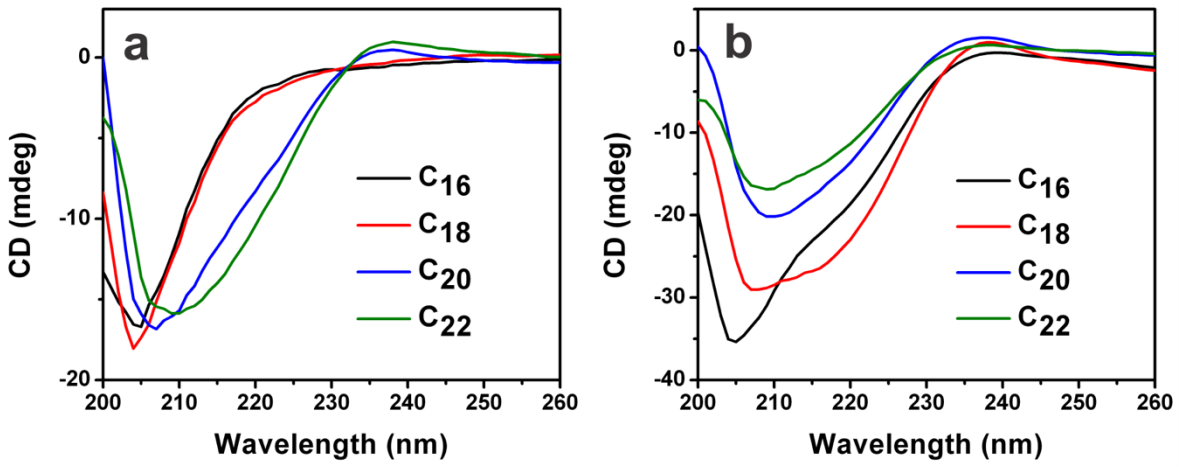

Figure 15. CD spectra of $C_{16\text{-}22}$ peptide conjugate assemblies collected either in the (a) absence or (b) presence of 1 mM $CaCl_2$.

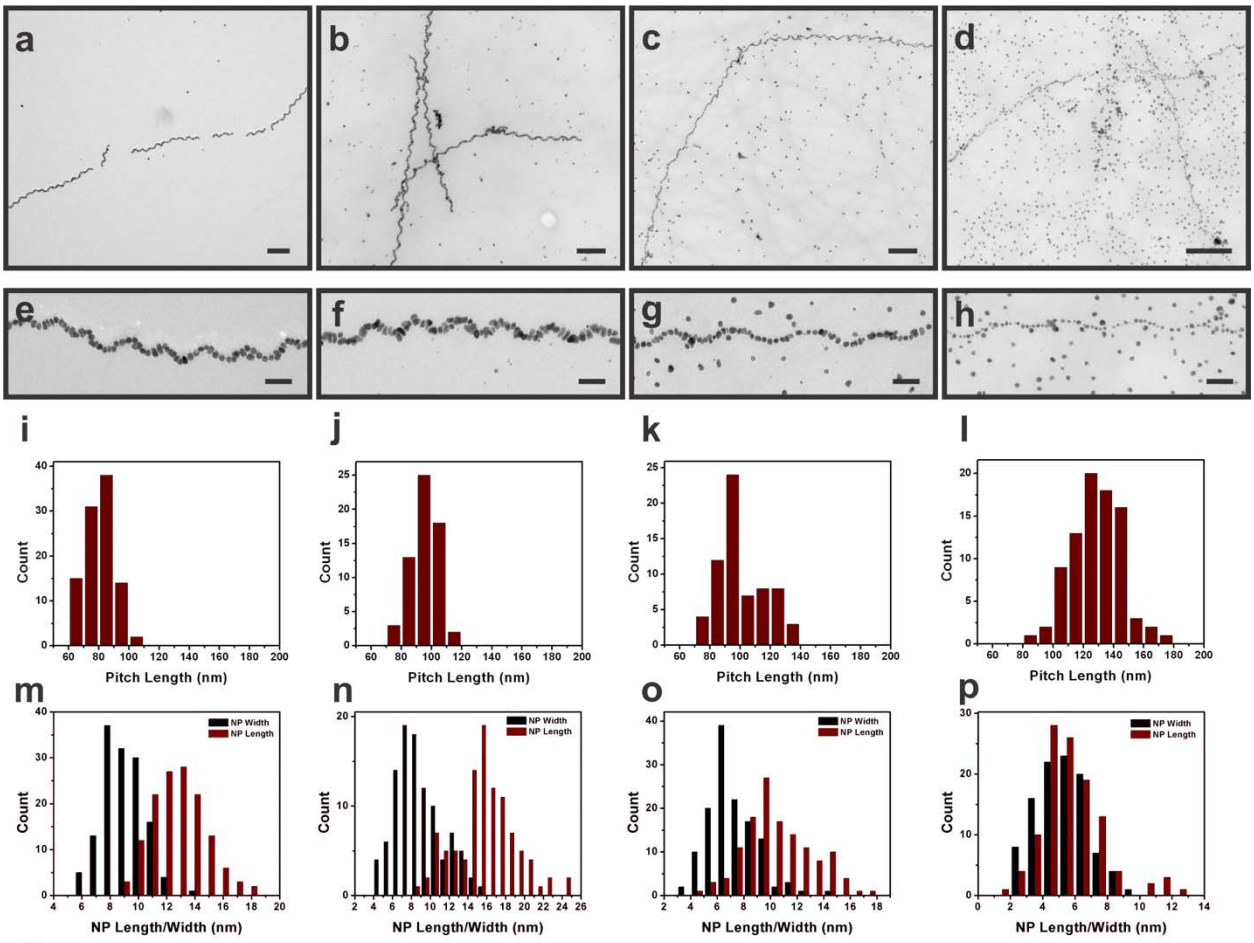

q

Peptide Conjugate	Pitch (nm)	Nanoparticle Length (nm)	Nanoparticle Width (nm)
C_{16}-$(PEP_{Au}^{M\text{-}ox})_2$	80 ± 9	13.4 ± 2.0	7.9 ± 1.8
C_{18}-$(PEP_{Au}^{M\text{-}ox})_2$	95 ± 7	15.9 ± 3.5	8.8 ± 2.5
C_{20}-$(PEP_{Au}^{M\text{-}ox})_2$	101 ± 15	10.5 ± 1.9	7.2 ± 1.8
C_{22}-$(PEP_{Au}^{M\text{-}ox})_2$	128 ± 16	5.8 ± 1.9	5.2 ± 1.6

Figure 16. Effect of aliphatic tail length on helical pitch and NP size and shape in a family of single-helical superstructures. Low magnification TEM images of single helices derived from (a) C_{16}, (b) C_{18}, (c) C_{20}, and (d) C_{22} (scale bar = 200 nm). High magnification TEM images of single helices derived from (e) C_{16}, (f) C_{18}, (g) C_{20}, (h) C_{22} (scale bar =50 nm). Helical pitch distributions of (i) C_{16}, (j) C_{18}, (k) C_{20}, (l) C_{22}-based single helices. NP length and width distributions of (m) C_{16}, (n) C_{18}, (o) C_{20}, and (p) C_{22}-based single helices. (q) Average helical pitch and NP length and width, tabulated as a function of peptide conjugate tail length (based on ~100 counts).

This family of peptide conjugates could serve to direct the assembly of AuNP single helices having incrementally different structural metrics (**Figure 16**). $C_{14\text{-}22}$ were used as assembly agents

using our established superstructure synthesis conditions.[26] They were each dissolved in HEPES buffer (the primary reducing agent for the Au ions), and an aliquot of a chloroauric acid/triethylammonium acetate (0.1 M $HAuCl_4$/TEAA) solution was added (see experimental section for details). C_{14} yielded non-assembled particles (**Figure S39**), as expected, because it does not assemble under the conditions studied. Initial syntheses employing C_{16} yielded similar results to C_{14} (**Figure S40**). On the basis of the CD results described above, we reasoned that C_{16}, might require Ca^{2+} to "prime" its assembly prior to addition of the $HAuCl_4$/TEAA solution. Accordingly, we added an aliquot of 0.1 M $CaCl_2$ to the C_{16} solution before adding $HAuCl_4$/TEAA to bring the [Ca^{2+}] $HAuCl_4$ to 1 mM. AuNP single helices with an average pitch length of 80 ± 9 nm resulted (**Figure S41**). $C_{18\text{-}22}$ yielded single helices with average pitch values of 95 ± 7, 101 ± 15, 128 ± 16 nm, respectively (**Figure 16**, **Figure S42-S44**). These values correlate well with those measured for the helical ribbons. The NP dimensions and shape also vary based on the peptide conjugate precursor, thereby allowing control over individual NP metrics in addition to superstructure morphology. In general, as the aliphatic tail length increases, the particles transition from oblong and rod-like to spherical (**Figure 16**).

We propose that differential peptide conjugate assembly behavior not only dictates helical pitch length but also indirectly influences the NP dimensions observed in each helical assembly. $C_{14\text{-}22}$ exhibit different assembly propensities, as illustrated by the CD spectroscopy data. Our prior work leads us to the understanding that, at the nascent stages of NP assembly, peptide conjugate molecules associate with small gold particles and then these particle conjugate constructs assemble together to produce single helices.[22] We reason that peptide conjugates with low assembly propensity (e.g., C_{14}) are rendered ineffective in this process and thus generate only unassembled NPs. Peptide conjugates with optimum assembly propensity (e.g., C_{18}) incorporate most of the

gold particles into their assembly, leading to AuNP single helices as the major product. Over time, the particles within the helices grow larger as more gold ions in solution are reduced. By extension, peptide conjugate molecules with high assembly propensity (e.g., C_{22}) assemble into fibers very rapidly and fail to effectively incorporate all the AuNPs into their assembly, leading to unassembled NPs as the major product. In this case, the average particle size within the helices is smaller than that observed for C_{16} or C_{18}. We attribute this observation to particle growth limitations that result from either (i) competition with the growth of free particles in solution; or (ii) more effective particle capping by the wider C_{22} ribbons.

Among this series of conjugates, C_{16} is unique because its assembly propensity can be significantly influenced by Ca^{2+}. It therefore provides a system that can be used to validate our reasoning for particle dimension control outlined above. As [Ca^{2+}] increases, C_{16} assembly propensity should increase, allowing reasonable comparison to the C_{22} system. In such cases, C_{16} should yield helices consisting of smaller spherical AuNPs as well as a large number of discrete, non-assembled NPs. Single helix syntheses were performed using C_{16} primed with increasing doses of Ca^{2+} (final $CaCl_2$ concentrations of 1 mM, 5 mM, 20 mM, and 40 mM). C_{16} directed the assembly of single helices comprising large, oblong particles at 1-5 mM $CaCl_2$ (**Figure 17**). In contrast, at 20-40 mM $CaCl_2$ concentrations, unassembled NPs were observed as the major product along with less well-defined single-helical superstructures comprising comparatively smaller, spherical particles (**Figure 17**, **Table S4**). These results corroborate our understanding that differential conjugate assembly behavior significantly influences NP dimensions. We acknowledge, however, that effects of wider C_{22} ribbons cannot be replicated using the C_{16} system.

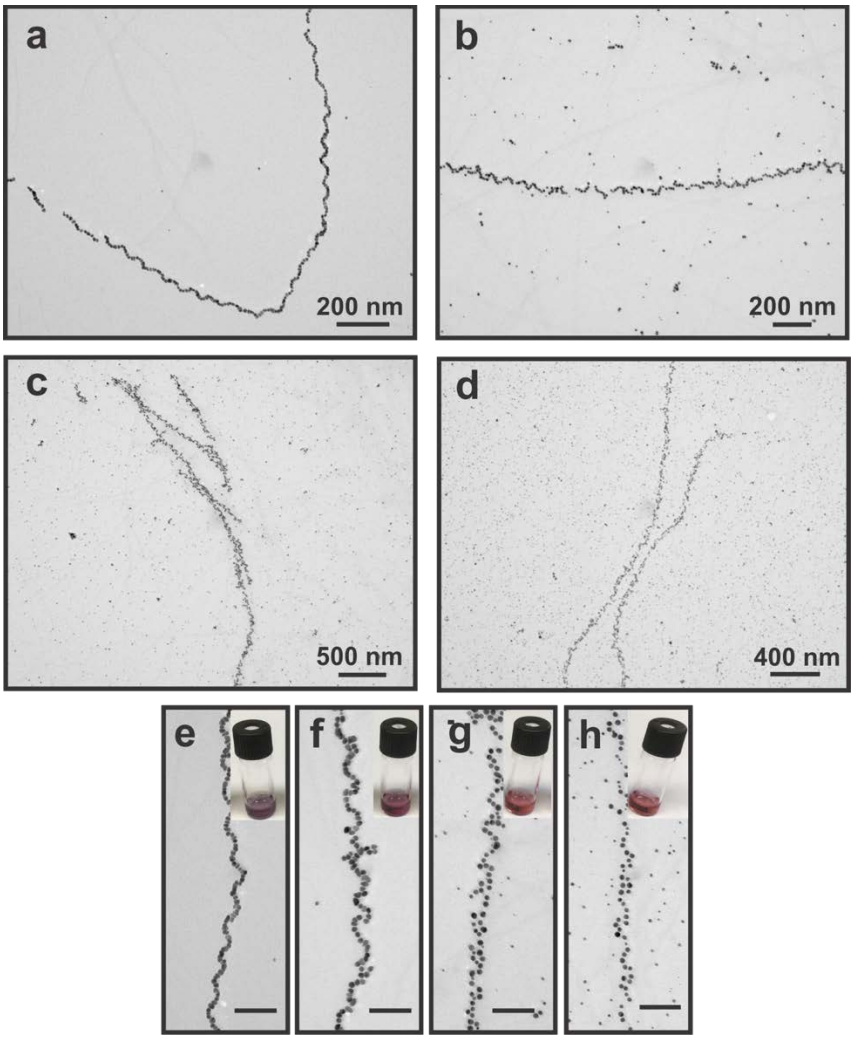

Figure 17. Effect of $CaCl_2$ concentration on the C_{16}-based assembly of single helices. Single helices consisting of larger oblong particles are observed as the predominant product at (a) 1 mM, (b) 5 mM $CaCl_2$, while less well-defined single helices and predominantly unassembled particles are observed at (c) 20 mM, and (d) 40 mM concentrations. High magnification images with reaction vials showing change in color (purple to red) with increase in $CaCl_2$ concentration at (e) 1 mM, (f) 5 mM, (g) 20 mM, and (h) 40 mM $CaCl_2$ concentration indicating increase in the number of free particles (scale bar = 100 nm).

In theory, the collection of structurally diverse $C_{16\text{-}22}$-based single helices should manifest differential chiroptical activity, as measured by their CD response and anisotropy factor (g).[18] Initial nonoptimized results revealed a decrease in chiroptical activity with increase in aliphatic

tail length. C_{16}-, and C_{18}-based single helices displayed large absolute *g*-factors, while C_{20}-based single helices displayed low chiroptical response (**Figure 18, Figure S45**) and C_{22} helices showed no observable response. Although these results are consistent with the observed trend in particle size and pitch length, and also the presence of unassembled gold nanoparticles that do not contribute to chiroptical activity, we do not rule out the possibility that an optimized synthetic protocol for $C_{20\text{-}22}$-based helices might yield high signal intensities. We note, though, that the nonoptimized *g*-factors observed for C_{16} and C_{18}-based single helices are comparable to the highest reported in the literature.

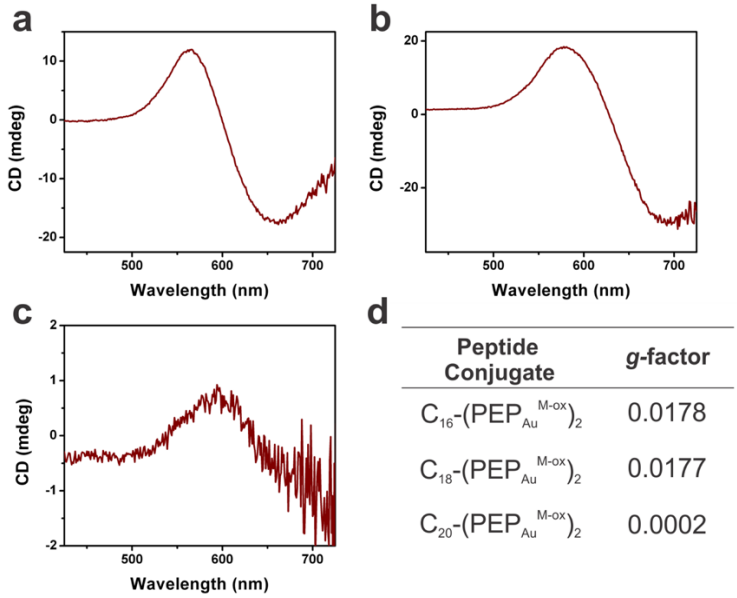

Peptide Conjugate	*g*-factor
C_{16}-$(PEP_{Au}^{M\text{-}ox})_2$	0.0178
C_{18}-$(PEP_{Au}^{M\text{-}ox})_2$	0.0177
C_{20}-$(PEP_{Au}^{M\text{-}ox})_2$	0.0002

Figure 18. Chiroptical properties of AuNP single helices derived from (a) C_{16}, (b) C_{18}, and (c) C_{20}. *g*-factors corresponding to $C_{16\text{-}20}$-based single-helical superstructures indicate a decrease in chiroptical activity with increase in aliphatic tail length.

2.3 Conclusion

Here, we have presented a rational design-based strategy that establishes peptide conjugates as excellent tailorable agents for attaining multiple levels of structural complexity in chiral superstructures. This is a unique demonstration that shows that single chemical modifications to a precursor assembly agent can be leveraged to simultaneously control the helical pitch, the NP dimensions, and therefore the chiroptical properties within a family of helical NP superstructures. Other regions of the peptide conjugate, such as the β-sheet region, could similarly be systematically modified, and therefore such modifications, too, should significantly affect the final assembly metrics and chiroptical properties.

2.4 Experimental Section

2.4.1 General Methods

All chemicals were obtained from commercial sources and used without further purification. Peptide (N_3-C_5H_8O-AYSSGAPPMPPF) was synthesized and purified by Pierce Biotechnology, Inc. Barnstead DiamondTM water purification system was used for Nanopure water (18.1 mΩ). Reverse-phase high-performance liquid chromatography (RP-HPLC) was performed by employing an Agilent 1200 liquid chromatographic system equipped with diode array and multiple wavelength detectors using a Zorbax-300SB C_{18} column. A linear gradient of 5-95% acetonitrile over 30 min was used to separate and purify all peptide conjugates. Acetonitrile and water were removed via lyophilization. Liquid-mass spectrometry (LC-MS) data were

analyzed using Shimadzu LC-MS 2020. UV-vis spectra were collected using an Agilent 8453 UV-vis spectrometer with a quartz cuvette (10 mm path length) at room temperature. All microscopy measurements were made using Image J.

2.4.2 Synthesis and Assembly Methods

$C_{14\text{-}22}$-$(PEP_{Au}{}^{M\text{-}ox})_2$, N_3-$(PEP_{Au}{}^{M\text{-}ox})$, and all organic intermediates were synthesized and purified by employing previously reported protocols.[22] Briefly, fatty acids were activated by employing standard NHS activation strategy. The corresponding functionalized NHS esters were treated with 2-amino-1,3-propanediol. The resultant diols were reacted with propargyl bromide to obtain the dialkyne organic substrate (refer to Appendix A for synthetic scheme). All final dialkyne organic intermediates were characterized via LC-MS (**Table S1**). Commercially obtained N_3-(PEP_{Au}) was dissolved in 1:1 Nanopure water and acetonitrile. Concentrated H_2O_2 was added to this solution to bring the final concentration of H_2O_2 equal to 100 mM. The resultant oxidized product was purified via HPLC and the purified product was thereafter lyophilized. Purified N_3-$(PEP_{Au}{}^{M\text{-}ox})$ was ultimately coupled with each dialkyne organic substrate using standard Cu-catalyzed click chemistry and purified via HPLC. Each purified peptide conjugate was characterized via LC-MS (**Figure S32**).

Purified peptide conjugates were lyophilized (18.725 nmol) and dissolved in 250 μL of 0.1 M HEPES buffer. The solution was sonicated for 5 min. Thereafter, an aliquot of 0.1 M $CaCl_2$ solution was added to bring the final concentration of $CaCl_2$ to 1 mM. TEM samples were prepared after ~16 hours.

Lyophilized conjugates, C_x-$(PEP_{Au}{}^{M\text{-}ox})_2$, (18.725 nmol for x = 14-20, and 9.4 nmol for x =22) were dissolved in 250 μL of 0.1 M HEPES buffer. The solution was sonicated for 5 min.

After 25 min, 2 μL of vortexed solution of 1:1 mixture of aqueous 0.1 M $HAuCl_4$ in 1 M TEAA buffer was added to the peptide conjugate solution. A localized black cloud was observed in 2-3 s and the vial was then immediately vortexed. For helices derived from C_{16}-$(PEP_{Au}{}^{M\text{-}ox})_2$, 2.5 μL of 0.1 M $CaCl_2$ was added to the peptide conjugate solution after sonication to yield a 1 mM $CaCl_2$ solution. TEM samples were prepared after 16 hours.

2.4.3 Fiber and NP Superstructure Characterization

Circular Dichroism Spectroscopy: CD experiments were conducted on an Olis DSM 17 CD spectrometer with a quartz cuvette (0.1 cm path length) at 25 °C with 8 nm/min scan rate. The PMT values ranged from 700-250V (200-280 nm). High PMT values observed close to 200 nm are due to HEPES absorption. The integration time was 5 sec. Peptide conjugates (18.725 nmol) were dissolved in 250 μL of 10 mM HEPES buffer to make a 75 μM solution and monitored via CD at 25 °C. For *g*-factor measurements, CD spectra were collected in 0.1 M HEPES and recorded 1 day after adding the $HAuCl_4$/TEAA mixture to the peptide conjugate solution.

Attentuated Total Reflectance Fourier Transform Infrared Spectroscopy: ATR-FTIR spectroscopy was conducted on PerkinElmer Spectrum 100 FTIR instrument equipped with an ATR accessory using PerkinElmer Spectrum Express software. Peptide conjugates were dissolved in 0.1 M HEPES buffer to afford a 75 μM solution. After 1 day, the solution was dialyzed against Nanopure water using d-tube dialyzers (Millipore catalog number 71505-3). The solution was concentrated and was drop cast onto the ATR-FTIR before collecting spectra.

Atomic Force Microscopy: AFM was conducted in tapping mode using an Asylum MFP-3D atomic force microscope and ultrasharp AFM tips. Freshly cut mica was functionalized by drop

casting 0.1% APTES (3-aminopropyl-triethoxysilane) solution and rinsing with Nanopure water. 50 μL of peptide conjugate in 0.1 M HEPES solution was drop cast and rinsed with water and allowed to dry overnight in a desiccator.

Transmission Electron Microscopy: TEM was conducted on a FEI Morgagni 268 operated at 80 kV and equipped with an AMT side mount CCD camera system. TEM samples were prepared by drop-casting 6 μL of peptide conjugate-HEPES solution onto a 3 mm-diameter copper grid with formvar coating (Electron Microscopy Sciences; FCF300-CU). After 5 min, excess solution was wicked away and the grid was air dried for 2 min. For studying peptide conjugate assembly, 6 μL of phosphotungstic acid (pH = 7) was drop cast onto the grid and allowed to sit for 30 s. For studying chiral NP assemblies, 6 μL of nanopore water was drop cast onto the grid and allowed to sit for 30 s. Excess solution was wicked away and the grid was allowed to air-dry for 5 min.

3.0 Beta-Sheet Modification Strategy for Affecting the Assembly Behavior of AuNPs

This chapter, written in collaboration with Nathaniel L. Rosi[*], is a *manuscript in preparation*. The supporting information for this chapter is found in Appendix B.

3.1 Introduction

Peptides exhibit unique self-assembly properties that depend upon their constituent amino acids.[88] Peptide sequence modification has previously been employed to effect changes in peptide conjugate self-assembly. For example, Stupp and coworkers have shown that the morphology of 1D fibers derived from a family of peptide conjugates can vary based on the relative position of hydrophilic and hydrophobic residues.[89] Stevens et al. proved that minute backbone changes such as serine to threonine substitutions can change peptide fiber morphology from twisted to planar ribbons.[90]

As described in Chapter 3, we were able to systematically increase the helical pitch length of AuNP single helices by adjusting the aliphatic tail length. Specifically, C_{16}-$(PEP_{Au}{}^{M\text{-}ox})_2$-directed single helices display an average pitch value of 80 nm while C_{22}-$(PEP_{Au}{}^{M\text{-}ox})_2$-directed single helices display an average pitch value of 120 nm. We were motivated by these trends to synthesize single helices with short pitch values (< 80 nm). However, contrary to the observed trend, C_{14}-$(PEP_{Au}{}^{M\text{-}ox})_2$ under similar conditions, does not self-assemble into helical fibers and consequently does not yield single-helical AuNP superstructures. Since, the aliphatic tail is primarily responsible for peptide aggregation via hydrophobic interactions, we reason that the

hydrophobic component within C_{14}-($PEP_{Au}^{M\text{-}ox}$)$_2$ molecules is relatively low and therefore prevents these molecules from assembling with each other. Multiple research questions arise: Can helical fiber assembly be achieved using C_{14} peptide conjugates? Is it possible to construct chiral single helices using C_{14} peptide conjugates? If so, will the average helical pitch of these assemblies be less than 80 nm? Ultimately, these questions are important for not only obtaining short pitch values but also optimized chiroptical properties.

In this chapter, we present a β-sheet modification strategy for answering these research questions. To test our reasoning, we prepare a series of sequence modified mutant C_{14} peptide conjugates, by introducing hydrophobic amino acids within the β-sheet segment in the $PEP_{Au}^{M\text{-}ox}$ sequence. Via these mutations, we can increase the hydrophobic gradient of the peptide conjugates without altering the aliphatic tail responsible for affecting the helical pitch of the superstructures. We demonstrate that the peptide assembly and NP superstructure morphology can be controlled via a single amino acid mutation. These results provide evidence that subtle changes to amino acid sequence in a series of gold-binding peptide conjugates is a powerful strategy to program structural variability in AuNP superstructures and adjust their optical properties.

3.2 Results and Discussion

We previously established that $C_{16\text{-}22}$-($PEP_{Au}^{M\text{-}ox}$)$_2$ helical ribbons fibers consist of a monolayer of peptides, arranged perpendicular to the fiber surface. While the C-terminus (-PPMPPF) anchor the AuNPs onto the fiber surface, the N-terminus amino acids engage in β-sheet formation. Since the β-sheet forming residues (~AYSSGA) are not associated with gold-binding in the proposed helical ribbon model,[22] we hypothesize that swapping the hydrophilic serine (S)

residue with more hydrophobic amino acids will effectively increase the hydrophobic to hydrophilic ratio in C_{14}-$(PEP_{Au}{}^{M\text{-}ox})_2$ (**Figure 19**).[91]

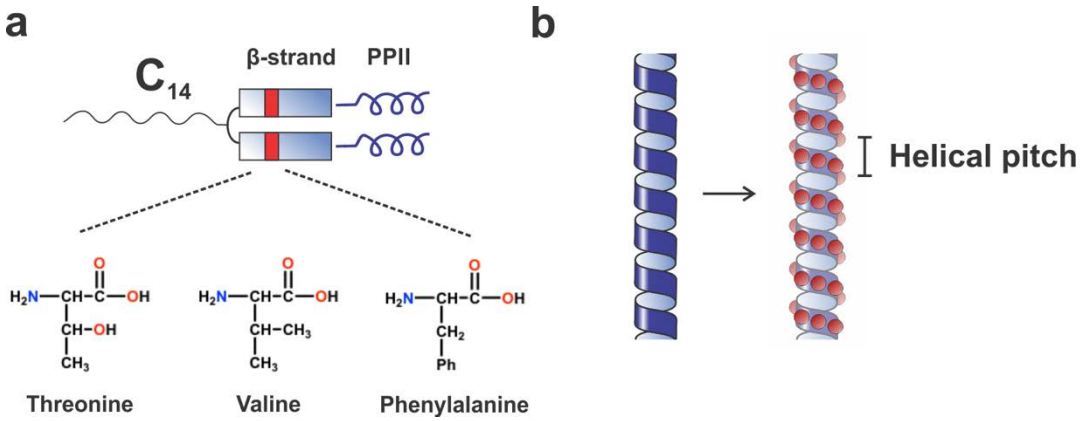

Figure 19. β-sheet modification strategy for affecting self-assembly of C_{14}-$(PEP_{Au}{}^{M\text{-}ox})_2$ peptide conjugate. (a) Swapping hydrophilic serine residue in the β-sheet region of the $PEP_{Au}{}^{M\text{-}ox}$ sequence with relatively hydrophobic amino acids: threonine (T), valine (V), and phenylalanine (F). (b) Tightly wound helical ribbon is the target self-assembly morphology expected from either one or all mutant peptide conjugates. We expect that tightly wound helical ribbons should yield single-helical superstructures with short helical pitch values.

To test this hypothesis, we synthesized a series of mutant peptide conjugates, C_{14}-$(AYSXGAPPM^{ox}PPF)_2$ where X = T (Threonine), V (Valine), F (Phenylalanine); refer to Appendix B for mass spectrometry characterization (**Figure S49**, **Figure S50**). Hereafter, each peptide conjugates is referred to by its modified amino acid residue (e.g.: C_{14}-$(AYSFGAPPM^{ox}PPF)_2$ = $C_{14}{}^{F}$). We purposefully chose these amino acids because they possess side chains that represent a broad range of more hydrophobic functional groups compared to the serine side chain: (polar hydrophobic (T), aliphatic (V), aromatic (F)). We began examining the assembly pattern of this series of peptide conjugates. Each peptide conjugate was dissolved in 0.1 M HEPES buffer (pH = 7.3) at room temperature. $C_{14}{}^{V}$ and $C_{14}{}^{F}$ both assemble into 1D fibers as

observed by transmission electron microscopy (TEM). However, C_{14}^{S} and C_{14}^{T} do not assemble into any discernible 1-D structure (**Figure 20**).

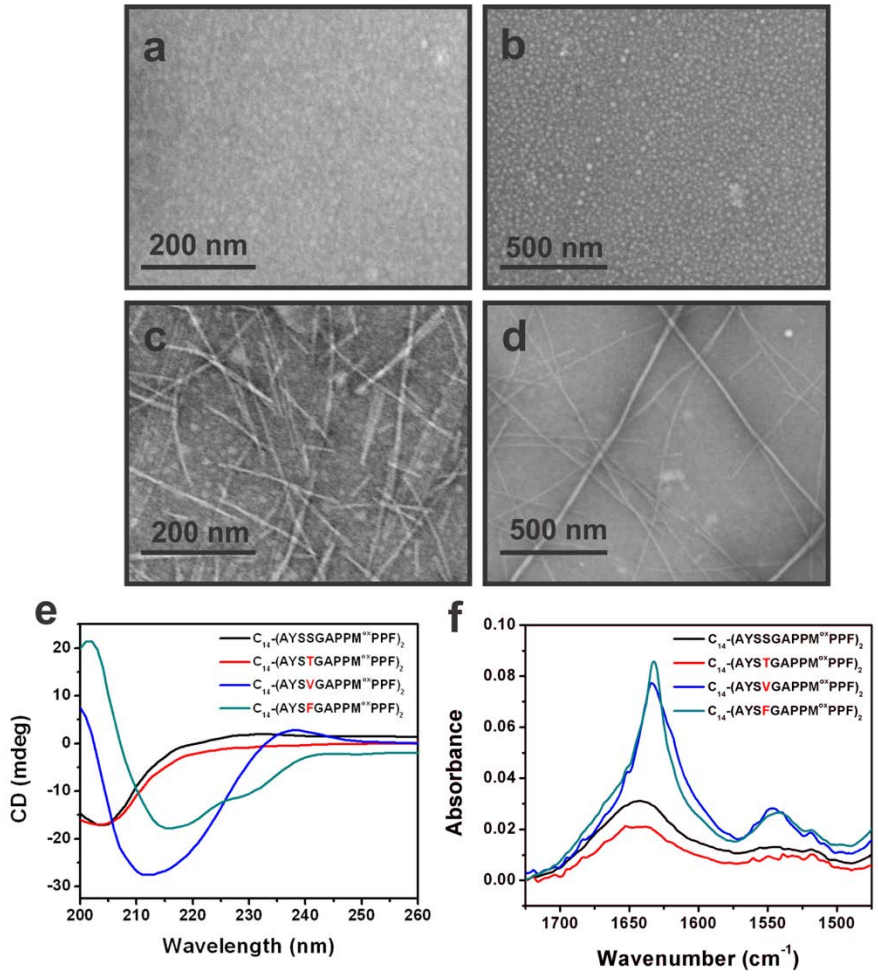

Figure 20. C_{14}^{X} assembly pattern monitored via TEM, IR, and CD spectroscopy (X = S, T, V, F). Negatively-stained TEM images of (a) C_{14}^{S}, (b) C_{14}^{T}, (c) C_{14}^{V}, and (d) C_{14}^{F} peptide conjugate assembly experiments. (e) CD spectra of C_{14}-based peptide conjugate assemblies, and (f) FTIR spectra of C_{14}-based peptide conjugate assemblies.

FTIR spectroscopy and CD spectroscopy are excellent analytical tools to verify and further probe peptide assembly.[83,85] FTIR spectra of C_{14}^{V} and C_{14}^{F} reveal distinct amide I peaks centered at ~1630 cm^{-1}, indicative of β-sheet secondary structure,[83] while C_{14}^{S} and C_{14}^{T} display broad peaks centered around ~1645 cm^{-1}, characteristic of unordered secondary structures (**Figure 20**). Further,

CD spectra of C_{14}^{V} and C_{14}^{F} display characteristic β-sheet signature with a negative peak centered between 215-220 nm,[83] while spectra of C_{14}^{S} and C_{14}^{T} display a negative peak at ~205 nm which is indicative of unassembled peptide in solution (**Figure 20**).[87] Taken together, both microscopic and spectroscopic data are in good agreement and strongly suggest that valine and phenylalanine mutations promote peptide conjugate assembly in this series of C_{14} backbone modified peptide conjugates.

We next proceeded to examine the effect of valine and phenylalanine mutations on peptide fiber morphology via AFM (**Figure 21, Figure S52, S53**). High magnification AFM images reveal that C_{14}^{V} fibers have ill-defined periodicity and do not possess a distinct helical morphology. Interestingly, C_{14}^{F} forms tightly wound helical fibers. The average ribbon width measured in this case is 31± 3 nm. However, the average helical pitch measured in this case is equal to 63 ± 9 nm, which is ~20 nm less that the average pitch value of C_{16}-$(PEP_{Au}^{M\text{-}ox})_2$ fibers.

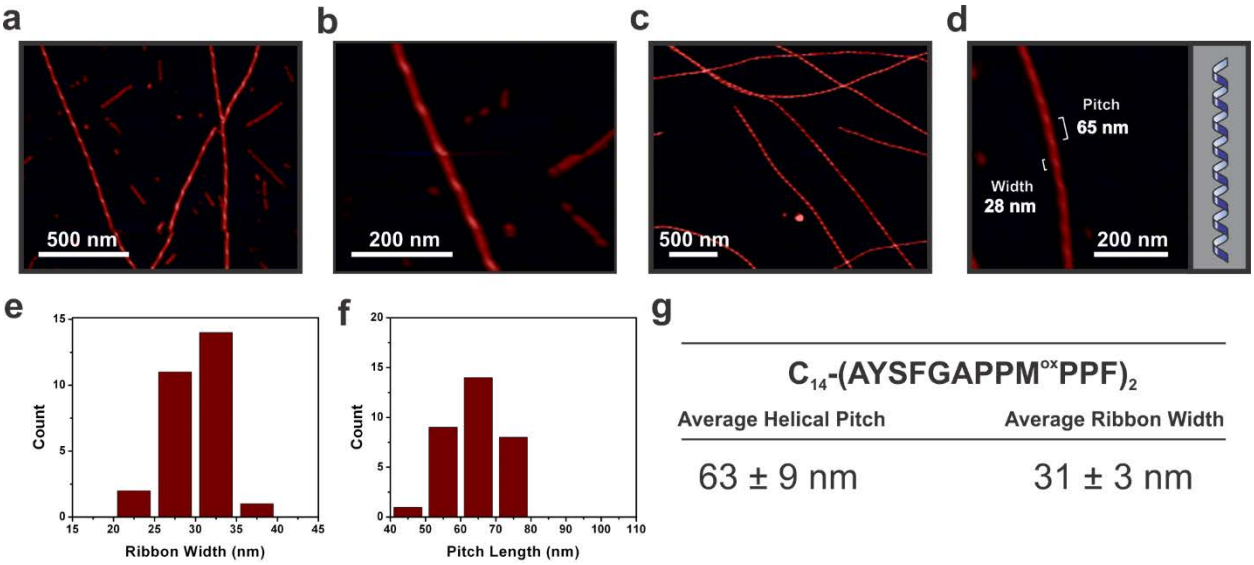

Figure 21. C_{14}^{V} and C_{14}^{F} fiber morphology differences examined via AFM analysis. (a) Low magnification and (b) high magnifcation images of C_{14}^{V} fibers. (c) Low magnification and (d) high magnification images of C_{14}^{F} fibers. (e) Ribbon width and (f) helical pitch length distribution of C_{14}^{F} fibers. (g) Average helical pitch and average ribbon width value tabulated for C_{14}^{F} fiber assemblies.

In order to establish that β-sheet modification does not affect gold-binding ability we designed two sets of control experiments. We subjected each modified peptide sequence to previously reported conditions of discrete NP synthesis. N_3-$PEP_{Au}^{T, M\text{-}ox}$, N_3-$PEP_{Au}^{V, M\text{-}ox}$, and N_3-$PEP_{Au}^{F, M\text{-}ox}$ all yielded disperse solution of stable branched NPs in 0.1 M HEPES buffer (**Figure S54**). Secondly, we synthesized peptide conjugate C_{18}-$(AYSSGA)_2$. This particular peptide conjugate has high self-assembly propensity because of its i) longer and more hydrophobic aliphatic tail, and ii) shorter hydrophilic peptide portion. We expect this conjugate to self-assemble in HEPES buffer but not form NP superstructures due to the absence of the -$PPM^{ox}PPF$ region. Following our NP assembly conditions, we observed that C_{18}-$(AYSSGA)_2$ assembles into fibers in 0.1 M HEPES buffer, however upon introduction of gold precursor solution, $HAuCl_4$/TEAA, it does not assemble any NP superstructures (**Figure S55**). Both these control experiments prove that

in our peptide assembly model, the C-terminus is primarily responsible for binding and recognizing gold surfaces. Modifications to the β-sheet region do not adversely affect gold-binding ability of $PEP_{Au}{}^{M\text{-}ox}$.

Next, we proceeded to investigate whether trends in the self-assembly behavior of the mutant peptide conjugates translated to similar patterns in NP assembly. We subjected each sequence-modified peptide conjugate to our established superstructure synthesis (**Figure 22**).[22] Consistent with peptide self-assembly patterns, $C_{14}{}^{S}$ and $C_{14}{}^{T}$ both yielded free discrete AuNPs. However, $C_{14}{}^{V}$ and $C_{14}{}^{F}$ directed the assembly of complex AuNP superstructures. $C_{14}{}^{V}$ yielded 1D assemblies of AuNPs while $C_{14}{}^{F}$ yielded pristine AuNP single helices. Interestingly, the average helical pitch of the single helices was measured to be ~67 nm, which is in excellent agreement with the helical pitch observed for $C_{14}{}^{F}$ helical fibers (**Figure 22, S56**). The NPs comprising the single-helical superstructures have average NP length and width equal to 11.4 + 2.1 nm and 7.2 + 2.4 nm, respectively. In addition to the single-helical superstructures observed in the $C_{14}{}^{F}$-based NP assembly, 1D AuNP chains are observed as a side-product (**Figure S57**). These superstructures are not helical but instead are achiral arrangements of oblong AuNPs in a linear fashion.

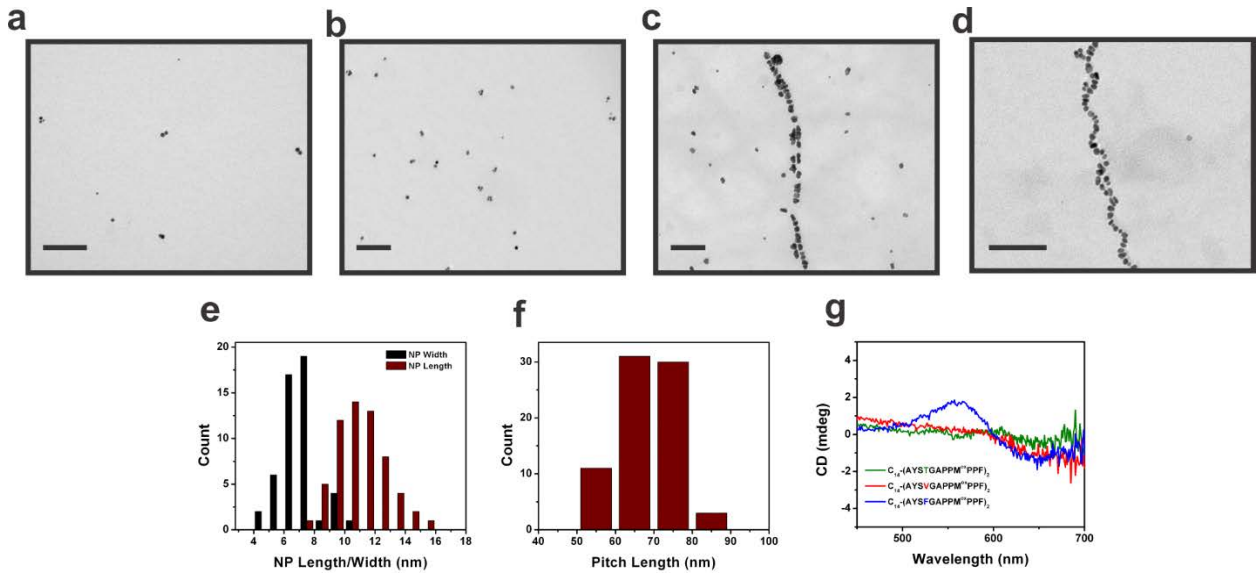

Figure 22. AuNP assembly behavior is dictated by amino acid modification within the β-sheet segment. Unassembled AuNPs result in (a) C_{14}^{S} and (b) C_{14}^{T}-based syntheses. (c) C_{14}^{V}-based synthesis yields 1D assemblies of AuNPs, while (d) C_{14}^{F}-based synthesis yields pristine AuNP single helices. Scale bar: 100 nm. (e) NP length and width distributions of component particles within the single helical superstructures. (f) Pitch distribution plot of C_{14}^{F}-based single helices. (g) CD signature of C_{14}^{X}-based NP superstructures/discrete NPs syntheses (X = T, V, F).

Ultimately, development of new synthetic methods to prepare complex NP assemblies are aimed at tuning their ensemble optical properties. As observed via CD spectroscopy, C_{14}^{S}, C_{14}^{T}, and C_{14}^{V} do not exhibit any chiroptical signal. However, C_{14}^{F} directed single-helical superstructures exhibit a distinct CD signal (**Figure 22**). We attribute the low signal intensity to either limited yield of single helices in solution or the achiral side products present in solution. In order to increase the yield of single-helical superstructures with short pitch values, we synthesized C_{16}-(AYSFGAPPM^{ox}PPF)$_2$. After subjecting C_{16}-(AYSFGAPPM^{ox}PPF)$_2$ to our NP assembly conditions, we synthesized single-helical superstructures with an average pitch value of 72 ± 7 nm (**Figure 23**). It is important to note that single helices derived from C_{16}-(AYSFGAPPM^{ox}PPF)$_2$ do not require Ca^{2+} prior to the addition of the gold salt as mentioned in Chapter 2. This

corroborates our theory that peptide conjugate hydrophobicity plays a crucial role in dictating the synthesis of single-helical superstructures. While C_{16}-(AYSSGAPPM^{ox}PPF)$_2$ requires Ca^{2+} to accelerate peptide conjugate assembly, C_{16}-(AYSFGAPPM^{ox}PPF)$_2$ does not due to the presence of hydrophobic phenylalanine residue in the β-sheet region. In addition, the average pitch values are similar for both C_{16}-(AYSSGAPPM^{ox}PPF)$_2$ and C_{16}-(AYSFGAPPM^{ox}PPF)$_2$-based single helices. Similar to C_{14}^{F}, the C_{16}-(AYSFGAPPM^{ox}PPF)$_2$-based synthesis also yields 1D AuNP chains as a side-product which in turn also affects the CD signal (**Figure S58**). Optimization methods to improve the CD signal of helices derived from both these peptide conjugates are underway.

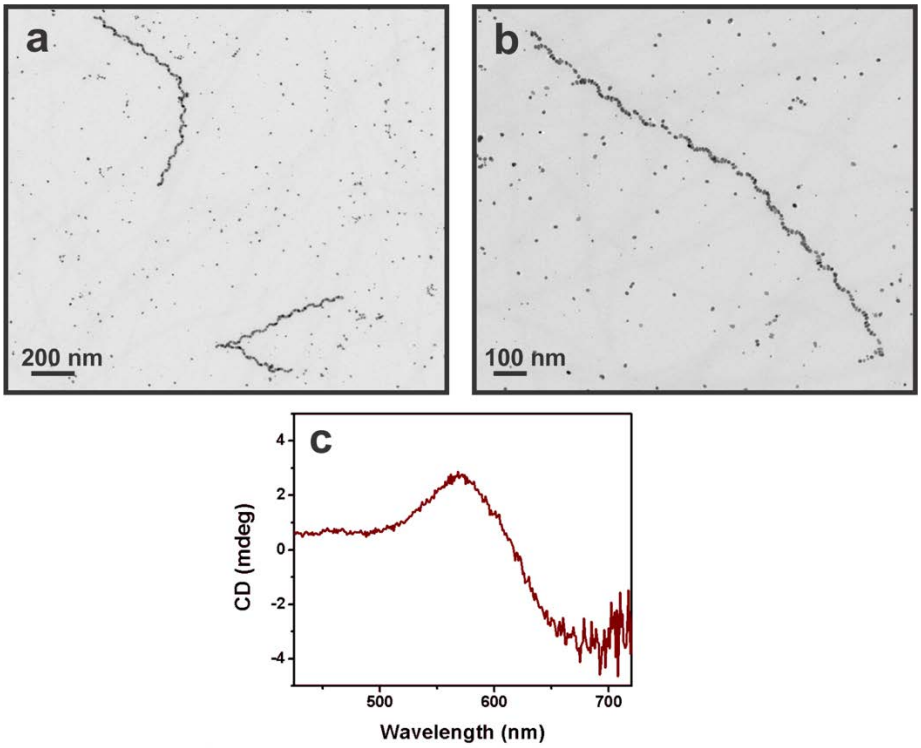

Figure 23. C_{16}-(AYSFGAPPM^{ox}PPF)$_2$-directed synthesis of single-helical AuNP superstructures exhibiting chiroptical CD signal. (a,b) TEM images of AuNP single helices prepared in the presence of C_{16}-(AYSFGAPPM^{ox}PPF)$_2$. (c) CD signature of the single helices plotted as a function of wavelength.

3.3 Conclusion

In summary, we demonstrate that single amino acid modification in a family of gold-binding peptide conjugates is an excellent strategy to not only affect the peptide conjugate assembly but also to rationally construct structurally diverse AuNP superstructures. A similar strategy for modifying the C-terminus of these peptide conjugates could also be effective in modulating gold-binding and consequently the size of the component NPs. These results lay a solid foundation for accessing multiple NP superstructure morphologies by fine-tuning the primary sequence of the assembly agent.

3.4 Experimental Section

3.4.1 General Methods

All chemicals were obtained from commercial sources and used without further purification. All peptides were synthesized using established microwave assisted solid phase peptide synthesis protocols on a CEM Mars microwave. Nanopure water (18.1 mΩ) from Barnstead DiamondTM water purification system was used to prepare all aqueous solutions. Peptides were purified by reverse-phase high-performance liquid chromatography on Agilent 1200 liquid chromatographic system equipped with diode array and multiple wavelength detectors using a Zorbax-300SB C_{18} column. Peptide masses were confirmed by liquid chromatography-mass spectrometry (LC-MS) data using Shimadzu LC-MS 2020. UV-Vis spectra were collected using

an Agilent 8453 UV-Vis spectrometer with a quartz cuvette (10 mm path length). All microscopy measurements were made using Image J software.

3.4.2 Synthesis

Peptide synthesis: All peptides were synthesized via established microwave assisted solid phase peptide synthesis protocol. Briefly, 138.8 mg (0.025 mmol) of Fmoc-Phe-NovasynR TGA resin (Millipore catalogue number: 8560340001) was soaked in DMF for 15 minutes. To begin the cycle of reactions, Fmoc-deprotection of the resin was performed by adding 2 mL of 20% 4-methylpiperidine in DMF to the resin and heating the mixture to 75 °C in 1 minute and holding at that temperature for 2 minutes. Excess reagent was drained using a filtration manifold and washed with copious amounts of DMF. To couple individual amino acids, 0.1 M solution of O-(1H-6-chlorobenzotriazole-1-yl)-1, 1, 3, 3-tetramethyluroniumhexafluorophosphate (HCTU) in N-methyl-2-pyrrolidone (NMP, 5 equivalents to resin, 1.25 mL) was added to Fmoc-protected amino acid (4 equivalents, 0.125 mmol) followed by N, N-diisopropylethylamine (DIEA, 7 equivalents, 0.175 mmol, 30.4 μL). The resulting solution was vortexed and centrifuged to ensure complete dissolution of amino acid. Thereafter, the solution was transferred to resin and heated to 75 °C for 1 minute and held at that temperature for 5 minutes. Excess reagent was then again drained and the resin was washed with copious amounts of DMF. This cycle was reactions were repeated for every amino acid. Proline and adjacent amino acid were coupled twice to ensure complete reaction of secondary amide group. The N-terminus was capped with 5-azido pentanoic acid using the same synthetic steps described above. Peptides N_3-$PEP_{Au}{}^{T,\ M\text{-}ox}$, N_3-$PEP_{Au}{}^{V,\ M\text{-}ox}$, and N_3-$PEP_{Au}{}^{F,\ M\text{-}ox}$ were all synthesized in this manner.

Peptide Conjugate Synthesis: C_{14}-dialkyne was synthesized using protocol reported in Chapter 2. C_{14}-dialkyne was attached to each azido peptide sequence via Cu-catalyzed click chemistry as described in chapter 2. The product was purified via HPLC and thereafter lyophilized.

3.4.3 Assembly Conditions

Peptide Conjugate Assembly: To 18.725 nmol of C_{14}^{X} (X = S, T, V, F) was added 250 μL of 0.1 M HEPES buffer. The solution was sonicated for 5 minutes and kept at room temperature for ~16 hours before TEM sample preparation.

NP Superstructure Assembly: 18.725 nmol of C_{14}^{X}, (X = S, T, V, F) and C_{16}-(AYSFGAPPM^{ox}PPF)$_2$, was dissolved in 250 μL of 0.1 M HEPES buffer, sonicated for 5 minutes and allowed to sit for 25 minutes. Thereafter, 2 μL of 1:1 mixture of aqueous 0.1 M $HAuCl_4$ in 1 M TEAA buffer was added to the peptide conjugate solution. About 2-3 seconds after addition of gold precursor solution, a localized black precipitate emerged which was rapidly vortexed.

3.4.4 Characterization and Sample Preparation

Circular Dichroism Spectroscopy: CD measurements were performed on Olis DSM 17 CD spectrometer with a quartz cuvette (0.1 cm path length) at 25 °C with 8 nm/min scan rate. The PMT values ranged from 700-250V (200-280 nm). High PMT values observed close to 200 nm are due to HEPES absorption. The integration time was 5 sec. C_{14}^{X} (X = S, T, V, F) was dissolved in 10 mM HEPES buffer (75 μM) and CD spectra were measured for each peptide conjugate. The CD signal of C_{14}^{F} and C_{16}-(AYSFGAPPM^{ox}PPF)$_2$-based single helices was measured in 0.1 M HEPES.

Attenuated Total Reflectance Fourier Transform Infrared Spectroscopy: ATR-FTIR measurements were conducted on PerkinElmer Spectrum 100 FTIR instrument equipped with an ATR accessory using PerkinElmer Spectrum Express software. C_{14}^{X} (X = S, T, V, F) was dissolved in 0.1 M HEPES buffer (75 μM) and left on the bench top for one day. After that time, the solution was dialyzed against Nanopure water using d-tube dialyzers (Millipore catalog number: 71505-3). The solution was concentrated and was drop cast on the ATR substrate before collecting spectra.

Atomic Force Microscopy: AFM measurements were performed in tapping mode using Asylum MFP-3D atomic force microscope and ultrasharp AFM tips (NanoandMore SHR-150). 0.1% APTES solution was drop casted onto a freshly cut mica surface, followed by rinsing with Nanopure water. 50 μL of C_{14}^{X} (X = V and F) dissolved in 0.1 M HEPES (75 μM) was then drop cast onto the mica surface and rinsed with water after 1 minute and allowed to dry in the desiccator overnight.

Transmission Electron Microscopy: TEM was conducted on a FEI Morgagni 268 operated at 80 kV and equipped with an AMT side mount CCD camera system. 6 μL of peptide conjugate-HEPES solution were drop casted onto a 3 mm-diameter copper grid with formvar coating (Electron Microscopy Sciences; FCF300-CU). After 5 minutes, excess solution was wicked away and the grid was air-dried for 2 minutes. For studying the peptide conjugate assembly of C_{14}^{F}, C_{14}^{V}, C_{14}^{T}, and C_{14}^{S}, 6 μL of phosphotungtic acid (pH = 7) were drop cast onto the grid and allowed to sit for 30 seconds. In the case of NP assemblies, 6 μL of Nanopure water was drop cast onto the grid and allowed to sit for 30 seconds. Excess solution was wicked away and the grid was allowed to air-dry for 5 minutes.

4.0 Effect of C-terminus Peptide Modification on the Structure and Chiroptical Properties of Helical AuNP Assemblies

This chapter, written in collaboration with Tiffany Walsh[*] and Nathaniel L. Rosi[*], is a *manuscript in preparation*. The supplemental information for this chapter can be found in Appendix C.

Prof. Tiffany Walsh performed all the computational studies on the mutant peptide sequences including the replica-exchange with solute tempering molecular dynamics (REST-MD) simulations.

4.1 Introduction

Small building blocks encode important information that translate to observable properties and function. This is illustrated in many technological and biological systems, e.g. sophisticated computing relies on the binary system (0 and 1), genetic information is encoded via 4 DNA bases, and peptide function is dictated by 20 natural amino acids. From the viewpoint of hybrid bioinspired materials, peptides are highly tunable agents for constructing these materials and also adjusting their structure and properties. Theoretical and experimental studies on PEP_{Au} reveal that systematic amino acid modification can alter the size and optical properties of individual AuNPs.[69,70] However, deliberate adjustment of component particle size and ensemble properties of an organized assembly of AuNPs via peptide sequence modification has yet to be explored.

Since the properties of AuNP assemblies depend upon AuNP size, interparticle distance, and 3-dimensional arrangement, we predict that encoding chemical information into PEP_{Au}-based AuNP assembly agents might serve as a powerful method for manipulating the collective optical properties arising from these assemblies.

As mentioned in Chapter 1, chiral AuNP superstructures represent an exciting class of optical materials that offer tremendous potential for several optical applications. In order to meet these applications, definitive control over the chiroptical signal intensity is required. Theoretical studies indicate that the chiroptical signal intensity is directly proportional to the NP size of the component particles.[18,37] We are therefore motivated to adjust the NP size and chiroptical properties of chiral AuNP superstructures via small chemical modifications to the assembly agent.

We have previously reported that the oxidation state of methionine can impact helical superstructure metrics. C_{18}-$(PEP_{Au})_2$ directs the assembly of AuNPs into irregular double helices comprising primarily spherical particles,[92] while C_{18}-$(PEP_{Au}{}^{M\text{-}ox})_2$ directs the assembly of AuNPs into chiral well defined single-helical superstructures comprising primarily rod-like particles.[22] At this stage, although the discrepancy in superstructure morphology is not clearly understood, it is evident that methionine plays a significant role in determining the fate of the AuNPs within the helices. These observations necessitate a comprehensive analysis of the Au-binding interactions of both oxidized and unoxidized peptides. Further, the strong gold-binding affinity of methionine also leads us to question whether the position of methionine/methionine sulfoxide within the C-terminus can be varied to affect the peptide-Au interaction. We hypothesize that the position of both M and M-ox within the C-terminus will dictate the extent of gold binding which in turn will affect the final size of AuNPs. We anticipate that the methionine-gold interactions could be leveraged to affect not only the size of discrete AuNPs but also the size of the component AuNPs

within the helical superstructures. We therefore predict that encoding chemical information via small methionine-based C-terminus modifications will lead to altered structural metrics of helical AuNP superstructures and also serve as a reliable method to tailor their chiroptical properties.

4.2 Results and Discussion

Since previously reported theoretical findings reveal that methionine interacts strongly with Au surfaces, our working hypothesis is that both the position and oxidation state of methionine can be varied to tune the overall peptide-Au interaction and therefore be effective in affecting NP size. We postulate that differences in peptide-Au interaction will affect the size of final AuNPs. To test our hypothesis, we began by synthesizing a series of mutant peptide sequences which vary in both the oxidation state and position of methionine residue (**Figure S59-S64, S65**). The unoxidized peptide series includes i) NH_2-AYSSGAMPPPPF, ii) NH_2-AYSSGAPPMPPF, iii) NH_2-AYSSGAPPPPMF, while the oxidized peptide series includes iv) NH_2-AYSSGAM^{ox}PPPPF, v) NH_2-AYSSGAPPM^{ox}PPF, and vi) NH_2-AYSSGAPPPPM^{ox}F. Hereafter, each mutant peptide sequence is referred to by the position and methionine oxidation state (e.g. $PEP_{Au}^{M\text{-}ox,\ 7}$ = NH_2-AYSSGAM^{ox}PPPPF and $PEP_{Au}^{M,\ 9}$ = NH_2-AYSSGAPPMPPF).

Peptide-capped NPs were synthesized following a known literature protocol[68] (refer to experimental section 4.4.3 for details). Briefly, peptides were dissolved in 0.1 M HEPES buffer (pH = 7), which acts a reducing agent for gold ions. Next, an aliquot of aqueous $HAuCl_4$ solution, was added to the peptide solution. The reduced AuNPs were examined via TEM (**Figure 24**).

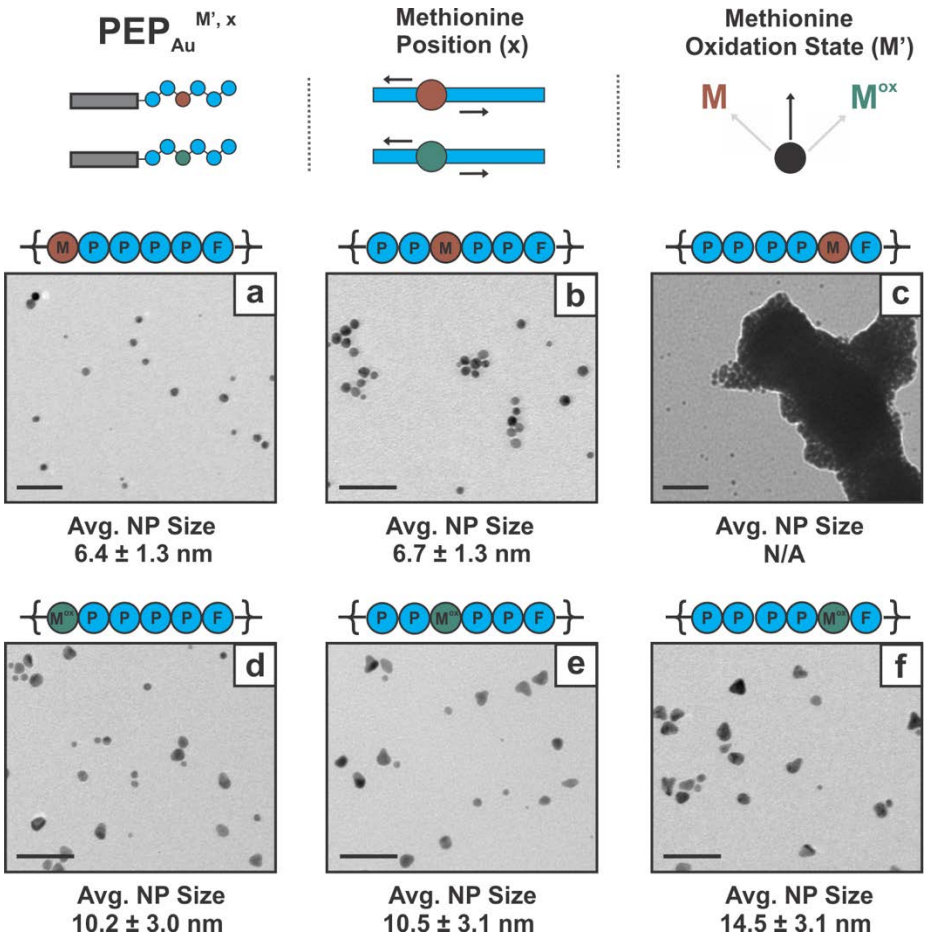

Figure 24. Effect of methionine modification on the size of AuNPs synthesized in the presence of mutated peptide sequences. TEM images of AuNPs synthesized in the presence of (a) $PEP_{Au}^{M,\ 7}$, (b) $PEP_{Au}^{M,\ 9}$, (c) $PEP_{Au}^{M,\ 11}$, (d) $PEP_{Au}^{M\text{-}ox,\ 7}$, (e) $PEP_{Au}^{M\text{-}ox,\ 9}$, and (f) $PEP_{Au}^{M\text{-}ox,\ 11}$. Average AuNP size distributions are listed below each case (based on ~100 counts). Scale bar: 100 nm.

We observed that particles prepared in the presence of unoxidized peptide sequences are predominantly spherical in nature. Peptides $PEP_{Au}^{M,\ 7}$ and $PEP_{Au}^{M,\ 9}$, yield spherical NPs with average particle size equal to 6.4 ± 1.3 nm and 6.7 ± 1.3 nm, respectively. However, $PEP_{Au}^{M,\ 11}$ yields large NP aggregates (**Figure 24**). Interestingly, the oxidized peptides do not follow these trends in NP size. $PEP_{Au}^{M\text{-}ox,\ 7}$, $PEP_{Au}^{M\text{-}ox,\ 9}$, and $PEP_{Au}^{M\text{-}ox,\ 11}$ yield larger non-spherical AuNPs exhibiting random shapes (**Figure 24**). The average particle size (longest dimension measured) for

particles prepared in the presence of $PEP_{Au}^{M\text{-}ox,\ 7}$ and $PEP_{Au}^{M\text{-}ox,\ 9}$ is equal to 10.2 ± 3.0 nm and 10.5 ± 3.1 nm, respectively. However, $PEP_{Au}^{M\text{-}ox,\ 11}$ yields AuNPs with slightly larger average diameter equal to 14.5 ± 3.0 nm. These trends in average NP diameter translate to their UV-vis absorption. The localized surface plasmon resonance (LSPR) peak for particles prepared in the presence of $PEP_{Au}^{M,\ 7}$ and $PEP_{Au}^{M,\ 9}$ is located at 519 nm and 525 nm. However, LSPR peaks for AuNPs synthesized in the presence of $PEP_{Au}^{M\text{-}ox,\ 7}$, $PEP_{Au}^{M\text{-}ox,\ 9}$, and $PEP_{Au}^{M\text{-}ox,\ 11}$ are much broader and red-shifted (**Figure S68**).

We employed theoretical modelling to study the effects of methionine-based backbone modifications on AuNP size. We started by first comparing the binding energy of small molecules on the surface of Au(111). Van der Waals density functional theory (vdW-DF)[93,94,95] calculations of dimethyl sulfoxide (DMSO) adsorbed on the Au(111) surface in vacuo predicts that the binding energy to be equal to -55 kJ/mol as compared to -77 kJ/mol for dimethyl sulfide. Using the unmodified parameters of the polarizable GolP-CHARMM force-field, we found a consistent trend, with a calculated in vacuo binding energy of -42 ±10 kJ/mol for DMSO, compared with our previously-reported value of -70 kJ/mol for dimethyl sulfide.[96] These preliminary data on small molecule counterparts suggest that the oxidized methionine has a weaker interaction with Au(111).

We proceeded to predict the degree of residue-surface contact for each residue within the modified and unmodified PEP_{Au} sequence adsorbed at the aqueous Au(111) interface. This characterization of peptide-surface adsorption is typically not an additive function of the peptide's constituent residues. This is due in part to the inherent intrinsic disorder of biocombinatorially-selected materials-binding peptides in general. The adsorbed state of such peptides cannot be adequately captured by a single conformation, but instead is more appropriately represented by a conformational ensemble. To this end, we used replica-exchange with solute tempering molecular

dynamics (REST-MD) simulations,[97,98] in partnership with the GolP-CHARMM force-field,[99] to predict the Boltzmann-weighted ensemble of conformations for each of the six surface adsorbed peptide in the presence of liquid water (**Figure 25**). REST-MD simulations of peptide-surface adsorption have been previously demonstrated to be highly effective, yielding binding results that are consistent with experimental data.[100,70] We began by comparing the binding interactions of the unoxidized PEP_{Au} mutant sequences. Compared to $PEP_{Au}^{M,9}$, both $PEP_{Au}^{M,7}$ and $PEP_{Au}^{M,11}$ reveal a decrease in binding interaction of the methionine residue (**Figure 25**). We relate this observation to the presence of 4 adjacent prolines (P) which result in a "mesogenic" rigid segment and therefore reduce the binding interaction of other residues. In the case of $PEP_{Au}^{M,7}$, change in methionine position does not affect the binding interactions of other amino acids significantly. Therefore, the overall binding interaction of $PEP_{Au}^{M,9}$ and $PEP_{Au}^{M,7}$ are comparable. However, in the case of $PEP_{Au}^{M,11}$, change in methionine position results in a global reduction in the binding interaction of other neighboring amino acids. $PEP_{Au}^{M,11}$ displays the least binding interaction with Au(111) surface. We speculate that this observation could be due to the competing effects of adjacent M and F residues, which are both strong binders. Overall, the theoretical binding interaction is in good agreement with the experimentally observed trends in AuNP sizes. Both $PEP_{Au}^{M,7}$ and $PEP_{Au}^{M,9}$ yield small spherical AuNPs. However, large AuNP aggregates are synthesized in the presence of $PEP_{Au}^{M,11}$.

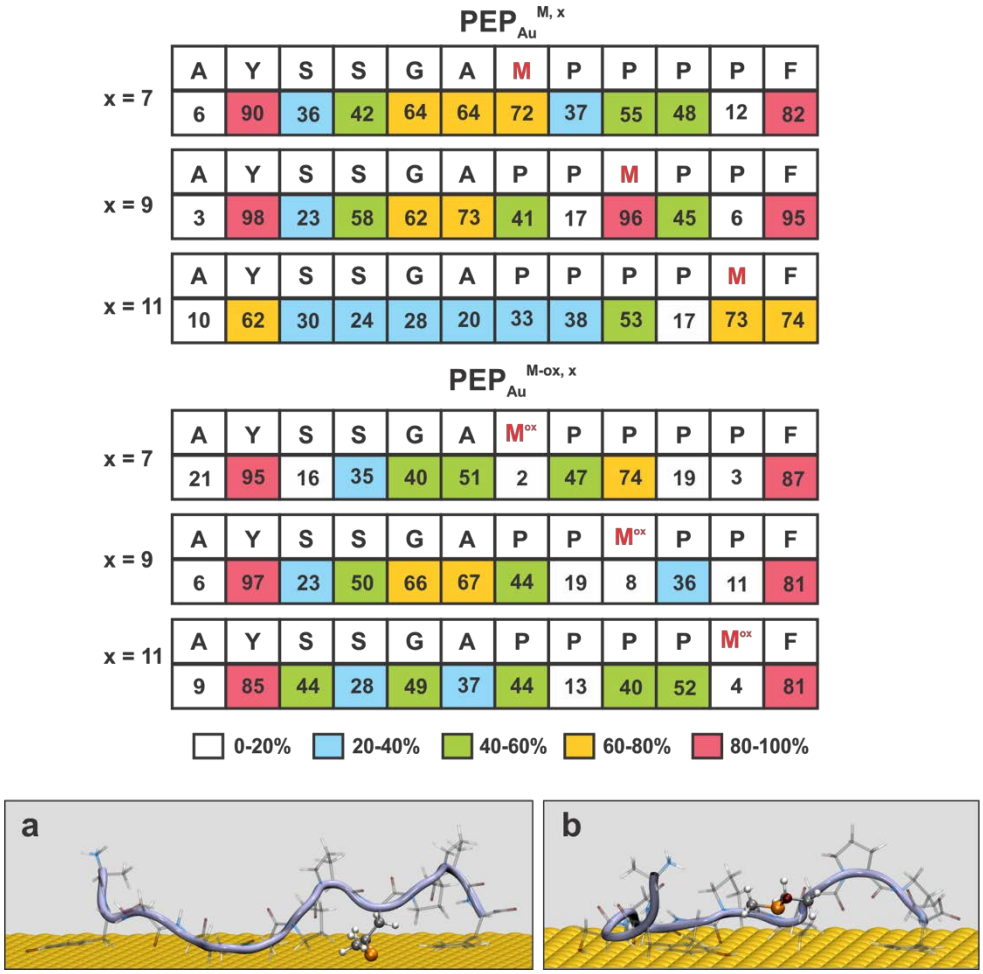

Figure 25. REST-MD simulations performed on oxidized and unoxidized peptide sequences. Average-degree of residue-Au contact (given as a percentage of the REST-MD trajectory) is listed for each residue in all sequences. Data for $PEP_{Au}^{M, 9}$ is taken from ref.101.[101] Representative structures of (a) $PEP_{Au}^{M, 9}$ and (b) $PEP_{Au}^{M\text{-}ox, 9}$ absorbed at the Au(111) interface as predicted from REST-MD simulations. Degree of contact between Au(111) surface and methionine sulfoxide (b) is drastically reduced compared to Au(111)-methionine interaction.

Next, we compared the binding interactions of the oxidized PEP_{Au} mutants. A common theme observed in all oxidized peptides regardless of methionine sulfoxide position residue is that the binding interaction of the methionine sulfoxide is dramatically low compared to unoxidized methionine (**Figure 25**). This observation is also consistent with the size discrepancy in discrete AuNPs synthesized in the presence of oxidized and unoxidized PEP_{Au} sequences. Compared to

$PEP_{Au}^{M\text{-}ox,\ 9}$, both $PEP_{Au}^{M\text{-}ox,\ 7}$ and $PEP_{Au}^{M\text{-}ox,\ 11}$ exhibit a slight reduction in overall binding interaction. Similar to the unoxidized peptides, this can be attributed to the presence of 4 adjacent proline residues causing rigidity in the sequence. Although one might expect both $PEP_{Au}^{M\text{-}ox,\ 7}$ and $PEP_{Au}^{M\text{-}ox,\ 11}$ to yield larger AuNPs compared to $PEP_{Au}^{M\text{-}ox,\ 9}$, experimentally large particles are observed only in the case of $PEP_{Au}^{M\text{-}ox,\ 11}$. From both theory and experimental data, we conclude that i) the oxidation of methionine dramatically decreases the peptide-AuNP binding interaction, and ii) the proximity of M/M-ox to the C-terminus of the peptide sequence causes either an increase in NP size or particle aggregation.

In order to confirm that the variations observed in the surface adsorption characteristics arise primarily due to the difference in the M-ox/M surface binding strength and not due to any differences inherent to the peptide conformational ensemble, we ran REST-MD simulations for each of the six sequences in the unadsorbed state. We characterized the resulting Boltzmann-weighted conformational ensemble of each of the six MD trajectories by using a clustering analysis (**Table S5-S10**). In general, this analysis identifies a set of like structures (referred to as clusters) and their fractional population in the ensemble. In this instance, our comparison was based on the structural similarity of the peptide backbone. We then used a cross-peptide analysis (**Table S11-S13**) to compare the structural similarity of *e.g.* each cluster in the $PEP_{Au}^{M,\ 7}$ ensemble to the set of clusters generated for $PEP_{Au}^{M\text{-}ox,\ 7}$. The clusters for the $PEP_{Au}^{M,\ 9}$/$PEP_{Au}^{M\text{-}ox,\ 9}$ and $PEP_{Au}^{M,\ 11}$ /$PEP_{Au}^{M\text{-}ox,\ 11}$ were similarly compared. Although the fractional populations of the clusters in each ensemble differ, we note a substantial degree of similarity between the backbone conformations for all three cases: $PEP_{Au}^{M,\ 7}$ /$PEP_{Au}^{M\text{-}ox,\ 7}$, $PEP_{Au}^{M,\ 9}$/$PEP_{Au}^{M\text{-}ox,\ 9}$ and $PEP_{Au}^{M,\ 11}$ / $PEP_{Au}^{M\text{-}ox,\ 11}$ (**Tables S11-S3**). To further validate these theoretical findings with experimental data, we studied the secondary structure of all peptides in HEPES buffer in the absence of gold (unadsorbed state).

Circular dichroism (CD) spectra indicate that all peptides exhibit polyproline II secondary structure (**Figure 26**, **Figure S69**). We calculated the Ramachandran plot for each peptide in the unadsorbed state, based on the entire REST-MD trajectory in each case. Consistent with the CD spectra, every peptide was predicted to feature a substantial contribution from the polyproline II secondary structure (**Table S14**).

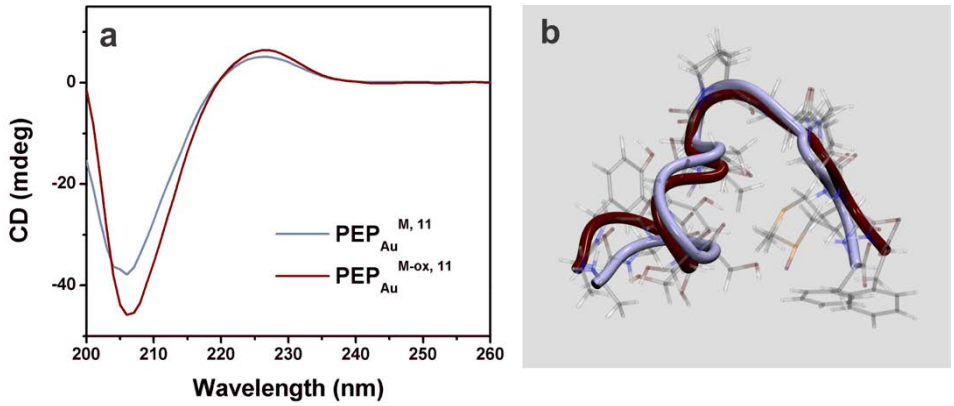

Figure 26. Representative secondary structure analysis of $PEP_{Au}^{M,\ 11}$ and $PEP_{Au}^{M\text{-}ox,\ 11}$. (a) CD measurements indicate that both $PEP_{Au}^{M,\ 11}$ and $PEP_{Au}^{M\text{-}ox,\ 11}$ exhibit predominantly PPII secondary conformations in solution. (b) Structural similarlity between $PEP_{Au}^{M,\ 11}$ (blue) and $PEP_{Au}^{M\text{-}ox,\ 11}$ (red) sequences gathered via theoretical cross-peptide analysis.

Encouraged by the effects of peptide C-terminus modification on individual AuNP size, we next investigated the effects of the methionine-based modification on the size of component AuNPs within the helical superstructures. Azido-modified mutant peptide conjugates were synthesized, e.g, N_3-AYSSGAPPM^{ox}PPF, coupled to a dialkyne modified C_{18} aliphatic tail via copper catalyzed click chemistry (**Figure S66**, refer to experimental section for details). Unoxidized peptide conjugates (C_{18}-$(PEP_{Au}^{M,\ 7})_2$, C_{18}-$(PEP_{Au}^{M,\ 9})_2$, and C_{18}-$(PEP_{Au}^{M,\ 11})_2$) and oxidized peptide conjugates (C_{18}-$(PEP_{Au}^{M\text{-}ox,\ 7})_2$, C_{18}-$(PEP_{Au}^{M\text{-}ox,\ 9})_2$, and C_{18}-$(PEP_{Au}^{M\text{-}ox,\ 11})_2$) were subjected to our established AuNP assembly conditions. C_{18}-$(PEP_{Au}^{M,\ 7})_2$, C_{18}-$(PEP_{Au}^{M,\ 9})_2$, and C_{18}-$(PEP_{Au}^{M,\ 11})_2$ all yield 1-dimensional AuNP assemblies with irregular helicity (**Figure 27**,

S70). The overall superstructure morphology observed in these cases is consistent with our previous studies on unoxidized peptide conjugates comprising of two PEP_{Au} sequences. In all three cases, the assemblies are composed of primarily spherical particles. The average diameter of component AuNPs in C_{18}-$(PEP_{Au}{}^{M,\,7})_2$ and C_{18}-$(PEP_{Au}{}^{M,\,9})_2$ is measured to be 8.1 ± 1.9 nm and 9.0 ± 1.8 nm, respectively. Interestingly, a large majority of helical superstructures derived from C_{18}-$(PEP_{Au}{}^{M,\,11})_2$ are composed of spherical particles that have larger average diameters equal to 12.3 ± 1.7 nm nm. However, we do note that a minor product, observed via TEM, in the C_{18}-$(PEP_{Au}{}^{M,\,11})_2$-based particle assembly are superstructures comprising smaller spherical particles with average diameter equal to 6.4 ± 1.1 nm (**Figure S71**). We acknowledge that to gain a better understanding of these observations, a robust binding model of gold nanoparticle and peptide fiber needs to be developed.

Before studying the assembly of AuNPs via the oxidized peptide conjugates, we proceeded to confirm the morphology of the C_{18}-$(PEP_{Au}{}^{M\text{-}ox,\,7})_2$ and C_{18}-$(PEP_{Au}{}^{M\text{-}ox,\,11})_2$ fibers. AFM microscopy revealed that C_{18}-$(PEP_{Au}{}^{M\text{-}ox,\,7})_2$ and C_{18}-$(PEP_{Au}{}^{M\text{-}ox,\,11})_2$ self-assemble into helical ribbons with average helical pitch values of 91 ± 6 nm and 93 ± 7 nm (**Figure S72**). This data confirmed that the position of M-ox within the peptide C-terminus does not affect the morphology of the helical ribbons. Well-defined single-helical superstructures are observed in C_{18}-$(PEP_{Au}{}^{M\text{-}ox,\,9})_2$ and C_{18}-$(PEP_{Au}{}^{M\text{-}ox,\,11})_2$-based AuNP assembly syntheses (**Figure 27**, **Figure S74**), while no assemblies were observed in the case of C_{18}-$(PEP_{Au}{}^{M\text{-}ox,\,7})_2$ (**Figure S73**). The component AuNPs comprising the single-helical superstructures are oblong in shape, presumably because of the weaker interaction of the oxidized peptide conjugate with gold nanoparticle surface. The average length and width of AuNPs comprising the helices constructed via via C_{18}-$(PEP_{Au}{}^{M\text{-}ox,\,9})_2$ is measured to be 15.5 ± 3.5 nm and 8.8 ± 2.5 nm, respectively. Interestingly, C_{18}-$(PEP_{Au}{}^{M\text{-}ox,\,11})_2$

yields single helices with larger component AuNPs. The average AuNP length and width measured in this case is equal to 20.5 ± 3.1 nm and 8.3 ± 1.8 nm, respectively. Although the inability of C_{18}-($PEP_{Au}^{M\text{-}ox,\ 7}$)$_2$ to direct the assembly single-helical superstructures warrants further investigation, the observed trends in NP size support our claim that the proximity of M-ox to the C-terminus can be varied to affect particle metrics.

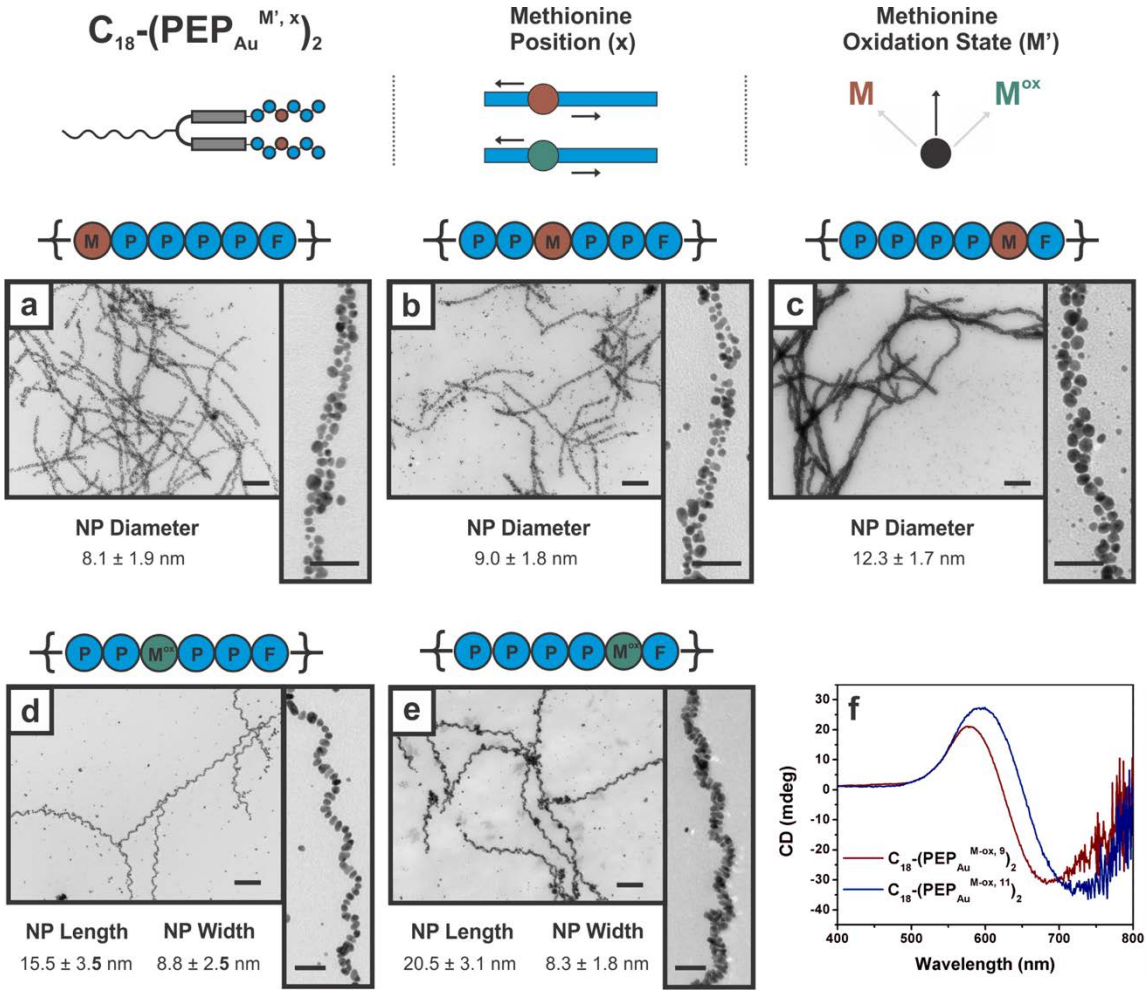

Figure 27. Effect of methionine modification on the size and shape of component AuNPs within helical superstructures. TEM analysis of 1-D superstructures exhibiting irregular helicity constructed via (a) C_{18}-($PEP_{Au}^{M,\ 7}$)$_2$, (b) C_{18}-($PEP_{Au}^{M,\ 9}$)$_2$, and (c) C_{18}-($PEP_{Au}^{M,\ 11}$)$_2$. Average NP diameters (based on ~100 counts) of component NPs in each case are listed below corresponding TEM image. TEM characterization of single-helical AuNP superstructures synthesized in the presence of (d) C_{18}-($PEP_{Au}^{M\text{-}ox,\ 9}$)$_2$ and (e) C_{18}-($PEP_{Au}^{M\text{-}ox,\ 11}$)$_2$. Helices constructed via C_{18}-($PEP_{Au}^{M\text{-}$

$^{ox,\ 11})_2$ comprise larger oblong particles (based on ~100 counts) as compared to C_{18}-($PEP_{Au}^{M\text{-}ox,\ 9}$)$_2$-based helices. (f) Chiroptical signal derived from C_{18}-($PEP_{Au}^{M\text{-}ox,\ 11}$)$_2$-based is helices is more intense compared to the signal derived from C_{18}-($PEP_{Au}^{M\text{-}ox,\ 9}$)$_2$-based helices. Low magnification image scale bar: 200 nm; high magnification scale bar: 50 nm.

Ultimately, our primary motive in this work is to vary the chiroptical signal intensity of helical AuNP superstructures via small molecular changes to the peptide sequence. In theory, single-helical superstructures comprising large oblong particles should exhibit intense optical chirality measured by their CD signal and anisotropy factor (*g*). We have previously reported that single helices derived from C_{18}-($PEP_{Au}^{M\text{-}ox,\ 9}$)$_2$ exhibit a *g*-factor ~ 0.017. In order to obtain higher g-factor values in this system, modified synthetic conditions are required to increase AuNP size. Interestingly, helices derived from C_{18}-($PEP_{Au}^{M\text{-}ox,\ 11}$)$_2$ that comprise larger oblong particles, simply due to a shift in M-ox position, display a more intense CD signal (**Figure 27**). The corresponding absolute *g*-factor is measured to be ~ 0.37. We acknowledge the possibility that further optimization of synthetic conditions might result in even higher *g*-factor values.

4.3 Conclusion

We successfully demonstrated that encoding chemical information in PEP_{Au}-based assembly agents via sequence engineering is a highly effective method for altering nanoscale structure and also optimizing the optical properties of helical AuNP assemblies. By combining theory and experiment, we identify the effects of methionine-based molecular transformations on PEP_{Au}-gold surface interaction. Ultimately, the differential gold-binding ability of the various

peptide conjugates is manifested in the difference in the nanoscale structure of helical AuNP superstructures.

4.4 Experimental Methods

4.4.1 General Methods

All chemicals were obtained from commercial sources and used without further purification. All peptides were synthesized using established microwave assisted solid phase peptide synthesis protocols on a CEM Mars microwave. Nanopure water (18.1 mΩ) from Barnstead DiamondTM water purification system was used to prepare all aqueous solutions. Peptides were purified by reverse-phase high-performance liquid chromatography on Agilent 1200 liquid chromatographic system equipped with diode array and multiple wavelength detectors using a Zorbax-300SB C_{18} column. Peptide masses were confirmed by liquid chromatography-mass spectrometry (LC-MS) data using Shimadzu LC-MS 2020. UV-Vis spectra were collected using an Agilent 8453 UV-Vis spectrometer with a quartz cuvette (10 mm path length). All microscopy measurements were made using Image J software.

4.4.2 Synthesis

Peptide Synthesis: Both unoxidized peptides ($PEP_{Au}^{M,\ x}$) and unoxidized peptides ($PEP_{Au}^{M\text{-}ox,\ x}$) were synthesized via established microwave assisted solid phase peptide synthesis protocol. Briefly, 138.8 mg (0.025 mmol) of Fmoc-Phe-NovasynR TGA resin was soaked in DMF

for 15 minutes. Fmoc-deprotection of the resin was performed by adding 2 mL of 20% 4-methylpiperidine in DMF to the resin and heating the mixture to 75 °C in 1 minute and holding for 2 minutes. Excess reagent was drained using a filtration manifold and washed with copious amounts of DMF. To couple individual amino acids, 0.1 M solution of HCTU in NMP (5 equivalents to resin, 1.25 mL) was added to Fmoc-protected amino acid (4 equivalents, 0.125 mmol) followed by DIEA (7 equivalents, 0.175 mmol, 30.4 μL). The resulting solution was vortexed and centrifuged to ensure complete dissolution of amino acid. Thereafter, the solution was transferred to resin and heated to 75 °C for 1 minute and held for 5 minutes. Excess reagent was then again drained and the resin was washed with DMF. This cycle was reactions were repeated for every amino acid. Proline and adjacent amino acid were coupled twice to ensure complete reaction of secondary amide group. In the final step, the N-terminus was deprotected. For preparing azido-modified peptides, 5-azidopentanoic acid was coupled to the N-terminus.

Peptide Conjugate Synthesis: C_{18}-dialkyne was attached to each azido peptide sequence via Cu-catalyzed click chemistry which is described in chapter 2.

4.4.3 NP Synthesis and Assembly

Discrete NP Synthesis: Synthetic conditions used to prepare discrete AuNPs in the presence of peptides were based on a previously established protocol. $PEP_{Au}^{M,\,x}$ and $PEP_{Au}^{M\text{-}ox,\,x}$ (x = 7, 9, 11) were dissolved in 250 μL 0.1 M HEPES. Next, 2 μL 0.1 M $HAuCl_4$ solution was added to the peptide-HEPES mixture. The reaction mixture was quickly vortexed after observance of a localized black precipitate (~ 4-5 s after adding the gold source) and thereafter the reaction vial was left undisturbed on the bench.

NP Superstructure Assembly: 18.725 nmol of C_{18}-($PEP_{Au}^{M, x}$)$_2$ and C_{18}-($PEP_{Au}^{M\text{-}ox, x}$)$_2$ (x = 7, 9, 11) were dissolved in 250 μL of 0.1 M HEPES buffer, sonicated for 5 minutes and allowed to sit for 25 minutes. Thereafter, 2 μL of 1:1 mixture of aqueous 0.1 M $HAuCl_4$ in 1 M TEAA buffer was added to the peptide-HEPES mixture. About 2-3 seconds after addition of gold precursor solution, a localized black precipitate emerged which was rapidly vortexed. The reaction vial was thereafter left undisturbed on the bench.

4.4.4 Characterization and Sample Preparation

Circular Dichroism Spectroscopy: CD measurements were performed on Olis DSM 17 CD spectrometer with a quartz cuvette (0.1 cm path length) at 25 °C with 8 nm/min scan rate. The PMT values ranged from 700-250V (200-280 nm). High PMT values observed close to 200 nm are due to HEPES absorption. The integration time was 5 sec. C_{18}-($PEP_{Au}^{M, x}$)$_2$ and C_{18}-($PEP_{Au}^{M\text{-}ox, x}$)$_2$ (x = 7, 9, 11) were dissolved in 250 μL of 10 mM HEPES. The chiroptical properties of single helices derived from C_{18}-($PEP_{Au}^{M\text{-}ox, 9}$)$_2$ and C_{18}-($PEP_{Au}^{M\text{-}ox, 11}$)$_2$ dissolved in 250 μL of 0.1 M HEPES were taken and measured directly after ~16 hrs of reaction.

Atomic Force Microscopy: AFM measurements were performed in tapping mode using Asylum MFP-3D atomic force microscope and ultrasharp AFM tips (NanoandMore SHR-150). 0.1% APTES (3-aminopropyl-triethoxy-silane) solution was drop casted onto a freshly cut mica surface, followed by rinsing with Nanopure water. C_{18}-($PEP_{Au}^{M\text{-}ox, 7}$)$_2$ and C_{18}-($PEP_{Au}^{M\text{-}ox, 11}$)$_2$ were dissolved in 250 μL 0.1 M HEPES to yield a 75 μM solution. Next, 50 μL of the solution was drop cast and rinsed with water after 1 minute and allowed to dry in the desiccator overnight.

Transmission Electron Microscopy: TEM was conducted on a FEI Morgagni 268 operated at 80 kV and equipped with an AMT side mount CCD camera system. 6 μL of peptide conjugate solution were drop casted onto a 3 mm-diameter copper grid with formvar coating (Electron Microscopy Sciences; FCF300-CU). After 5 minutes, excess solution was wicked away and the grid was air-dried for 2 minutes. Thereafter, 6 μL of Nanopure water was drop cast onto the grid and allowed to sit for 30 seconds. Excess solution was wicked away and the grid was allowed to air-dry for 5 minutes.

4.4.5 Molecular Simulations

Replica-Exchange with Solute Tempering Molecular Dynamics Simulations: REST-MD simulations[97,98] were used to predict the Boltzmann-weighted ensemble of configurations for each of the six peptide sequences, in both the surface-adsorbed and unadsorbed states. Each unadsorbed simulation comprised one of the six peptides and liquid water Each surface-adsorbed simulation comprised these and also an Au surface, modeled as an Au(111) slab four atomic layers thick. The Au(111) substrate has been previously demonstrated to be an effective approximation for more complex Au surfaces.[100,102,103] The peptide, Au surface, and water were modeled using the CHARMM-22*,[104,105] GolP-CHARMM[99] and modified TIP3P[106,107] potentials respectively. Periodic boundary conditions were used in 3D. Frames were saved from each trajectory every 1ps. These trajectories were analyzed using clustering with respect to the relative positions of the peptide backbone atoms. In addition, for the surface-adsorbed simulations we applied a residue-surface contact analysis which yielded the percentage of frames that each residue was in contact with the surface. Full details of the simulations and analyses are provided in Appendix C.

First Principles Calculations: Plane-wave density functional theory calculations were carried out for dimethyl sulfoxide adsorbed onto the Au(111) surface in vacuo, using Quantum Espresso (v5.2.0).[108] Three-dimensional periodic boundary conditions were employed using a $3 \times 3\sqrt{3}$ supercell and a Au slab four atomic layers thick. Calculations were performed using vdW-DF[93,94,95] with the revPBE exchange-correlation functional.[109] The binding energy of dimethyl sulfoxide was determined via two stages; a geometry optimization followed by a single point energy calculation of the resultant geometry. The binding energy was calculated using the supermolecule approach. Full details are provided in Appendix C.

5.0 Deliberate Introduction of Particle Anisotropy in Helical AuNP Superstructures

This work, written in collaboration with Nathaniel L. Rosi*, is reprinted with permission from *Particle and Particle Systems Characterization* **2019**, *36*, 1800504. Copyright 2019, Wiley. The supporting information is found in Appendix D.

5.1 Introduction

Advances in seed-mediated NP synthesis, wherein small seed particles grow into larger morphologically distinct NPs, have yielded a rich library of NPs that exhibit shape-dependent optical properties.[110-115] Triangular NPs (i.e 'nanoprisms'),[116,117,118] which are typically synthesized via seed-mediated approaches, are highly efficient at localizing electromagnetic 'hotspots' at their surface edges and corners,[119,120,121] and these 'hotspots' can be harnessed for wide-ranging applications including surface enhanced Raman spectroscopy (SERS) sensing,[122,123] cellular imaging,[124] and chemical catalysis.[125] Further, it is known that the localized electromagnetic fields are intensified at interparticle gaps (e.g. gap between two corners of adjacent nanoprisms).[126,127,128] Assembly methods that may serve to couple such particles together in close proximity are needed to realize and optimize some of their optoelectronic and catalytic properties. Various NP assembly methods have been developed to prepare well-defined NP superstructures.[129,130,72] Bottom-up methods generally include the attachment and organization of discrete NPs, typically spheres and rods, onto pre-fabricated soft scaffolds (DNA, peptide, or polymer). However, few reports demonstrate the assembly of NPs with sharp edges (e.g.

nanoprisms) into three-dimensional architectures.[131,132] This may be achieved by combining seed-mediated NP synthesis with scaffold-directed NP assembly, whereby scaffold materials decorated with particle seeds serve as precursor assemblies for myriad exotic NP superstructures composed of various NP shapes.

The properties of chiral NP superstructures are dependent on several structural parameters of the helix including the size and shape of the component NP shape. As with other NP assemblies, most reported chiral NP assemblies consist of spherical NPs or nanorods.[32] Currently, chiral structures assembled using other NP shapes have yet to be prepared and their effect on the chiroptical read-out of these materials is not known. We are therefore motivated to develop synthetic strategies for altering the shape of component NPs within a chiral NP superstructure. Ionic surfactants, e.g. cetyltrimethylammonium bromide (CTAB) and its analogs, are employed extensively in the syntheses of anisotropic NPs.[111,133] In this chapter, we demonstrate how a series of CTAB molecules can alter the shape of component NPs within a chiral NP assembly. Specifically, we investigate the effect of CTAB alkyl chain length on the final shape of the constituent NPs. This study provides valuable insights into the construction of chiral NP assemblies composed of various particle shapes.

5.2 Results and Discussion

The synthesis of AuNP single helices using C_{18}-$(PEP_{Au}^{M\text{-}ox})_2$ involves the *in situ* reduction of Au ions into AuNPs and their simultaneous incorporation into the helical fiber assembly. At very early stages of the assembly process, small AuNPs (~3 nm) are bound to the helical fiber. Over time, the particles on the helices grow larger and become oblong and rod-shaped.[22] We

therefore hypothesize that introduction of external shape controlling agents at very early stages of assembly will affect the final shape of AuNPs on the surface of the helical fiber (**Figure 28**). As a first step toward realizing this objective, we study here the effect of CTAB molecules on NP shape in the context of the single helix synthesis. We envision that this strategy could lead to the construction of a variety of chiral NP superstructures composed of different NP shapes.

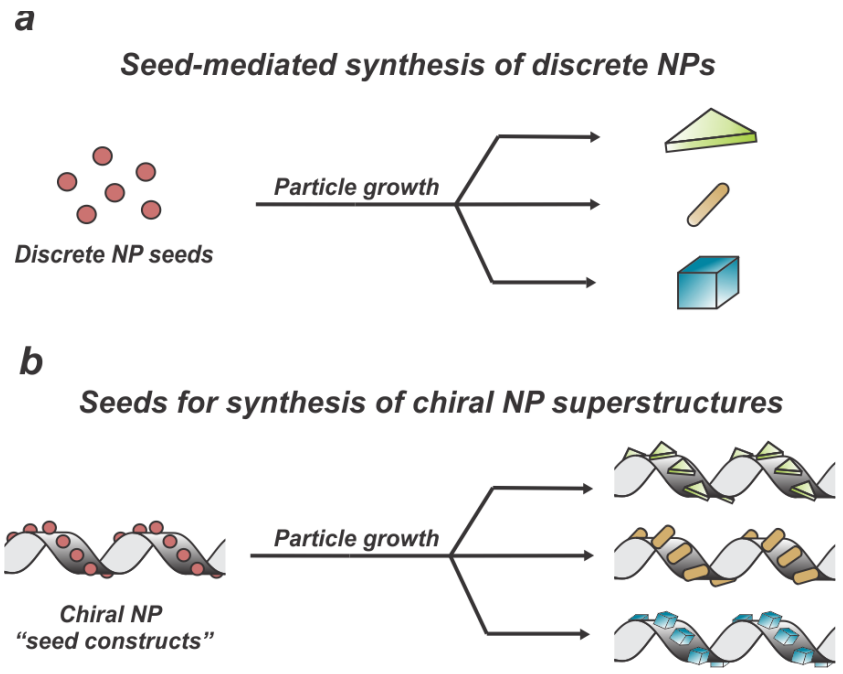

Figures 28. (a) Illustration depicting the seed-mediated synthesis of morphologically different NPs. (b) A synthetic strategy similar to (a) is envisioned for the synthesis of chiral NP superstructures varying in the shape of component NPs.

In order to identify ideal synthetic conditions for controlling AuNP shape in single-helical superstructures, we focused on determining i) the most suitable shape controlling reagent, and ii) the appropriate reagent concentration. The peptide-based synthesis of discrete, unassembled AuNPs is similar to the synthesis of AuNP single helices. During the synthesis of discrete AuNPs, gold-binding PEP_{Au} caps the surface of small particles formed in solution, while during the synthesis of AuNP single helices, small particles formed in solution incorporate into the C_{18}-$(PEP_{Au}{}^{M\text{-}ox})_2$ helical fiber assembly. In both cases, the particles grow larger as the reaction proceeds

and the gold ion source is consumed. Due to the similarities between the two syntheses, we began by examining shape control in the synthesis of discrete NPs. In a typical synthesis, AuNPs are synthesized by dissolving PEP_{Au} in 0.1 M HEPES buffer (pH = 7.3) and then adding to this solution an aliquot of 0.1 M $HAuCl_4$. We first explored how NH_4Br, the simplest bromide-based ammonium ionic salt, affects the size and shape of discrete AuNPs at different concentrations (**Figure S76**). In the absence of NH_4Br, transmission electron microscopy (TEM) revealed that the average diameter of the resulting spherical NPs increases from ~4 nm after 5 minutes of reaction to 6.9 ± 1.3 nm after ~16 hours (**Figure 30**). To affect NP growth at very early stages, an aliquot of 0.1 M NH_4Br solution was added to the reaction vial immediately after the reduction of Au ions. Three different NH_4Br concentrations were examined: 100 μM, 400 μM, and 1000 μM (**Figure S76)**. After ~16 hours, the average particle sizes at these NH_4Br concentrations were 7.6 ± 1.3 nm, 13.1 ± 1.6 nm, and 10.9 ± 2.4 nm, respectively. In the presence of 400 μM and 1000 μM NH_4Br, large NPs with prominent sharp facets are observed (**Figure S76**). Further, some NPs adopt either prismatic or hexagonal structure, which was not observed in the absence of NH_4Br. These results are in line with previous literature reports, wherein bromide ions serve as modulators to sharpen the corners and edges of discrete NPs (e.g. Ag and Au).[134] These initial experiments suggest that higher concentrations (e.g. 1000 μM) of bromide-based external agents are required for affecting the final NP shape.

We next examined the effect of a series of CTAB analogs on the final shape of discrete AuNPs synthesized in the presence of PEP_{Au}. Murphy et al. previously demonstrated that the alkyl tail length of CTAB molecules can dramatically affect AuNPs shape and aspect ratio.[135] We therefore selected four CTAB analogs, denoted here by the length of their aliphatic tail: $C_{10}TAB$, $C_{12}TAB$, $C_{14}TAB$, and $C_{16}TAB$. Following the same procedure described above, an aliquot of each

CTAB analog was added to separate PEP_{Au}-HEPES reaction mixtures immediately following the reduction event to make the final CTAB concentration in each reaction vial 1000 μM. In the case of C_{10}TAB and C_{12}TAB, spherical particles are observed as the major product along with a few large hexagonal NPs (**Figure S77**). However, in the case of C_{14}TAB and C_{16}TAB, prominent Au nanoprisms are observed with an average edge length equal to 11.9 ± 2.9 nm (**Figure 30b, Figure S77**). Overall, the yield of the anisotropic AuNPs increases with increase in C_nTAB tail length (**Figure 29**).

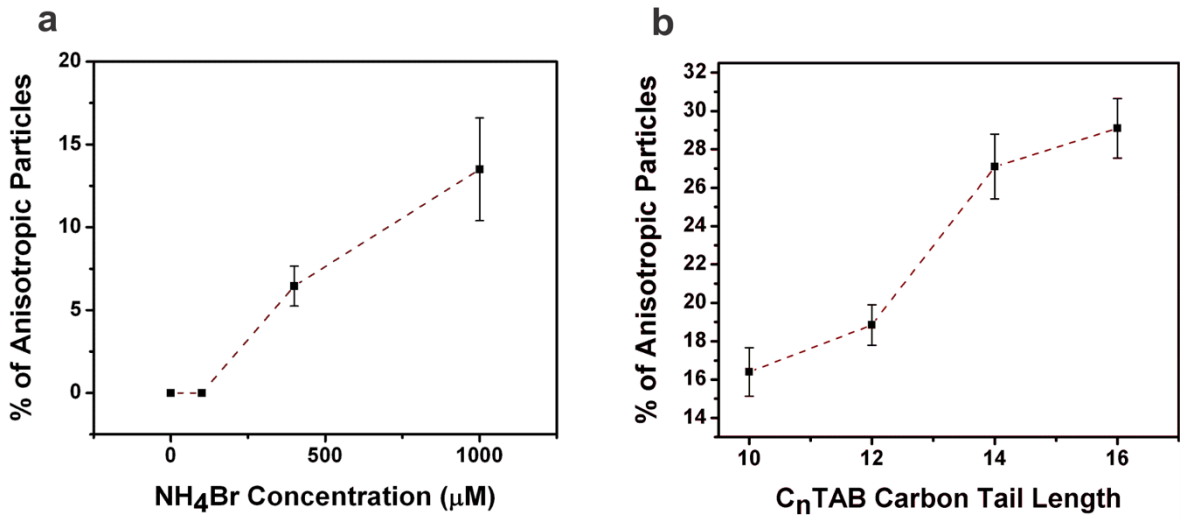

Figures 29. The percentage of anisotropic AuNPs observed in discrete particle syntheses plotted as a function of (a) NH_4Br concentration, and (b) C_nTAB carbon tail length (based on ~200 counts).

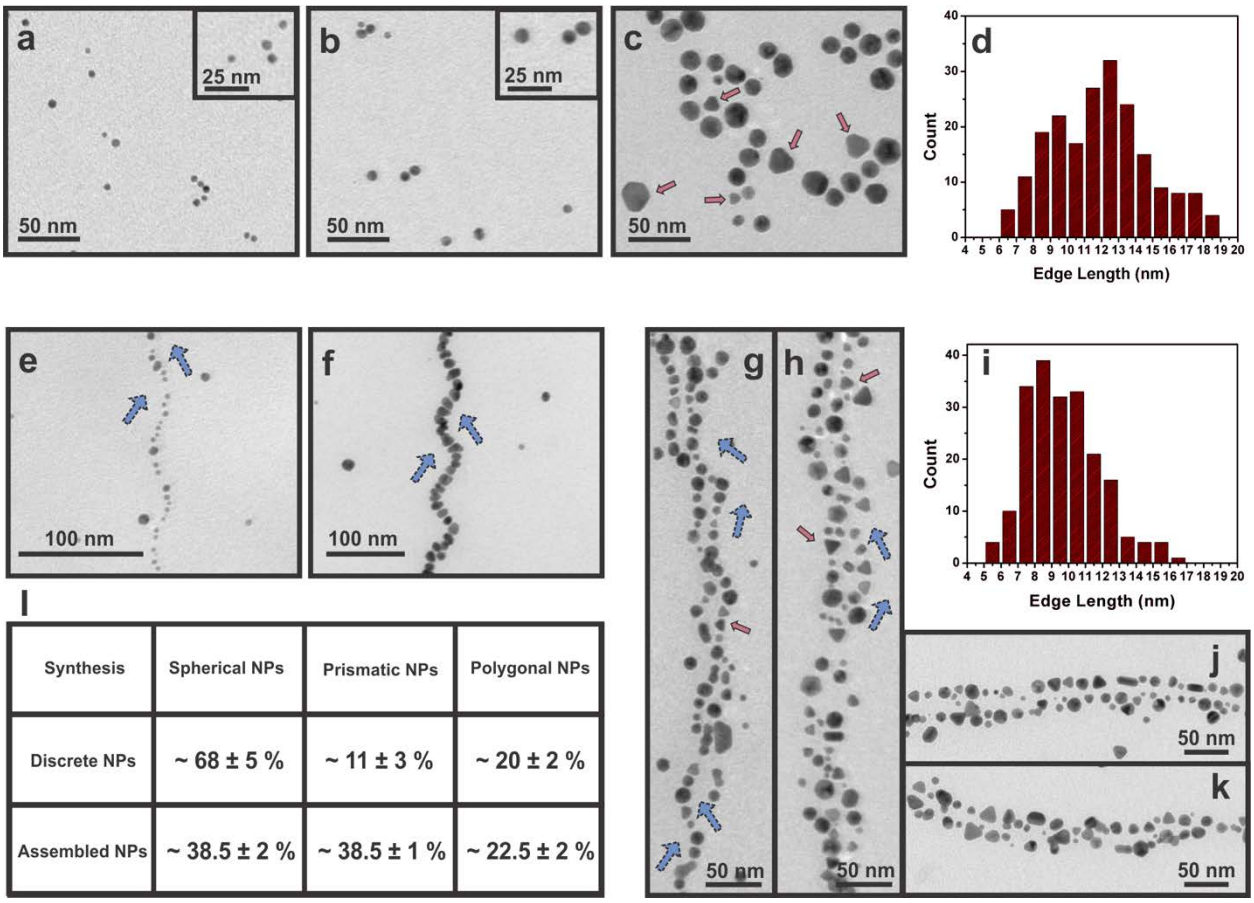

l

Synthesis	Spherical NPs	Prismatic NPs	Polygonal NPs
Discrete NPs	~ 68 ± 5 %	~ 11 ± 3 %	~ 20 ± 2 %
Assembled NPs	~ 38.5 ± 2 %	~ 38.5 ± 1 %	~ 22.5 ± 2 %

Figures 30. Effect of C_{16}TAB on the synthesis of discrete AuNPs and helical AuNP superstructures. Spherical AuNPs synthesized in the presence of PEP_{Au} imaged at (a) 5 minutes and (b) 16 hours after reduction of Au ions. (c) AuNPs synthesized in the presence of PEP_{Au} and 1000 μM C_{16}TAB. Here, Au nanoprisms (red arrows) are observed along with other discrete spherical NPs. (d) Edge length distribution of discrete Au nanoprisms prepared in the presence of C_{16}TAB. C_{18}-$(PEP_{Au}^{M\text{-}ox})_2$-mediated assembly of chiral AuNP single helices images at (e) 5 minute and (f) 16 hours after the reduction of Au ion precursors (blue arrows indicate helical directionality). (g, h) Helical NP superstructures observed after the addition of C_1TAB to helices observed in (e). (i) Edge length distribution of Au nanoprisms within the superstructures. (j, k) Additional images of helical superstructures synthesized in the presence of C_{16}TAB. (l) Average percentage distributions of spherical, prismatic, and polygonal NPs observed in the C_{16}TAB-based synthesis of discrete NPs and helical superstructures (based on ~200 counts).

Since both C_{10}TAB and C_{16}TAB exhibit vastly different effects on NP shape, we next examined their influence on NP shape within AuNP single helix syntheses. We measured the average size of AuNPs at different time points in the single helix synthesis (**Figure S78**). After 5 minutes, the single helices consist of spherical particles with an average diameter of 3.5 ± 0.5 nm (**Figure S78**), which represent an ideal size for 'seed' particles in anisotropic NP synthesis.[133] We therefore decided to add the CTAB doses after 5 minutes of reaction. Aliquots of C_{10}TAB and C_{16}TAB were each added to separate reaction vials, such that the final concentration of C_{10}TAB and C_{16}TAB was 1000 μM. The contents of the reaction vial were analyzed via TEM after 16 hours of reaction. In the absence of CTAB, the AuNPs comprising the single helices are oblong (**Figure 30f, S79**). However, in the presence of C_{10}TAB, most particles comprising the single-helical superstructures are spherical, although a few particles adopt prismatic geometries (**Figure S80**). Interestingly, in the case of C_{16}TAB, a large number of particles adopt a variety of shapes with sharp edges (**Figure 30g, h, j, k, S81**). ~60% of the constituent NPs are anisotropic (based on ~200 counts), with ~38% adopting prismatic geometry and ~22% adopting other polygonal geometries (**Figure 30l**). We speculate that compared to the relatively lower conversion percentages observed in the case of discrete nanoprism synthesis, these observed higher percentages indicate that the synthesis of nanoprisms is more efficient when the particle seeds are anchored to the peptide fiber surface. The average edge length of the prismatic particles is 9.7 ± 1.8 nm (**Figure 30i**), which is smaller than most other Au nanoprism syntheses reported in the literature.[131,132,136] It is interesting to note that in the presence of C_{16}TAB, the overall morphology of the NP superstructures changes from single helices to ostensibly aggregated or intertwined helical assemblies (**Figure 30g, h, j, k, S82**). This observation is consistent with our previous studies where the assembly of chiral AuNP single helices was affected by external ionic agents such as $CaCl_2$. Negatively-stained TEM

samples reveal that the aggregated assemblies result from bundling of the C_{18}-$(PEP_{Au}{}^{M\text{-}ox})_2$ fibers (**Figure S82**). Negative staining experiments further revealed that C_{18}-$(PEP_{Au}{}^{M\text{-}ox})_2$ in the presence of C_{16}TAB alone also exhibits fiber bundling (**Figure S82**). In order to further investigate the effect of C_{16}TAB on AuNP assembly, we doubled the final concentration of the C_{16}TAB aliquot added to the single helix synthesis. Increasing [C_{16}TAB] appears to decrease the helicity of the resultant superstructures, yet it does not significantly affect the observed percentage of spherical and anisotropic AuNPs (**Figure S83**). We conclude from these experiments that C_{16}TAB has a two-fold effect on the assembly process: i) it affords the anisotropic growth of small component AuNPs within the helical superstructures, and ii) it promotes fiber bundling, leading to the formation of intertwined helical AuNP superstructures and, at higher concentrations, superstructures with apparent decreased helicity.

We have previously reported the assembly of a variety of helical AuNP superstructures, comprising either spherical or oblong AuNPs, which exhibit strong chiroptical activity.[22,50] Therefore, we were motivated to study the optical properties of these AuNP superstructures that consist of prismatic and other anisotropic AuNPs. However, at this stage, these assemblies do not exhibit a discernible chiroptical response at the plasmon wavelength (**Figure S84)**. We speculate that this could be due to decreased helicity caused by fiber bundling or lower synthetic yields of the superstructures.

5.3 Conclusions

We have introduced deliberate particle anisotropy in a chiral assembly of AuNPs. Individual particles within the chiral single-helical superstructure grow from small spherical NPs

to oblong NPs. By adding external CTAB surfactants, the final anisotropic particle shape can be modulated from oblong to prismatic. These results demonstrate that single helices consisting of small seed particles can serve as progenitor species for accessing multiple different helical superstructures comprising various anisotropic AuNPs. We anticipate that this strategy could be adapted and generalized for constructing chiral NP architectures using other assembly methods where attachment of anisotropic AuNPs to scaffold materials may be challenging.

5.4 Experimental Methods

5.4.1 General Methods

All chemicals were purchased from commercial vendors and used without purification. Nanopure water (18.1 mΩ) was obtained using a Barnstead DiamondTM water purification system. Peptides and peptide conjugates were synthesized using a CEM MARS 6TM synthesis microwave reactor and purified using Agilent 1200 reverse-phase high-performance liquid chromatography (RP-HPLC) system consisting of multiple wavelength detectors and a Zorbax-300SB C_{18} column. A linear gradient of 5-95% acetonitrile over 30 min was used to elute peptide samples. Liquid chromatography-mass spectrometry (LC-MS) was performed on a Shimadzu LC-MS 2020 system and used to confirm the mass of PEP_{Au} and C_{18}-$(PEP_{Au}^{M\text{-}ox})_2$. In order to quantify the precise amounts of peptides/peptide conjugates, UV-vis spectra were collected using an Agilent 8453 UV-vis spectrometer with a quartz cuvette (10 mm path length) at room temperature. All microscopy measurements were made using ImageJ software.

5.4.2 Particle and Helical Superstructure Synthesis

PEP_{Au}-Based Particle Synthesis: NPs were synthesized by following a previously established protocol.[68] Amine-terminated PEP_{Au} (81 nmol) was dissolved in 250 μL 0.1 M HEPES. Next, 2 μL of 0.1 M $HAuCl_4$ solution was added to the peptide-HEPES mixture. A black cloud/precipitate was observed after ~4-5 seconds, after which the reaction vial was quickly vortexed to disperse the precipitate. For examining the role of NH_4Br in affecting particle shape, 2.5 μL, 10 μL, and 25 μL of 10 mM NH_4Br solution was added to the reaction mixture after the addition of 0.1 M $HAuCl_4$. These additions yielded final NH_4Br concentrations of 100 μM, 400 μM, and 1000 μM. In the case of affecting particle shape via CTAB analogs, 25 μL of 10 mM C_nTAB in 0.1 M HEPES (n = 10, 12, 14, 16) was added to the reaction mixture after the addition of 0.1 M $HAuCl_4$. The contents of the reaction were observed via TEM after ~16 hours.

C_{18}-($PEP_{Au}^{M\text{-}ox}$)$_2$-Based Single Helix Synthesis: Chiral AuNP single helices were prepared by following our established synthetic method. Briefly, 18.725 nmol of C_{18}-($PEP_{Au}^{M\text{-}ox}$)$_2$ was dissolved in 0.1 M HEPES buffer. Next, the peptide-HEPES buffer was sonicated for 5 minutes and then allowed to sit at room temperature for 25 minutes. After 25 minutes, 2 μL of 0.1 M $HAuCl_4$ in 1M triethyl ammonium acetate (TEAA) buffer was added to the peptide-HEPES buffer. After observing a localized black precipitate, the reaction vial for vortexed to disperse the precipitate. For affecting particle shape via CTAB, 25 μL of each 10 mM C_nTAB (n= 10, 12, 14, 16) in 0.1 M HEPES was added to the separate reaction vials 5 minutes after vortexing. The contents of individual reaction vials were analyzed via TEM after ~16 hours.

5.4.3 Microscopic and Spectroscopic Characterization

Transmission Electron Microscopy: TEM imaging was performed on a FEI Morgagni 268 operated at 80 kV and equipped with an AMT side mount CCD camera system. TEM samples were prepared by drop-casting 6 μL of sample onto a 3 mm-diameter copper grid with Formvar coating (Electron Microscopy Sciences; FCF300-CU). Excess solution was wicked away after 5 minutes followed by air-drying for ~2 minutes. For studying discrete particles and AuNP helical assemblies, 6 μL of Nanopure water was added and the grid was left undisturbed for ~30 seconds. Excess water was then wicked away and the grid was allowed to air-dry for 5 min. For determining the nature of fiber scaffold underlying the NP assemblies, 6 μL of phosphotungstic acid (pH ~7.3) was drop cast onto the grid and allowed to sit for ~30 seconds. Excess solution was wicked away and the grid was air dried for 5 minutes.

Circular Dichroism Spectroscopy: CD studies of the AuNP superstructures were performed on an Olis DSM 17 CD spectrometer with a quartz cuvette (0.1 cm path length) at 25 °C. The integration time was 5 sec. Spectra were collected in 0.1 M HEPES buffer 1 day after adding gold precursor solution.

Appendix A

Supporting Information for Chapter 2: "Systematic Adjustment of Pitch and Particle Dimensions within a Family of Chiral Plasmonic AuNP Single Helices"

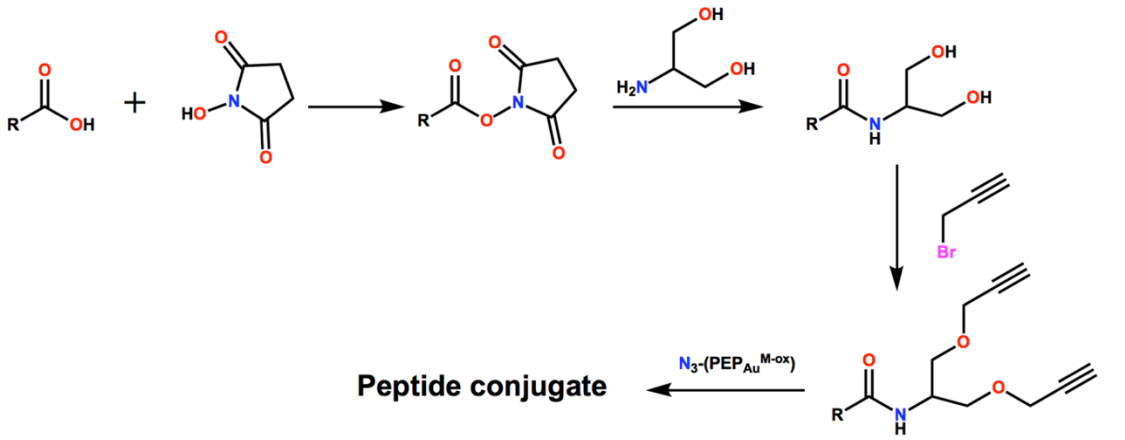

Figure S31. General synthetic scheme for the preparation of peptide conjugates.

Table S1. Mass spectrometry characterization of C_n-dialkynes (final organic small molecule).

C_n-dialkynes	Theoretical mass, M (Da)	Experimental mass, M+H (Da)
C_{14}	377.6	378.3
C_{16}	405.6	406.5
C_{18}	433.7	434.3
C_{20}	461.7	462.1
C_{22}	489.8	490.3

Synthesis of peptide conjugates and organic intermediates

$C_{14\text{-}22}$-$(PEP_{Au}{}^{M\text{-}ox})_2$, N_3-$(PEP_{Au}{}^{M\text{-}ox})$ and all organic intermediates were synthesized and purified by employing previously reported protocols.[92]

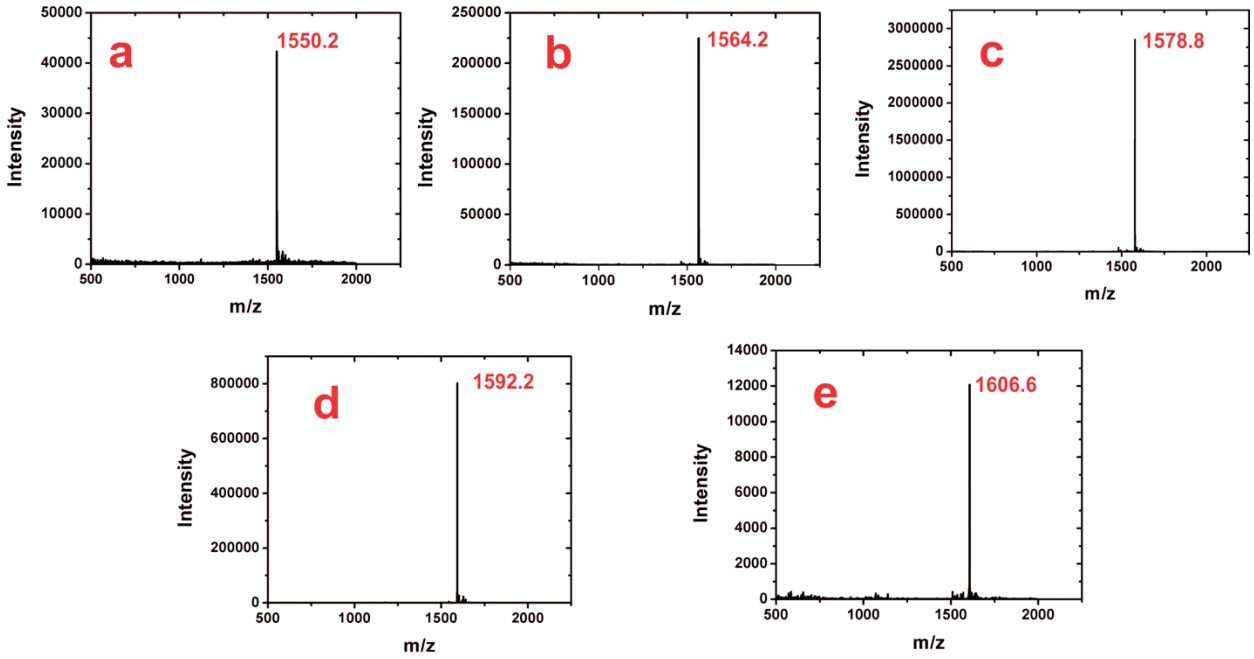

Figure S32. LC-MS mass assignment of (a) C_{14}-($PEP_{Au}^{M\text{-}ox}$)$_2$, m/z = 1550.2 Da ($M\text{-}2H^+$)/2; (b) C_{16}-($PEP_{Au}^{M\text{-}ox}$)$_2$, m/z =1564.2 Da ($M\text{-}2H^+$)/2; (c) C_{18}-($PEP_{Au}^{M\text{-}ox}$)$_2$, m/z = 1578.8 Da ($M\text{-}2H^+$)/2; (d) C_{20}-($PEP_{Au}^{M\text{-}ox}$)$_2$, m/z = 1592.2 Da ($M\text{-}2H^+$)/2; (e) C_{22}-($PEP_{Au}^{M\text{-}ox}$)$_2$, m/z = 1606.6 Da ($M\text{-}2H^+$)/2.

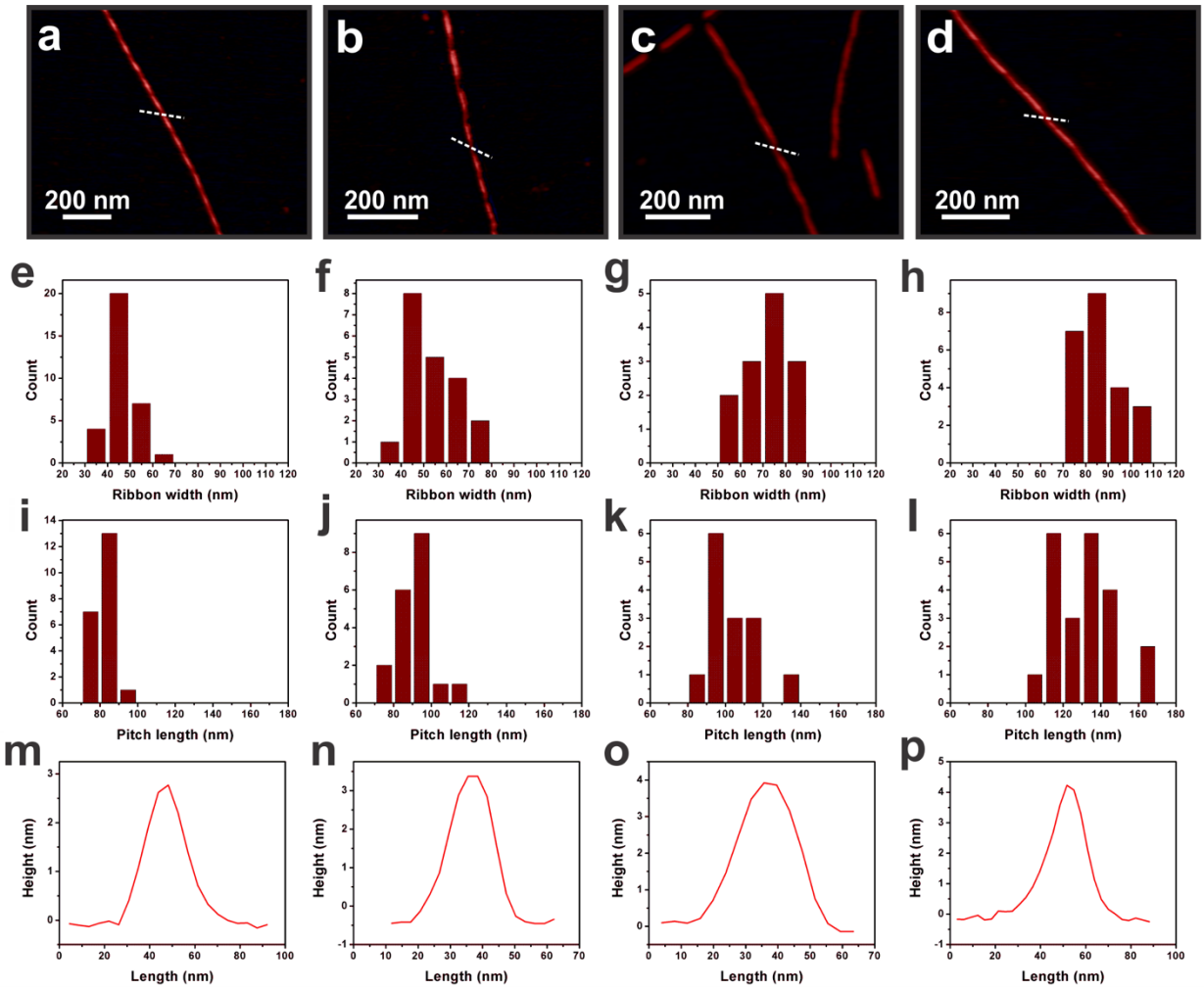

Figure S33. AFM images of (a) C_{16}-$(PEP_{Au}{}^{M\text{-}ox})_2$, (b) C_{18}-$(PEP_{Au}{}^{M\text{-}ox})_2$, (c) C_{20}-$(PEP_{Au}{}^{M\text{-}ox})_2$ and (d) C_{22}-$(PEP_{Au}{}^{M\text{-}ox})_2$ helical ribbons. Ribbon width distributions for (e) C_{16}-$(PEP_{Au}{}^{M\text{-}ox})_2$, (f) C_{18}-$(PEP_{Au}{}^{M\text{-}ox})_2$, (g) C_{20}-$(PEP_{Au}{}^{M\text{-}ox})_2$ and (h) C_{22}-$(PEP_{Au}{}^{M\text{-}ox})_2$ helical ribbons. Pitch length distributions for (i) C_{16}-$(PEP_{Au}{}^{M\text{-}ox})_2$, (j) C_{18}-$(PEP_{Au}{}^{M\text{-}ox})_2$, (k) C_{20}-$(PEP_{Au}{}^{M\text{-}ox})_2$ and (l) C_{22}-$(PEP_{Au}{}^{M\text{-}ox})_2$ helical ribbons. Ribbon thickness data (measured along dotted lines shown in a-d) for (m) C_{16}-$(PEP_{Au}{}^{M\text{-}ox})_2$, (n) C_{18}-$(PEP_{Au}{}^{M\text{-}ox})_2$, (o) C_{20}-$(PEP_{Au}{}^{M\text{-}ox})_2$ and (p) C_{22}-$(PEP_{Au}{}^{M\text{-}ox})_2$ helical ribbons.

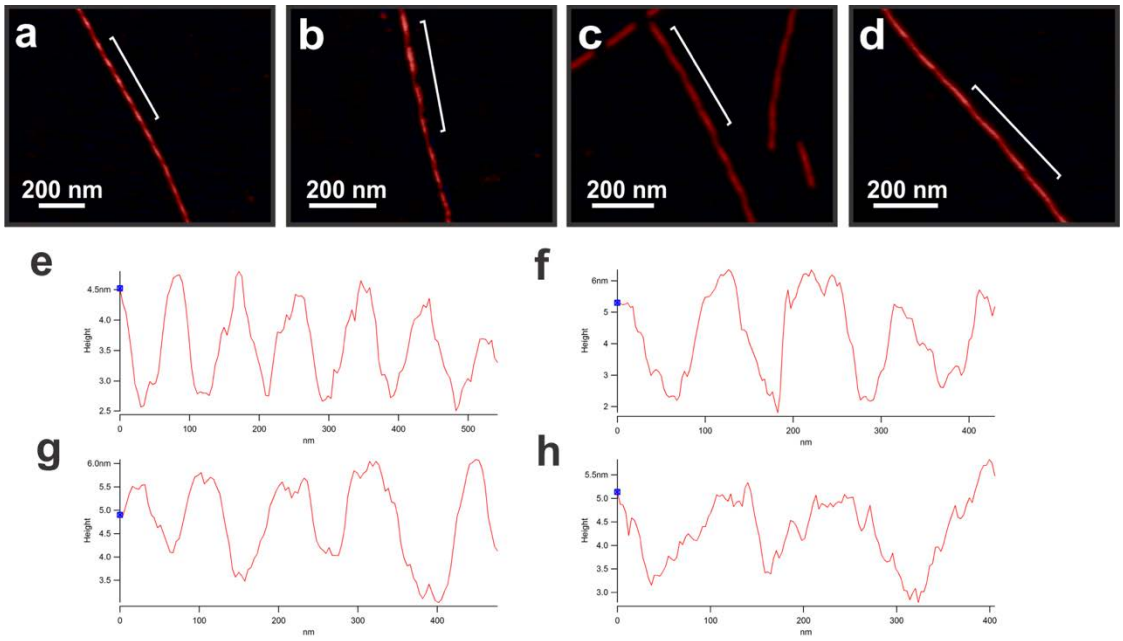

Figure S34. AFM images of (a) C_{16}-($PEP_{Au}^{M\text{-}ox}$)$_2$, (b) C_{18}-($PEP_{Au}^{M\text{-}ox}$)$_2$, (c) C_{20}-($PEP_{Au}^{M\text{-}ox}$)$_2$ and (d) C_{22}-($PEP_{Au}^{M\text{-}ox}$)$_2$ with labeled segments corresponding to height traces (e) C_{16}-($PEP_{Au}^{M\text{-}ox}$)$_2$, (f) C_{18}-($PEP_{Au}^{M\text{-}ox}$)$_2$, (g) C_{20}-($PEP_{Au}^{M\text{-}ox}$)$_2$ and (h) C_{22}-($PEP_{Au}^{M\text{-}ox}$)$_2$.

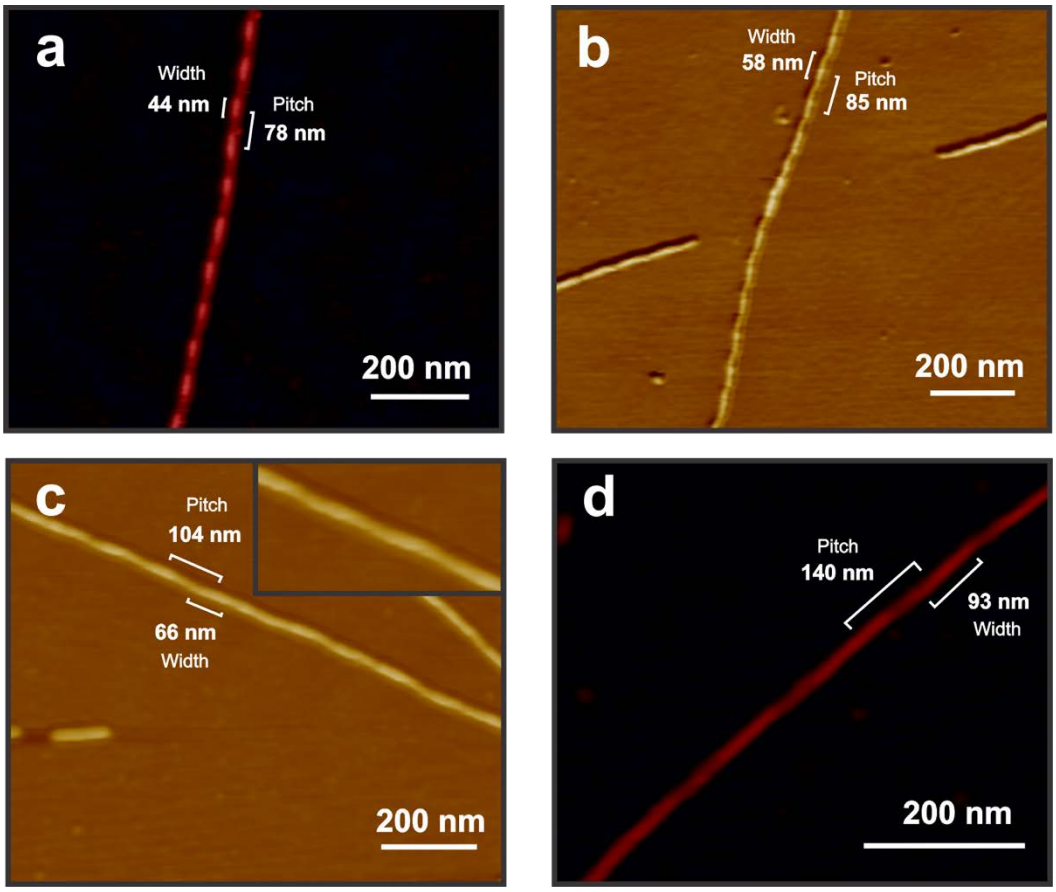

Figure S35. Additional AFM images of (a) C_{16}-$(PEP_{Au}^{M\text{-}ox})_2$, (b) C_{18}-$(PEP_{Au}^{M\text{-}ox})_2$, (c) C_{20}-$(PEP_{Au}^{M\text{-}ox})_2$ and (d) C_{22}-$(PEP_{Au}^{M\text{-}ox})_2$.

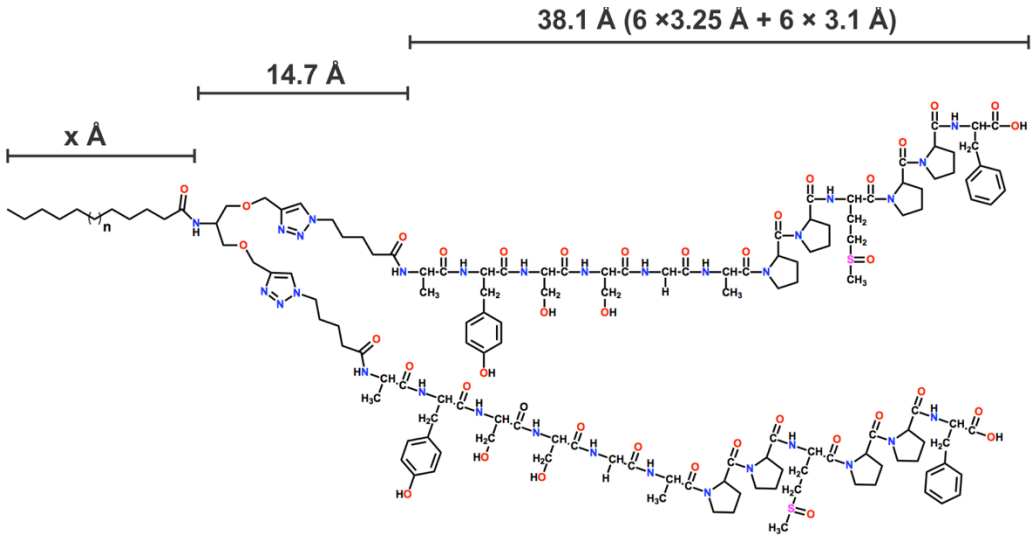

Figure S36. Length of the extended regions of peptide conjugates. The length of the peptide portion takes into account the average length spanned by one amino acid in both parallel β-sheet (3.25 Å)[3] and PPII (3.1 Å)[4] secondary structures.

Table S2. Extended length of aliphatic tails and corresponding peptide conjugate.

Aliphatic tail	Length of aliphatic tail (x Å)	Length of conjugate (nm)
C_{14}	17.4	7.0
C_{16}	19.9	7.3
C_{18}	22.4	7.5
C_{20}	24.9	7.8
C_{22}	27.4	8.0

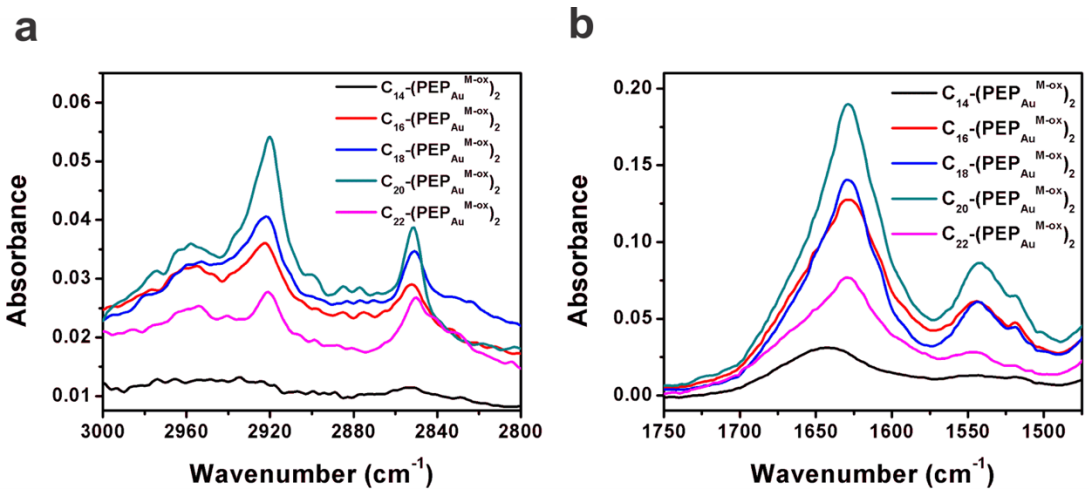

Figure S37. FTIR spectroscopy of $C_{16\text{-}22}$-$(PEP_{Au}{}^{M\text{-}ox})_2$ peptide conjugates. (a) C-H symmetric and asymmetric regions, and (b) Amide I and II regions.

Table S3. C-H symmetric and asymmetric stretch values of peptide conjugate assemblies.

Peptide conjugate	C-H symmetric stretch (cm^{-1})	C-H asymmetric stretch (cm^{-1})
C_{16}	2851	2923
C_{18}	2851	2922
C_{20}	2851	2920
C_{22}	2850	2921

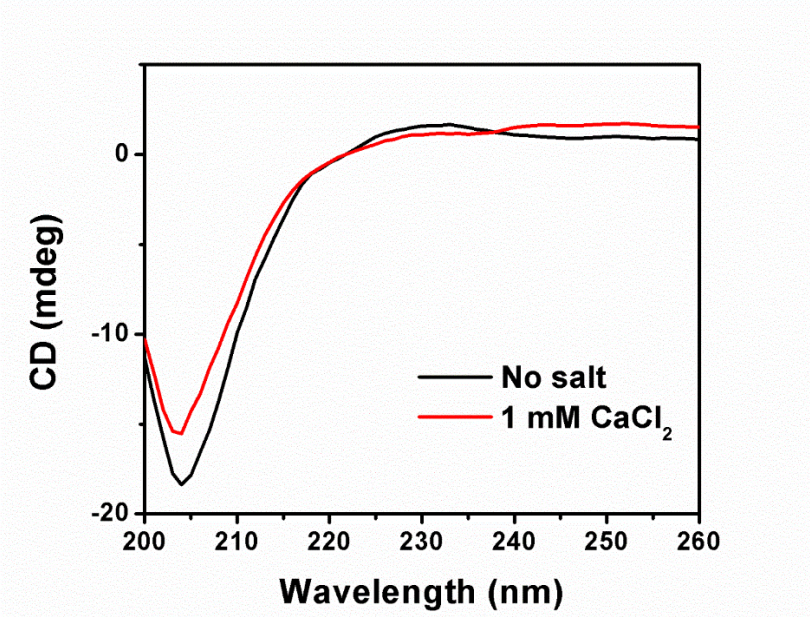

Figure S38. CD spectra of C_{14}-$(PEP_{Au}^{M\text{-}ox})_2$ in the presence and absence of 1 mM $CaCl_2$.

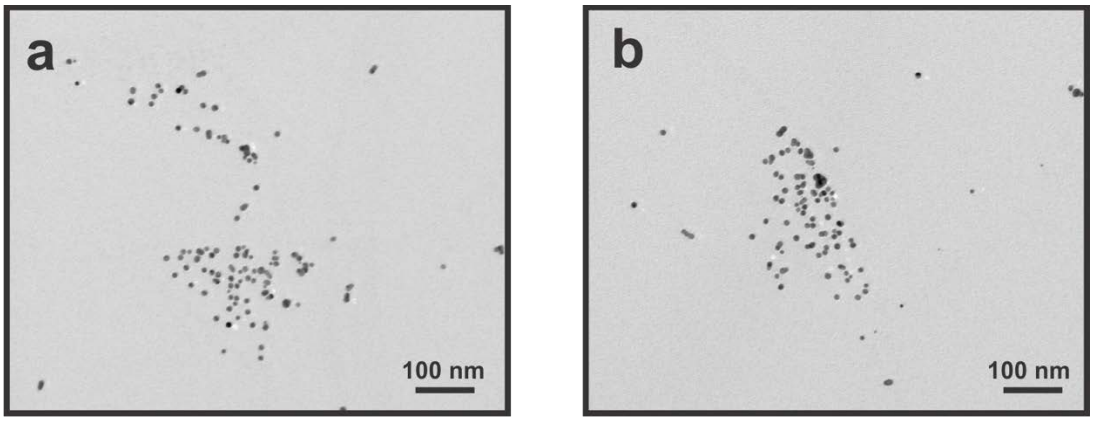

Figure S39. TEM analysis of C_{14}-$(PEP_{Au}^{M\text{-}ox})_2$-based unassembled AuNPs.

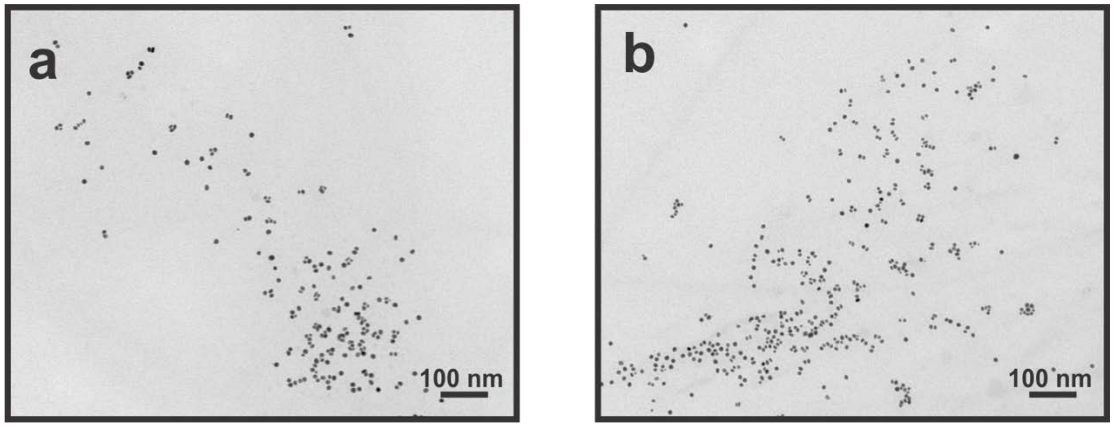

Figure S40. TEM analysis of C_{16}-$(PEP_{Au}^{M\text{-}ox})_2$-based unassembled AuNPs formed in the absence of $CaCl_2$.

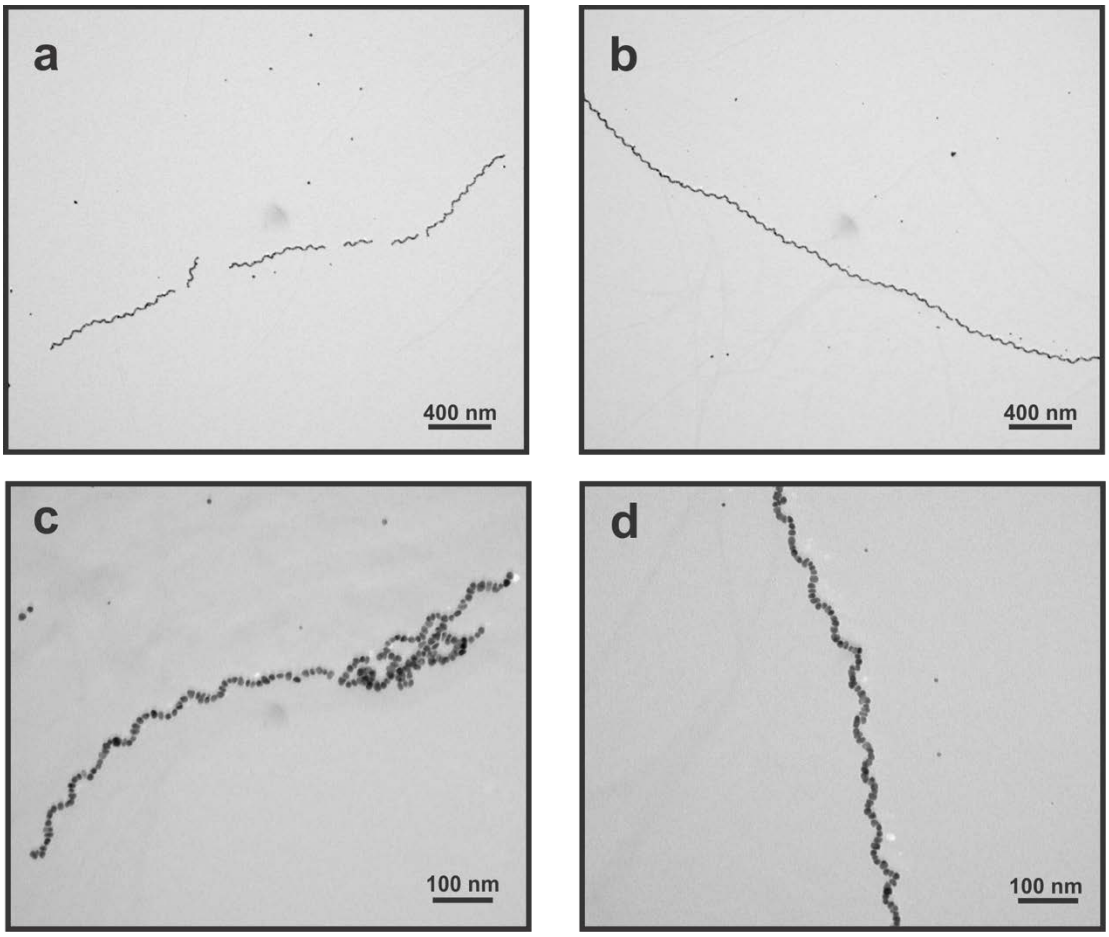

Figure S41. TEM analysis of C_{16}-$(PEP_{Au}{}^{M\text{-}ox})_2$-based single helices formed in the presence of 1 mM $CaCl_2$.

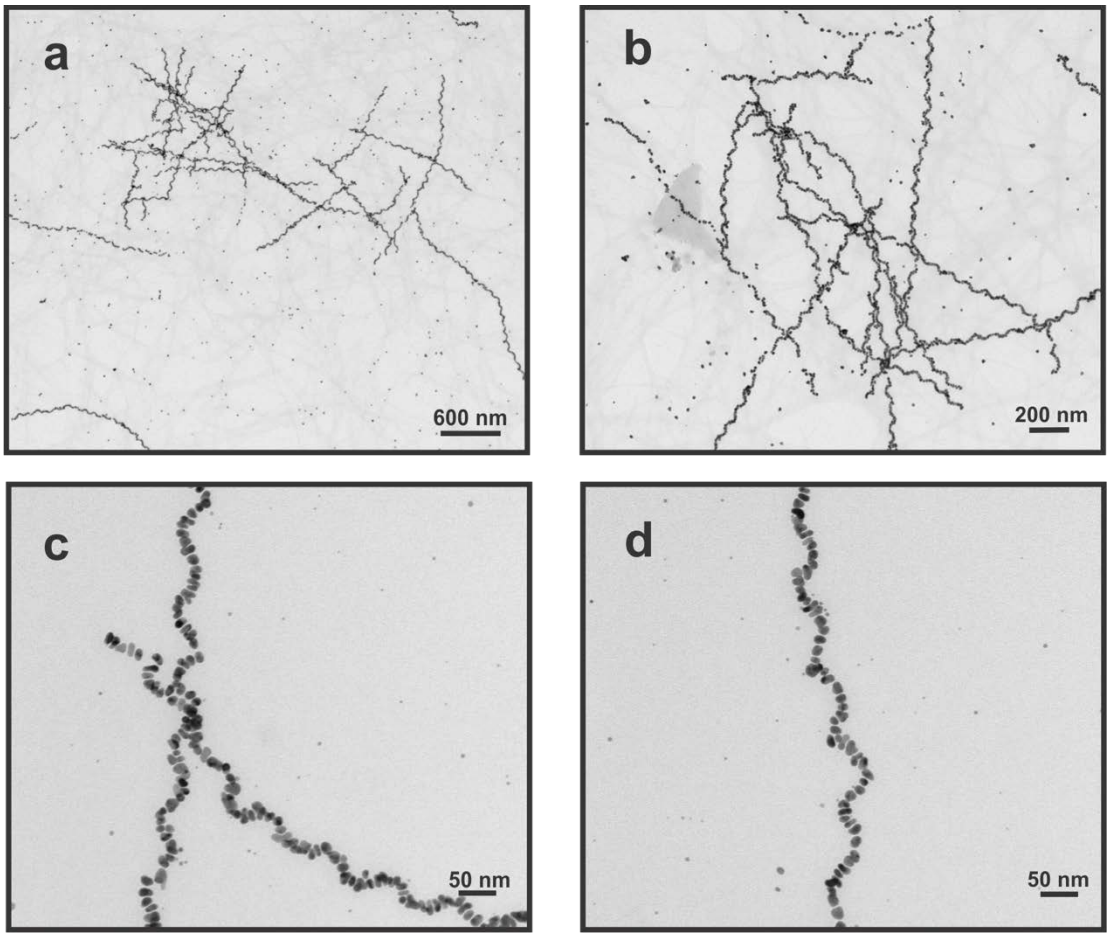

Figure S42. TEM analysis of C_{18}-$(PEP_{Au}{}^{M\text{-}ox})_2$-based single helices.

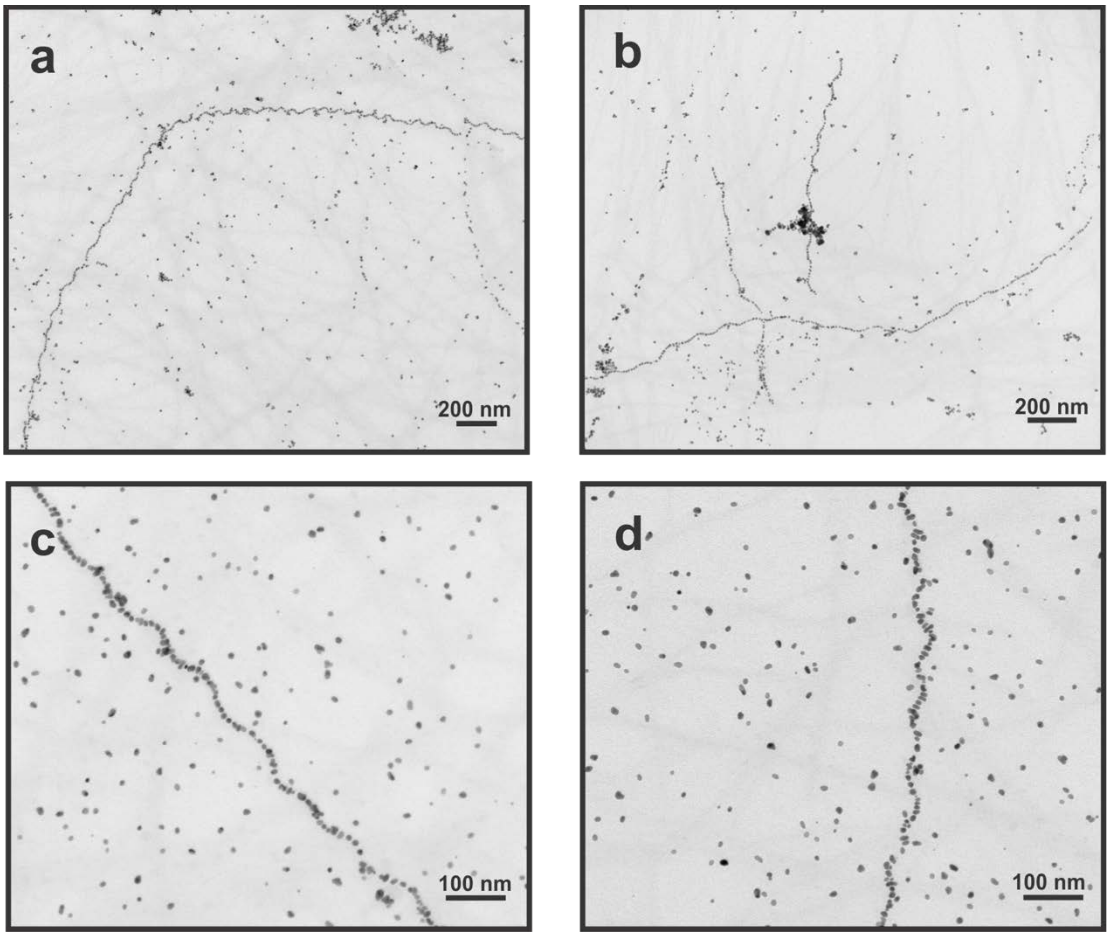

Figure S43. TEM analysis of C_{20}-$(PEP_{Au}{}^{M\text{-}ox})_2$-based single helices.

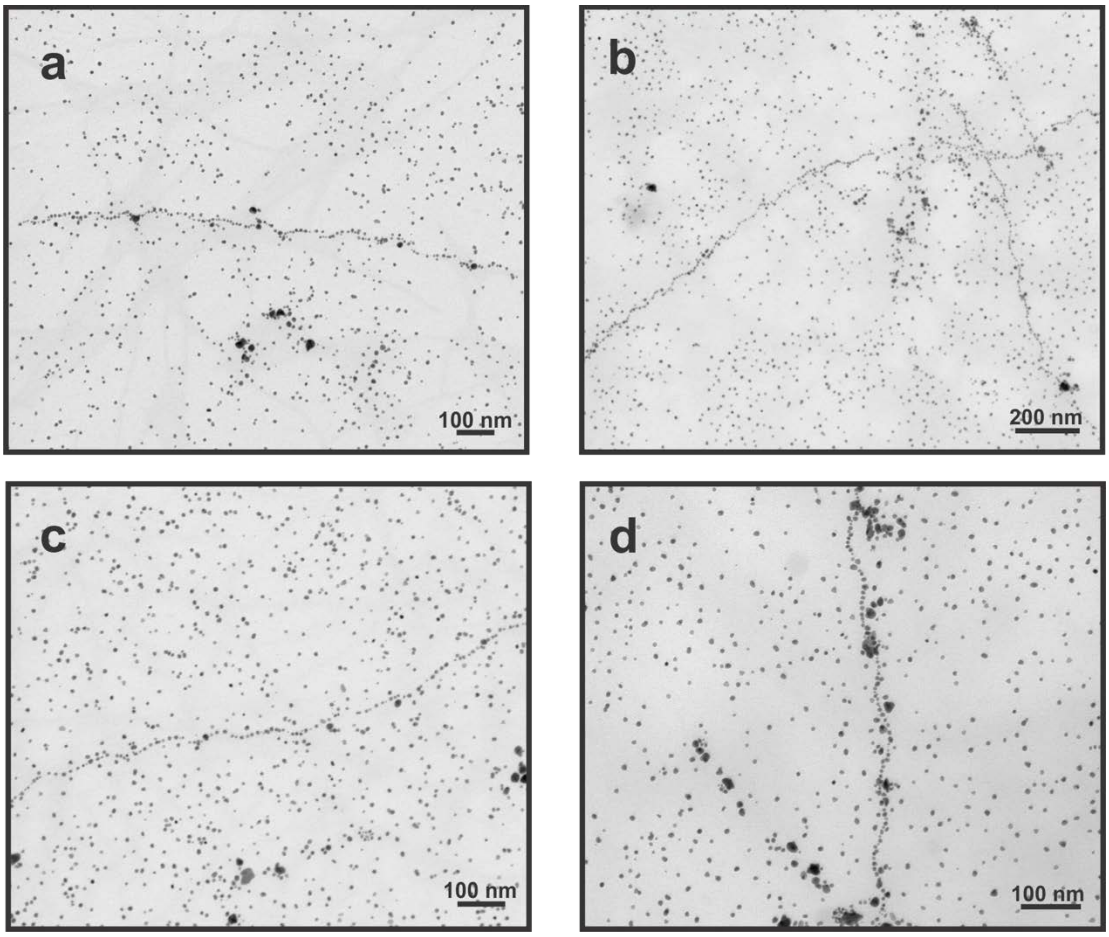

Figure S44. TEM analysis of C_{22}-$(PEP_{Au}^{M\text{-}ox})_2$-based single helices.

Table S4. NP dimensions as a function of salt concentration in C_{16}-$(PEP_{Au}^{M\text{-}ox})_2$-based assembly of single helices.

$CaCl_2$ concentration (mM)	NP length (nm)	NP width (nm)
1	13.4 ± 2.0	7.9 ± 1.8
5	15.0 ± 1.9	10.7 ± 1.7
20	12.1 ± 1.5	11.6 ± 1.4
40	11.6 ± 1.2	11.6 ± 1.4

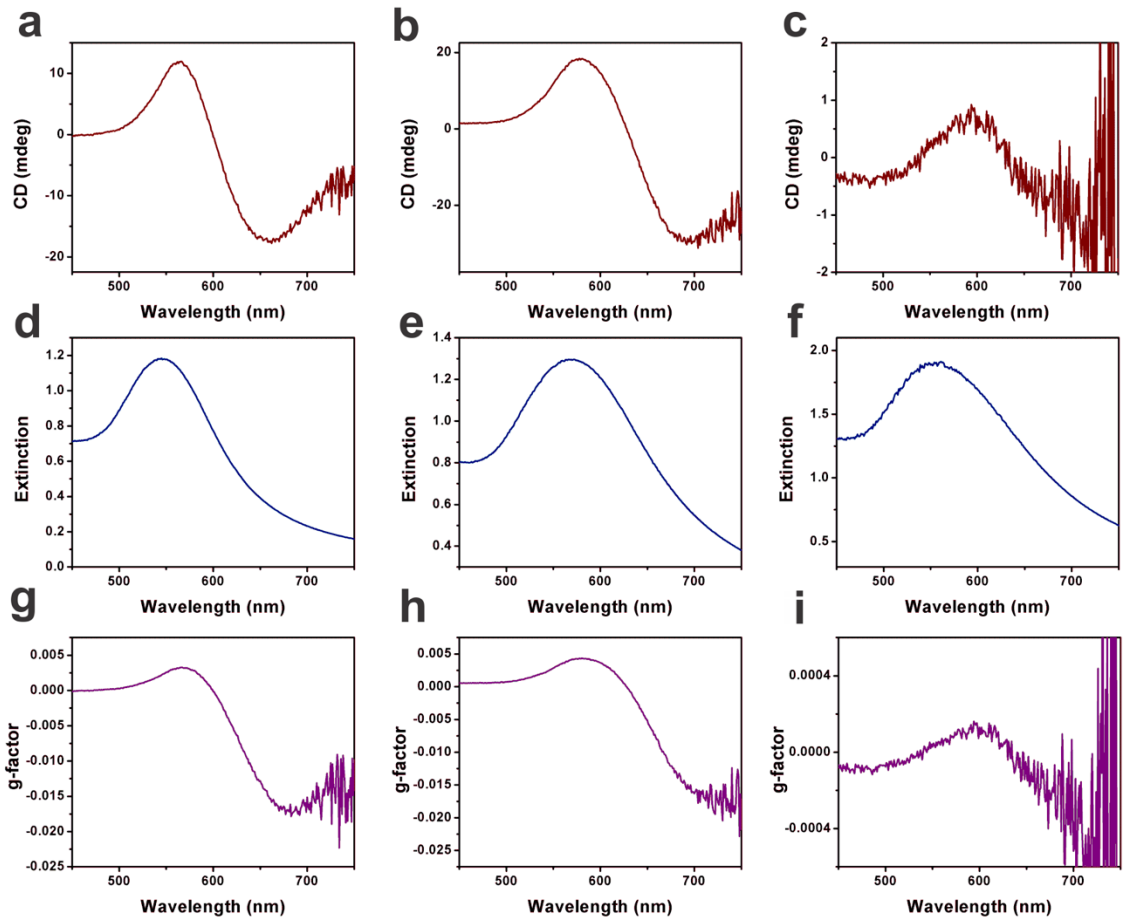

Figure S45. Chiroptical response monitored via CD for single helices derived from (a) C_{16}-$(PEP_{Au}^{M\text{-}ox})_2$, (b) C_{18}-$(PEP_{Au}^{M\text{-}ox})_2$ and (c) C_{20}-$(PEP_{Au}^{M\text{-}ox})_2$. UV-vis extinction for single helices derived from (d) C_{16}-$(PEP_{Au}^{M\text{-}ox})_2$, (e) C_{18}-$(PEP_{Au}^{M\text{-}ox})_2$ and (f) C_{20}-$(PEP_{Au}^{M\text{-}ox})_2$. *g*-factor plots of (g) C_{16}-$(PEP_{Au}^{M\text{-}ox})_2$, (h) C_{18}-$(PEP_{Au}^{M\text{-}ox})_2$ and (i) C_{20}-$(PEP_{Au}^{M\text{-}ox})_2$-based single helices. *g*-factor = $\Delta\varepsilon/\varepsilon$, where $\Delta\varepsilon$ is the circular dichroism and ε is the extinction.

Appendix B

Supporting Information for Chapter 3: “Beta-Sheet Modification Strategy for Affecting the Assembly Behavior of AuNPs”

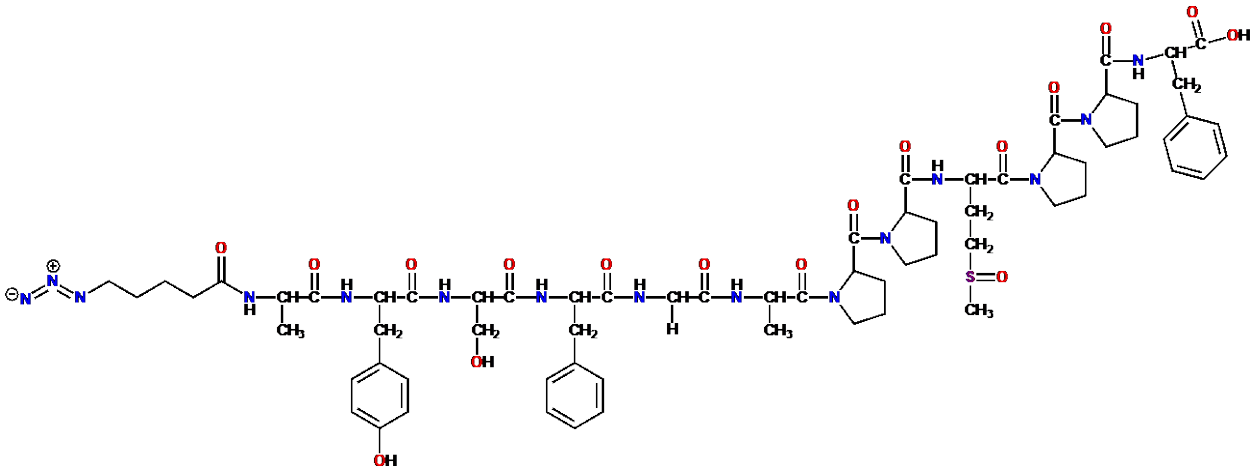

Figure S46. Chemical structure of N_3-(AYSFGAPPM^{ox}PPF).

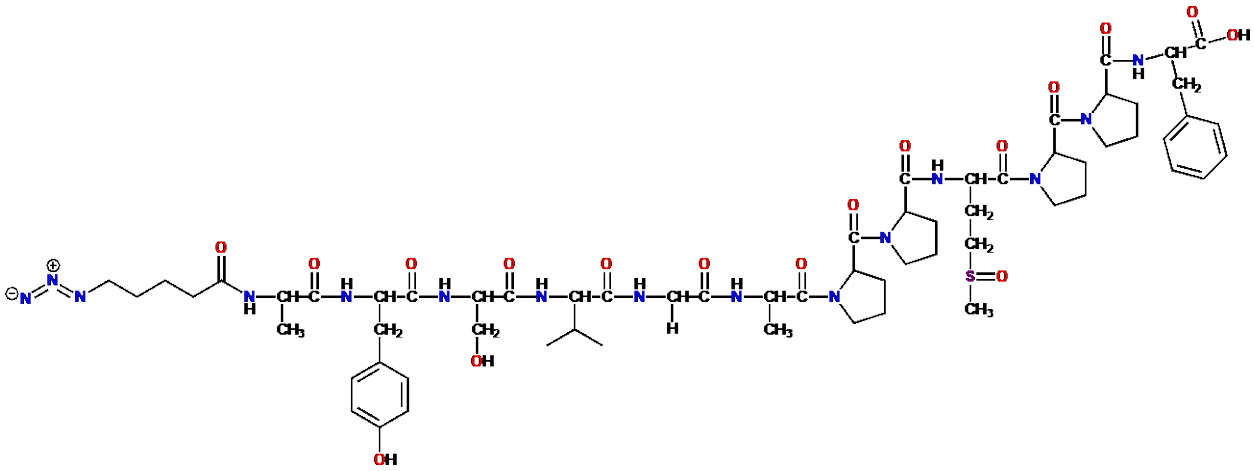

Figure S47. Chemical structure of N_3-(AYSVGAPPM^{ox}PPF).

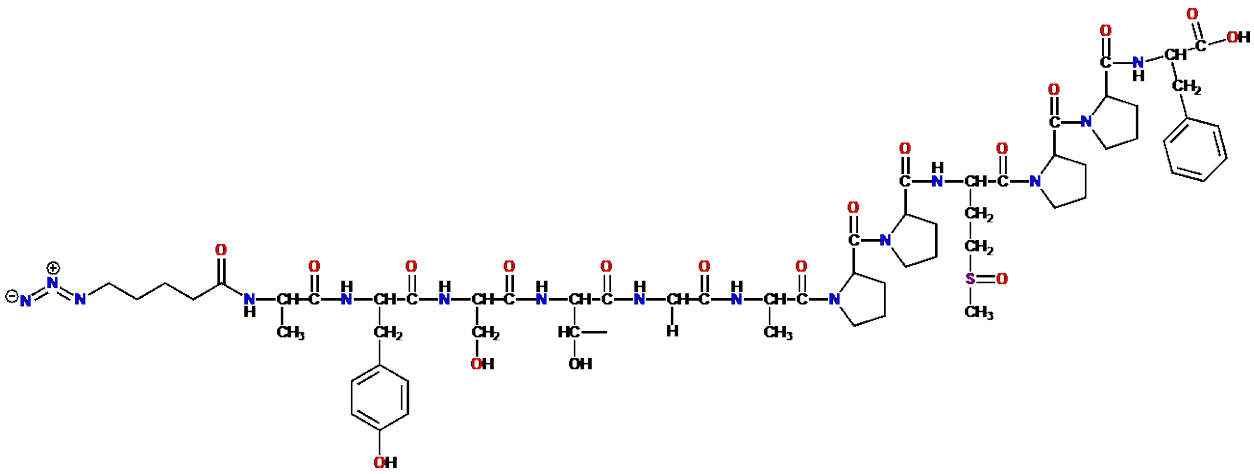

Figure S48. Chemical structure of N_3-(AYSTGAPPM^{ox}PPF).

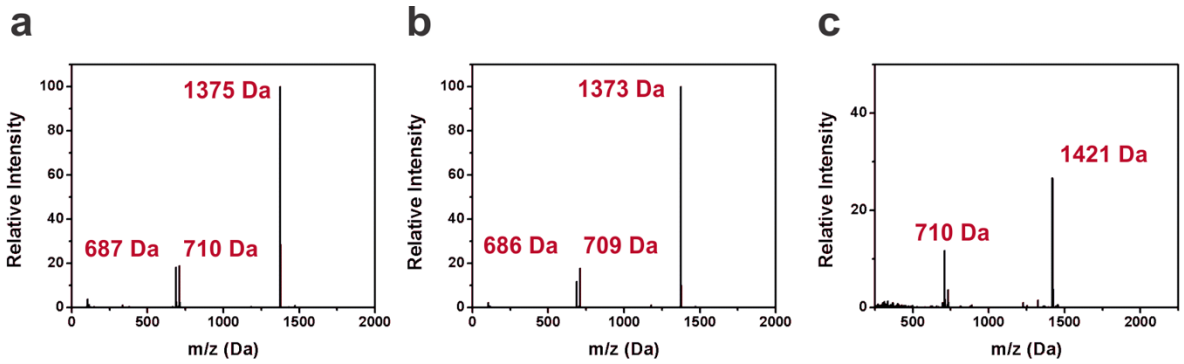

Figure S49. LC-MS mass assignment of (a) N_3-(AYSTGAPPM^{ox}PPF), m/z = 1375 Da (M-H$^+$); 710 Da (M-H$^+$+ HCOO$^-$)/2; 687 Da (M-2H$^+$)/2; (b) N_3-(AYSVGAPPM^{ox}PPF), m/z =1373 Da (M-H$^+$); 709 Da (M-H$^+$+ HCOO$^-$)/2; 686 Da (M-2H$^+$)/2; (c) N_3-(AYSFGAPPM^{ox}PPF), m/z = 1421 Da (M-H$^+$); 710 Da (M-2H$^+$)/2.

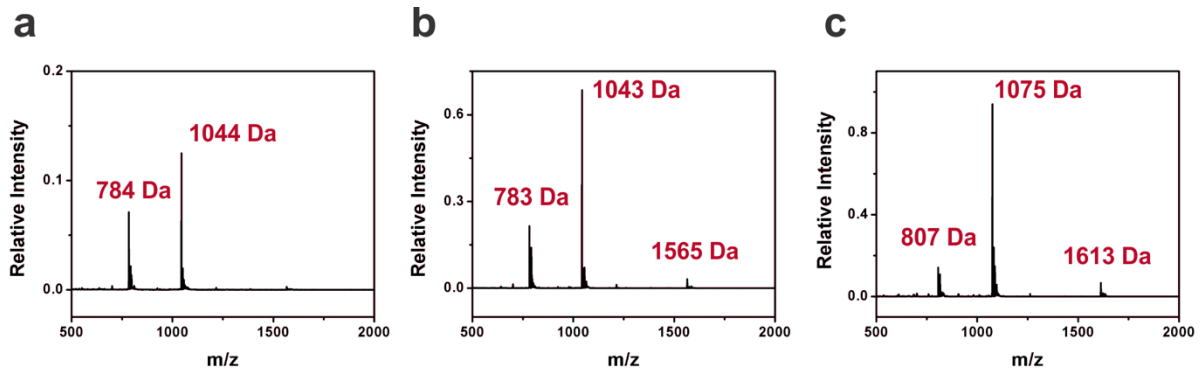

Figure S50. LC-MS mass assignment of (a) C_{14}-(AYSTGAPPM^{ox}PPF)$_2$, m/z = 1044 Da (M-3H$^+$)/3; 784 Da (M-4H$^+$)/4; (b) C_{14}-(AYSVGAPPM^{ox}PPF)$_2$, m/z =1565 Da (M-2H$^+$)/2; 1043 Da (M- 3H$^+$)/3, 783 Da (M-4H$^+$)/4; (c) C_{14}-(AYSFGAPPM^{ox}PPF)$_2$, m/z = 1613 Da (M-2H$^+$)/2; 1075 Da (M-3H$^+$)/3; 807 Da (M-4H$^+$)/4.

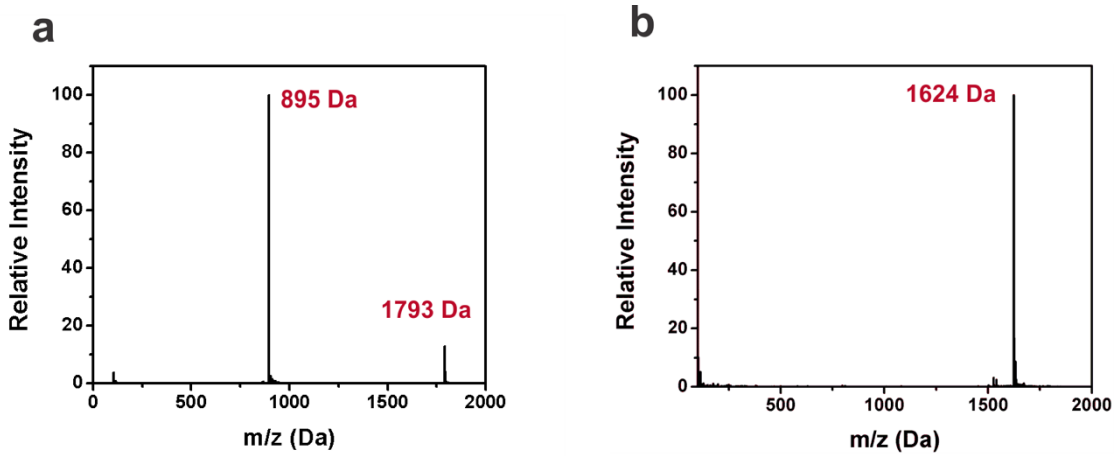

Figure S51. LC-MS mass assignment of (a) C_{18}-(AYSSGA)$_2$, m/z = 1793 Da (M-H$^+$); 895 Da (M-2H$^+$)/2; and (b) C_{16}-(AYSFGAPPM^{ox}PPF)$_2$, m/z =1624 Da (M-2H$^+$)/2.

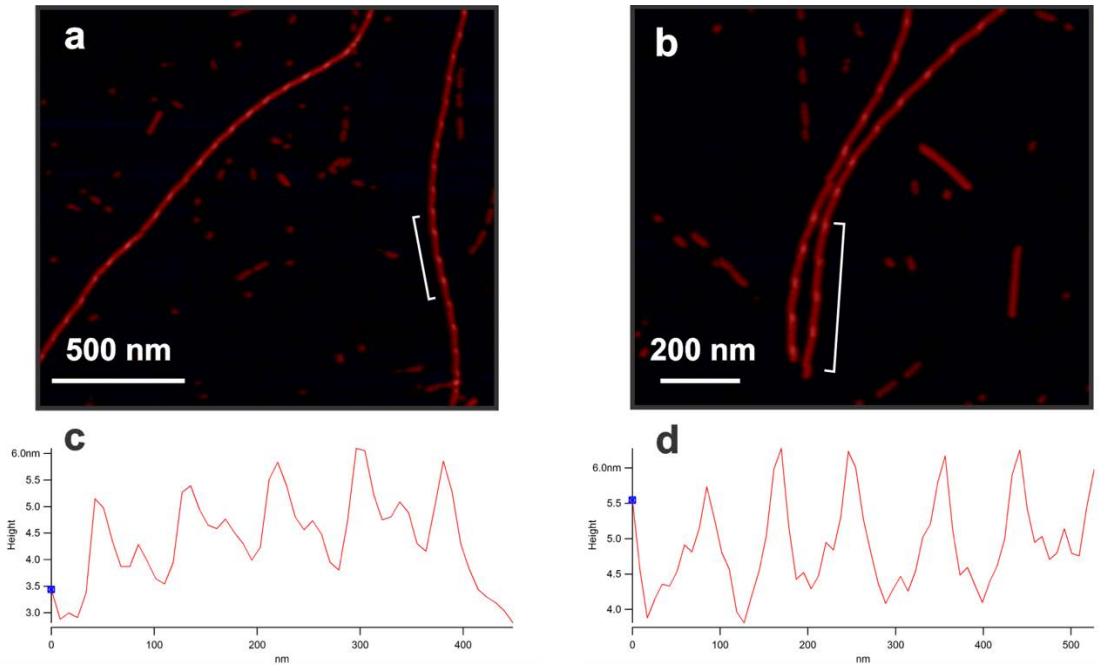

Figure S52. Additional AFM images of (a, b) C_{14}-(AYSVGAPPM^{ox}PPF)$_2$, with labeled segments corresponding to (c, d) height traces.

.

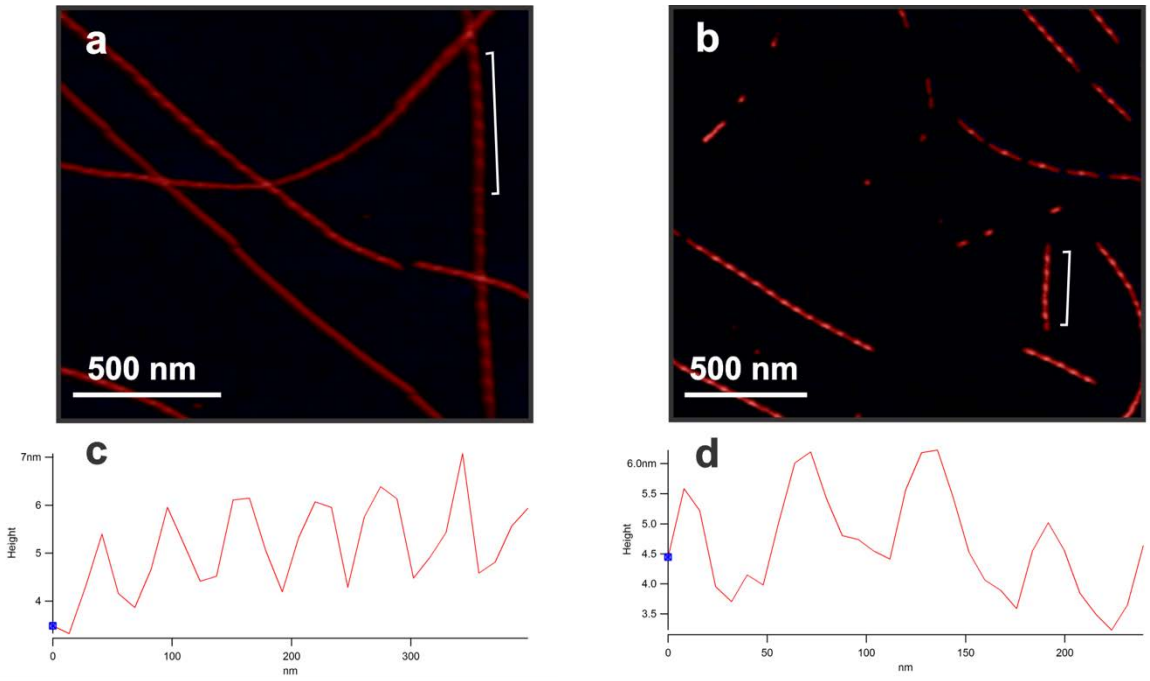

Figure S53. Additional AFM images of (a, b) C_{14}-(AYSFGAPPM^{ox}PPF)$_2$, with labeled segments corresponding to (c, d) height traces.

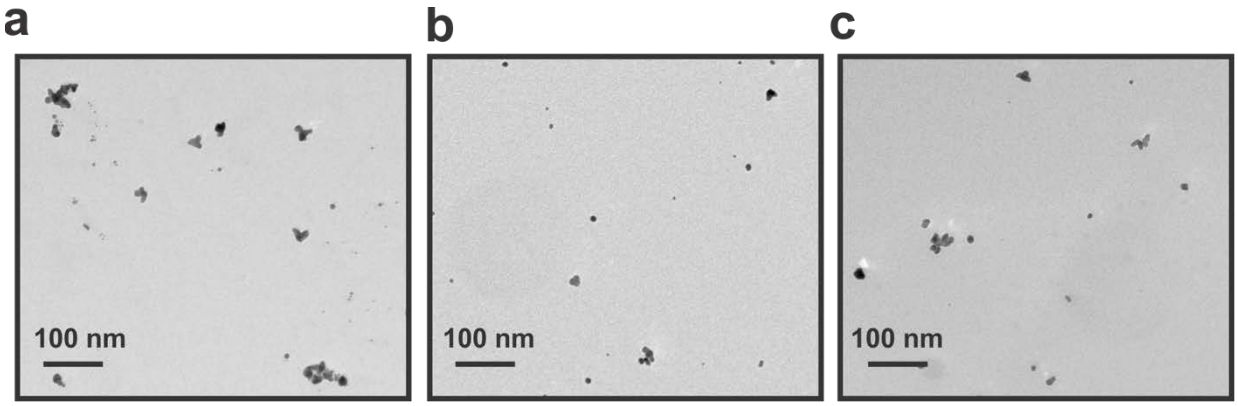

Figure S54. Control experiments performed to confirm that mutant peptide sequences bind to gold and direct the synthesis of discrete NPs. TEM images indicate the formation of unassembled AuNPs in the presence of (a) N_3-(AYSTGAPPM^{ox}PPF)$_2$, (b) N_3-(AYSVGAPPM^{ox}PPF)$_2$, and (c) N_3-(AYSFGAPPM^{ox}PPF)$_2$.

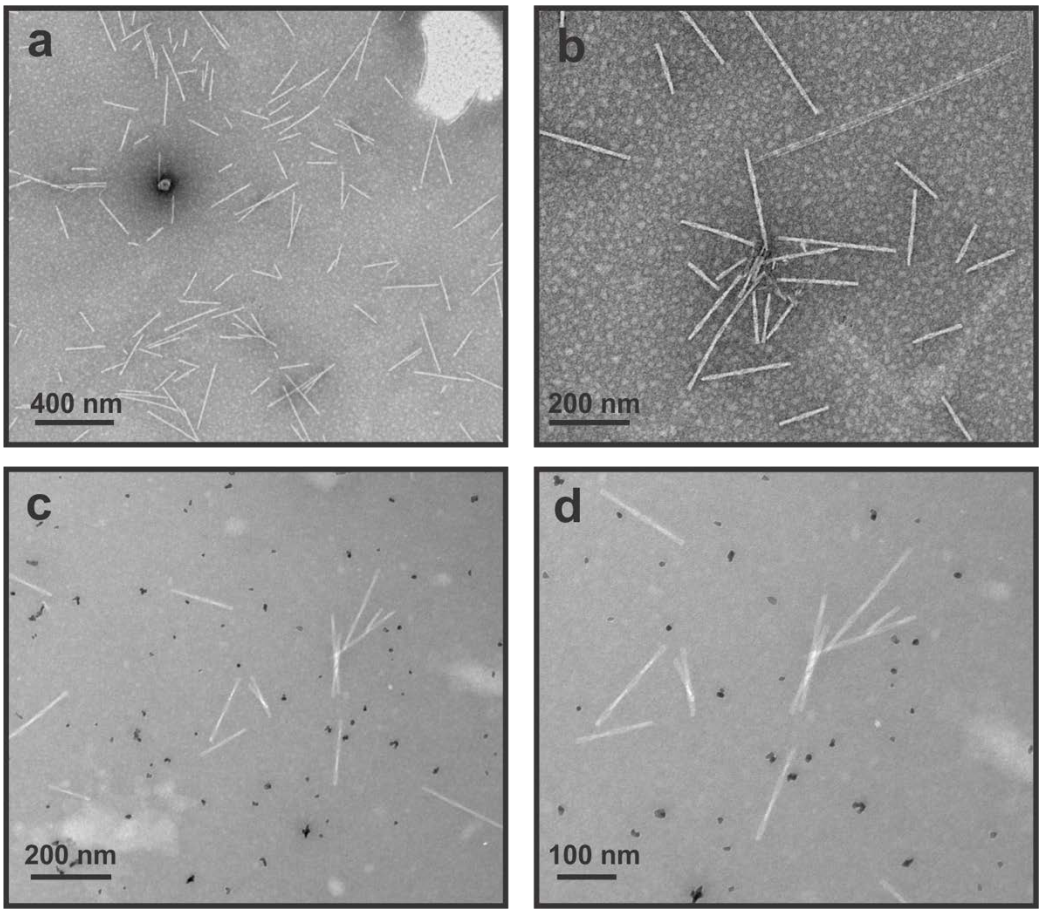

Figure S55. Control experiments performed using C_{18}-$(AYSSGA)_2$ which does not contain -PPM^{ox}PPF gold-binding segment. (a, b) TEM images of C_{18}-$(AYSSGA)_2$ fibers self-assembled in 0.1 M HEPES buffer. (c, d) TEM images indicate that in the presence of 0.1 M HEPES and $HAuCl_4$/TEAA, C_{18}-$(AYSSGA)_2$ self assembles into fibers but does not form any AuNP superstructures.

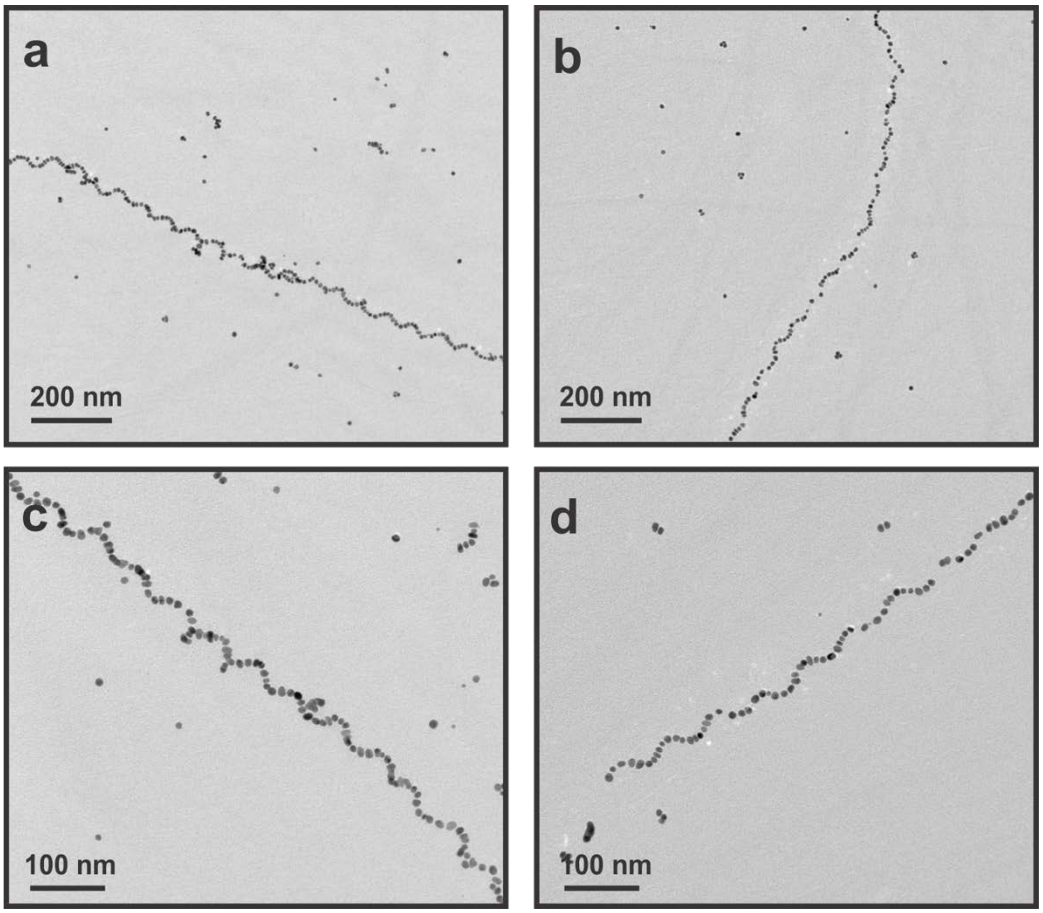

Figure S56. TEM images of C_{14}-(AYSFGAPPM^{ox}PPF)$_2$-directed assembly of single helices.

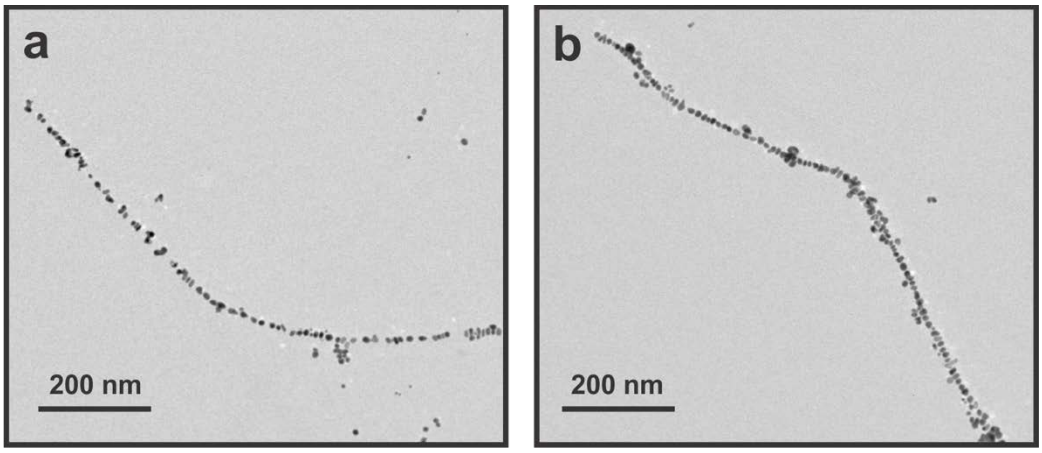

Figure S57. TEM images of AuNP 1D chains observed as a side product in the C_{14}-(AYSFGAPPM^{ox}PPF)$_2$-directed assembly of single helices.

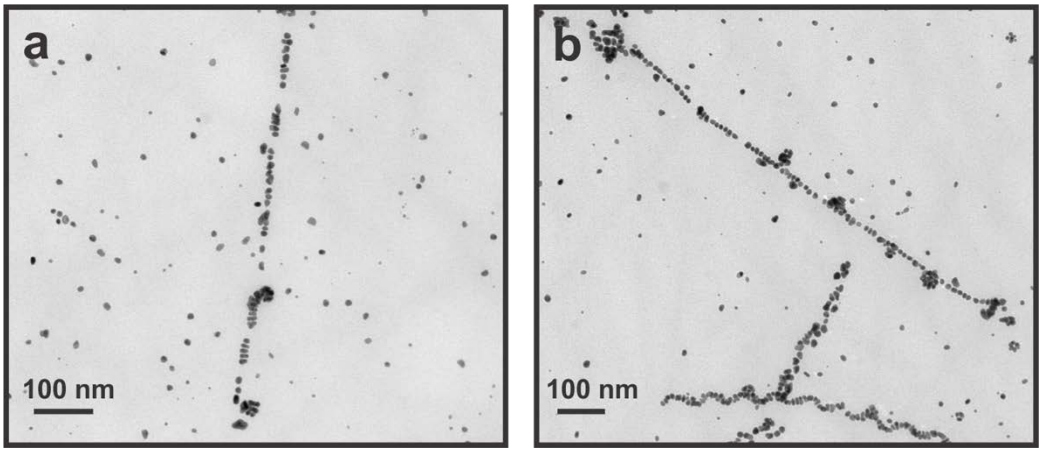

Figure S58. TEM images of AuNP 1D chains observed as a side product in the C_{16}-(AYSFGAPPM^{ox}PPF)$_2$-directed assembly of single helices.

Appendix C

Supporting Information for Chapter 4: "Effect of C-Terminus Peptide Modification on the Structure and Chiroptical Properties of Helical AuNP Assemblies"

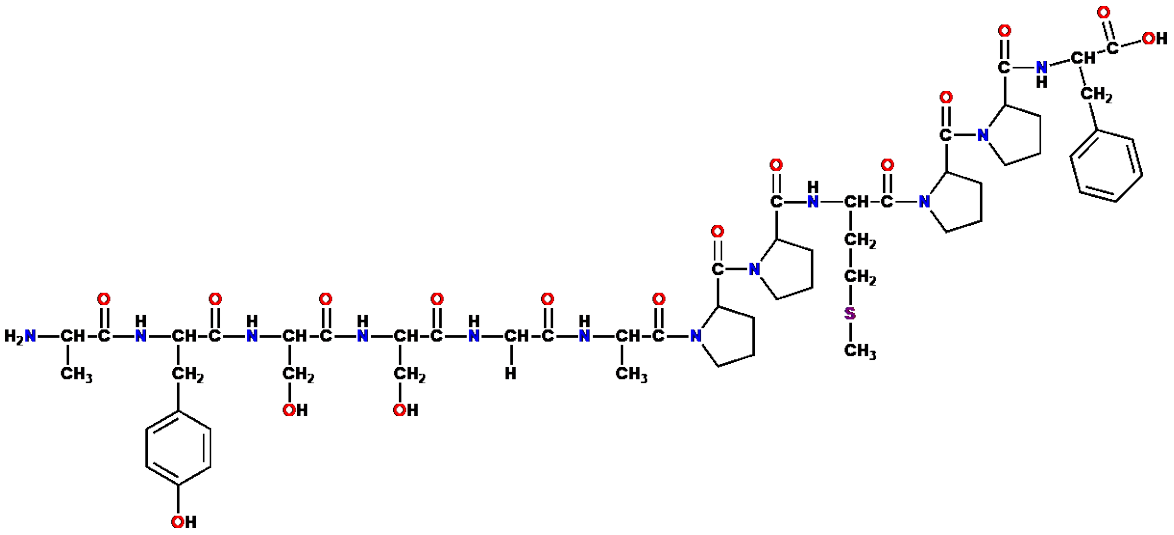

Figure S59. Molecular structure of $PEP_{Au}^{M, 9}$.

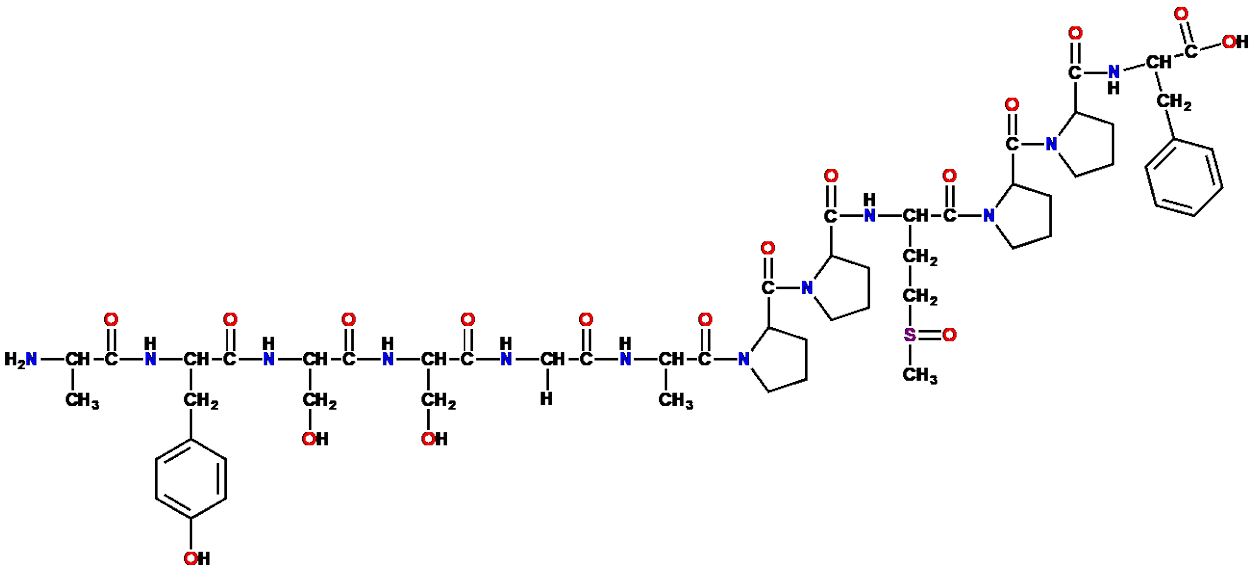

Figure S60. Molecular structure of $PEP_{Au}^{M\text{-}ox, 9}$.

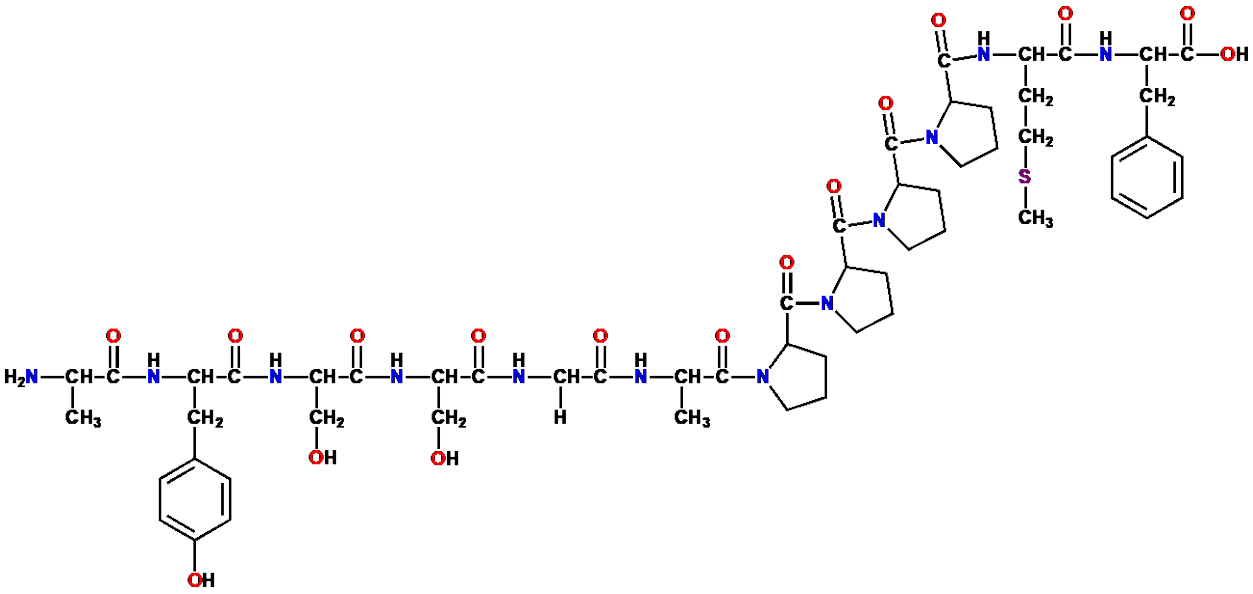

Figure S61. Molecular structure of $PEP_{Au}^{M, 11}$.

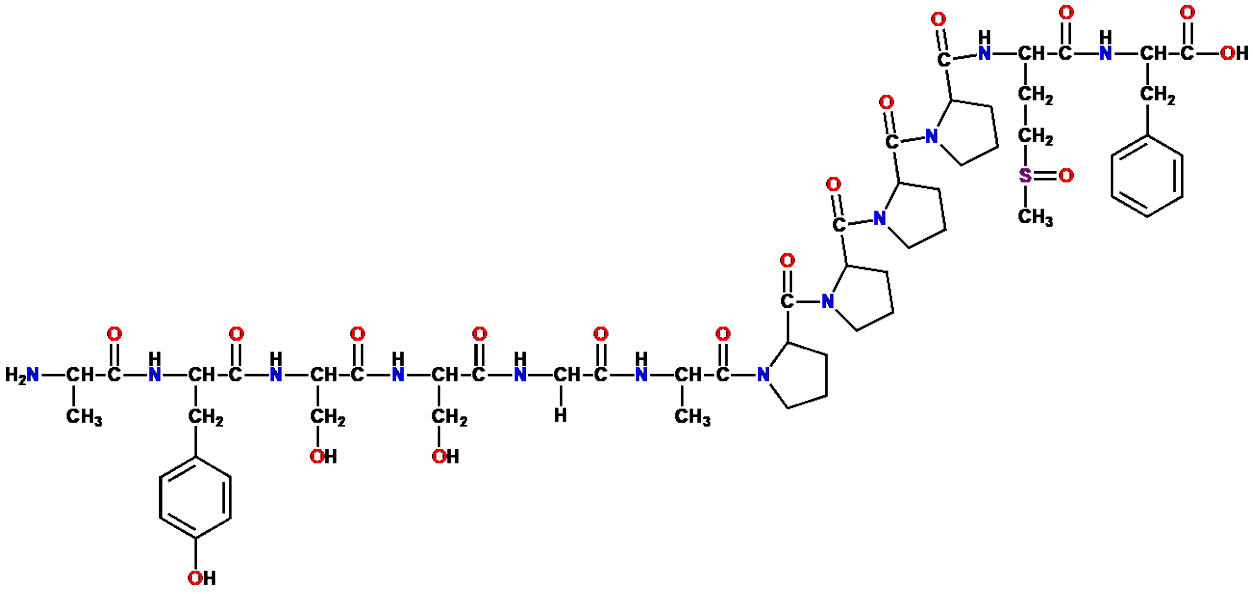

Figure S62. Molecular structure of $PEP_{Au}^{M\text{-}ox, 11}$.

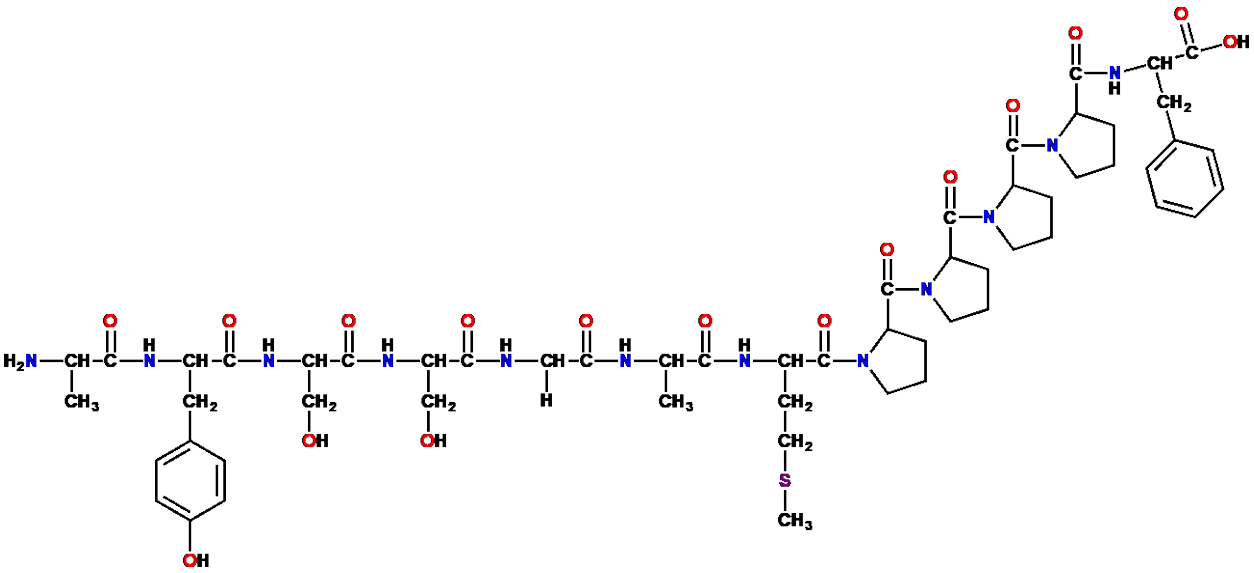

Figure S63. Molecular structure of $PEP_{Au}^{M, 7}$.

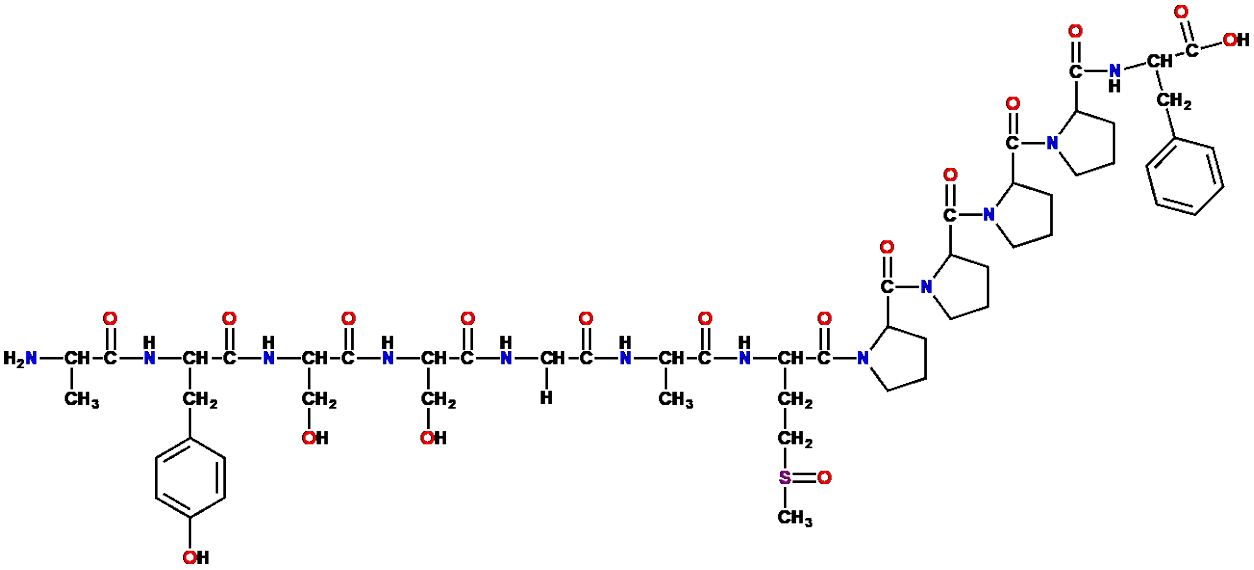

Figure S64. Molecular structure of $PEP_{Au}^{M\text{-}ox, 7}$.

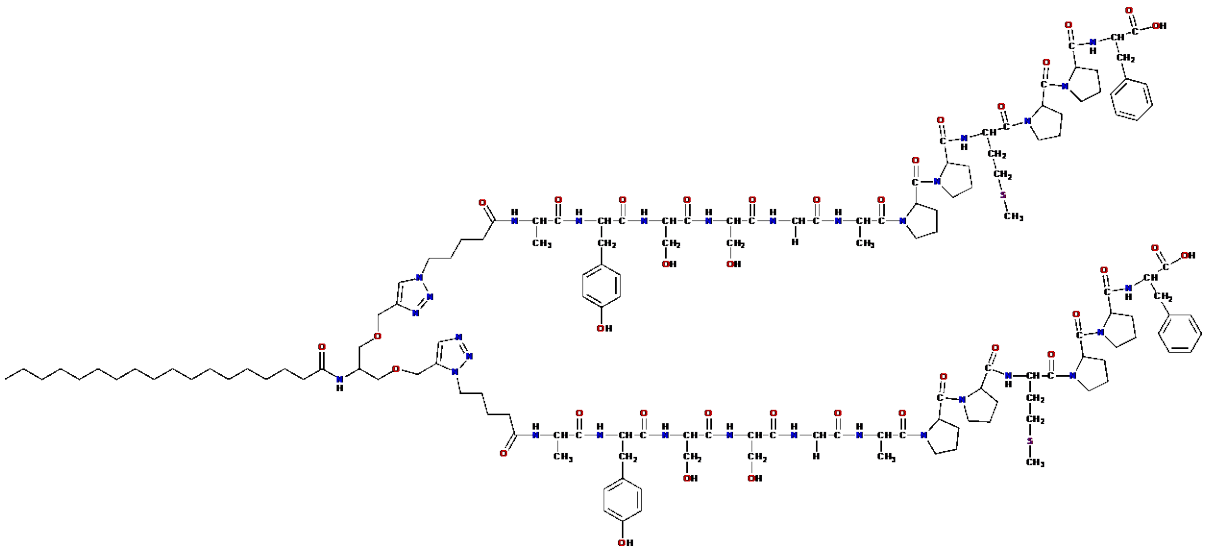

Figure S65. Molecular structure of C_{18}-$(PEP_{Au}^{M,\,9})_2$.

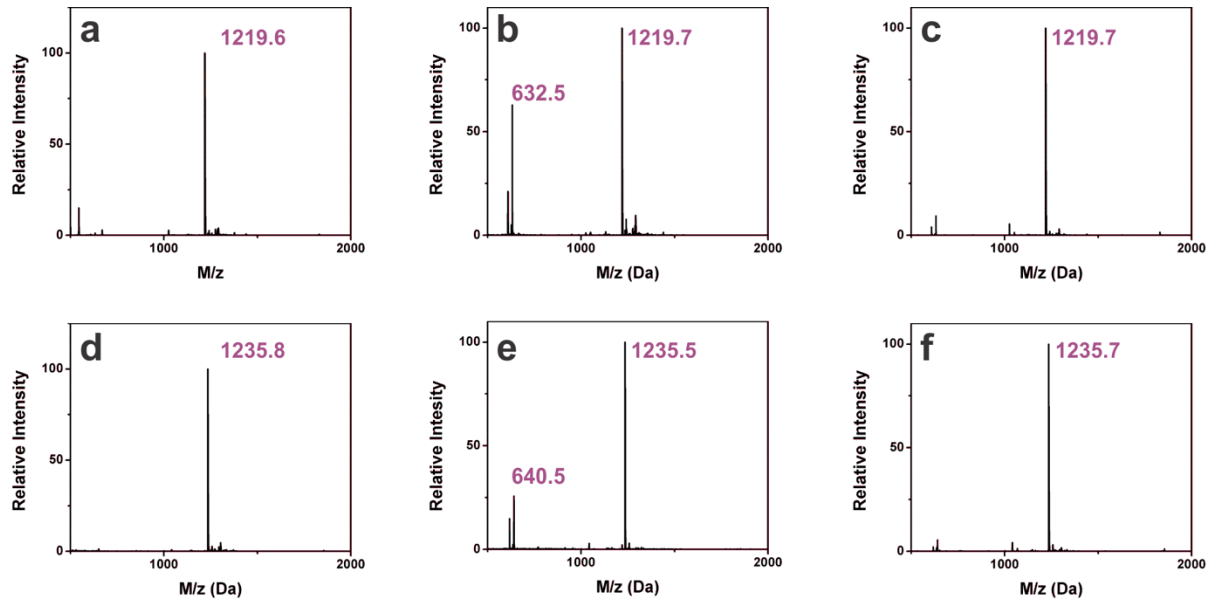

Figure S66. LC-MS assignment of (a) $PEP_{Au}^{M,\ 7}$ = 1219.6 Da ($M\text{-}H^+$); (b) $PEP_{Au}^{M,\ 9}$ = 1219.6 Da ($M\text{-}H^+$), 632.5 ($M\text{-}2H^+$)/2; (c) $PEP_{Au}^{M,\ 11}$ = 1219.7 Da ($M\text{-}H^+$); (d) $PEP_{Au}^{M\text{-}ox,\ 7}$ = 1235.8 Da ($M\text{-}H^+$); (e) $PEP_{Au}^{M\text{-}ox,\ 9}$ = 1235.5 Da ($M\text{-}H^+$), 640.5 Da ($M\text{-}2H^+$)/2; (f) $PEP_{Au}^{M\text{-}ox,\ 11}$ = 1235.7 Da ($M\text{-}H^+$).

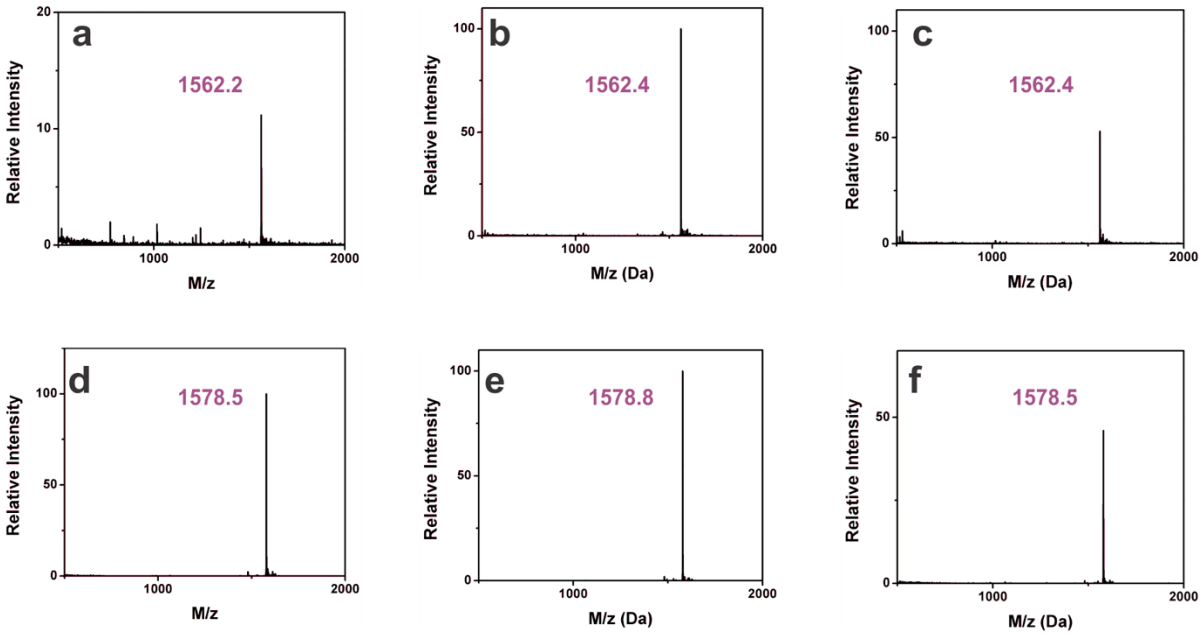

Figure S67. LC-MS assignment of (a) C_{18}-$(PEP_{Au}{}^{M,\,7})_2$ = 1562.2 Da $(M\text{-}2H^+)/2$; (b) C_{18}-$(PEP_{Au}{}^{M,\,9})_2$ = 1562.4 Da $(M\text{-}2H^+)/2$; (c) C_{18}-$(PEP_{Au}{}^{M,\,11})_2$ = 1219.7 Da $(M\text{-}2H^+)/2$; (d) C_{18}-$(PEP_{Au}{}^{M\text{-}ox,\,7})_2$ = 1578.5 Da $(M\text{-}2H^+)/2$; (e) C_{18}-$(PEP_{Au}{}^{M\text{-}ox,\,9})_2$ = 1578.8 Da $(M\text{-}2H^+)/2$; (f) C_{18}-$(PEP_{Au}{}^{M\text{-}ox,\,11})_2$= 1578.5 Da $(M\text{-}2H^+)/2$.

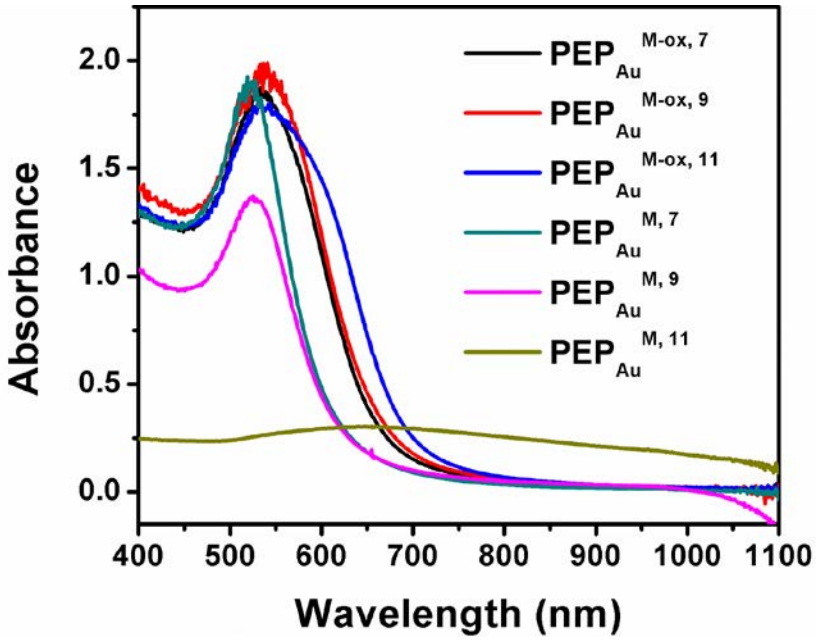

Figure S68. UV-vis absorption spectra of AuNPs synthesized in the presence of methionine-based mutant peptides. Slight shifts in peak maxima and peak broadening observed in the case of peptides containing M-ox.

Table S5. Conformational ensemble population distribution for the top ten most populated distinct structures (clusters) of $PEP_{Au}^{M,9}$ (AYSSGAPPMPPF) in the unadsorbed state.

Cluster Rank	Percentage Population
1	22
2	7
3	6
4	5
5	4
6	3
7	3
8	2
9	2
10	2

Table S6. Conformational ensemble population distribution for the top ten most populated distinct structures (clusters) of $PEP_{Au}^{M,7}$ (AYSSGAMPPPPF) in the unadsorbed state.

Cluster Rank	Percentage Population
1	10
2	8
3	8
4	7
5	5
6	4
7	4
8	3
9	3
10	3

Table S7. Conformational ensemble population distribution for the top ten most populated distinct structures (clusters) of $PEP_{Au}^{M, 11}$ (AYSSGAPPPPMF) in the unadsorbed state.

Cluster Rank	Percentage Population
1	12
2	10
3	8
4	6
5	6
6	6
7	6
8	5
9	4
10	3

Table S8. Conformational ensemble population distribution for the top ten most populated distinct structures (clusters) of $PEP_{Au}^{M\text{-}ox,\ 9}$ (AYSSGAPPM^{ox}PPF) in the unadsorbed state.

Cluster Rank	Percentage Population
1	17
2	7
3	5
4	4
5	4
6	3
7	3
8	3
9	2
10	2

Table S9. Conformational ensemble population distribution for the top ten most populated distinct structures (clusters) of $PEP_{Au}^{M\text{-}ox,\ 7}$ (AYSSGAM^{ox}PPPPF) in the unadsorbed state.

Cluster Rank	Percentage Population
1	24
2	8
3	7
4	4
5	4
6	4
7	4
8	3
9	2
10	2

Table S10. Conformational ensemble population distribution for the top ten most populated distinct structures (clusters) of $PEP_{Au}^{M\text{-}ox,\ 11}$ (AYSSGAPPPPM^{ox}F) in the unadsorbed state.

Cluster Rank	Percentage Population
1	22
2	9
3	8
4	7
5	5
6	5
7	4
8	4
9	3
10	3

Table S11. Cross-cluster similarity analysis. The top five most populated clusters for $PEP_{Au}^{M, 9}$ are compared with all clusters generated for $PEP_{Au}^{M\text{-}ox, 9}$, based on the root mean squared deviation (RMSD) of the backbone atom positions, within a cutoff of 0.2 nm (the same as was used for the clustering analysis). Entries in black designate a cluster match, entries in red signify a near match (with an RMSD within a cutoff of 0.25 nm).

Cluster rank of $PEP_{Au}^{M, 9}$	Cluster rank of $PEP_{Au}^{M\text{-}ox, 9}$
0	1, 5
1	1, 3, 9
2	5
3	-
4	2

Table S12. Cross-cluster similarity analysis. The top five most populated clusters for $PEP_{Au}^{M, 7}$ are compared with all clusters generated for $PEP_{Au}^{M\text{-}ox, 7}$, based on the root mean squared deviation (RMSD) of the backbone atom positions, within a cutoff of 0.2 nm (the same as was used for the clustering analysis). Entries in black designate a cluster match, entries in red signify a near match (with an RMSD within a cutoff of 0.25 nm).

Cluster rank of $PEP_{Au}^{M, 7}$	Cluster rank of $PEP_{Au}^{M\text{-}ox, 7}$
0	3, 4
1	1, 6
2	2, 5
3	3, 8
4	2, 5

Table S13. Cross-cluster similarity analysis. The top five most populated clusters for $PEP_{Au}^{M, 11}$ are compared with all clusters generated for $PEP_{Au}^{M\text{-}ox, 11}$, based on the root mean squared deviation (RMSD) of the backbone atom positions, within a cutoff of 0.2 nm (the same as was used for the clustering analysis). Entries in black designate a cluster match, entries in red signify a near match (with an RMSD within a cutoff of 0.25 nm).

Cluster rank of $PEP_{Au}^{M, 11}$	Cluster rank of $PEP_{Au}^{M\text{-}ox, 11}$
0	0
1	-
2	8
3	0, 2
4	4

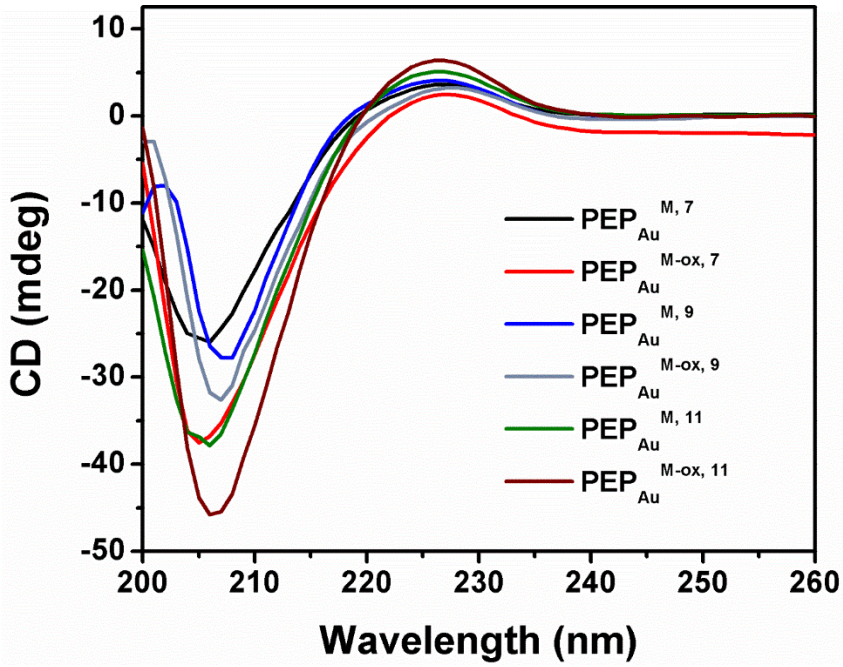

Figure S69. CD spectra of methionine-based mutant peptides dissolved in 10 mM HEPES buffer. All peptides exhibit a characteristic PPII signature.

Table S14. Percentage occupation of the principal regions of secondary structure in a Ramachandran plot, calculated over all frames of the REST MD simulation trajectories for each peptide in the unadsorbed state. Unclassified states are designated as random coil (RC).

Peptide	α	α	β	γ	γ	PPII	RC
$PEP_{Au}^{M, 7}$	22	1	14	2	1	55	5
$PEP_{Au}^{M, 9}$	22	1	13	1	1	58	4
$PEP_{Au}^{M, 11}$	9	11	6	2	1	33	37
$PEP_{Au}^{M\text{-}ox, 7}$	28	3	13	2	1	48	5
$PEP_{Au}^{M\text{-}ox, 9}$	28	1	14	2	1	52	4
$PEP_{Au}^{M\text{-}ox, 11}$	6	13	5	4	1	27	44

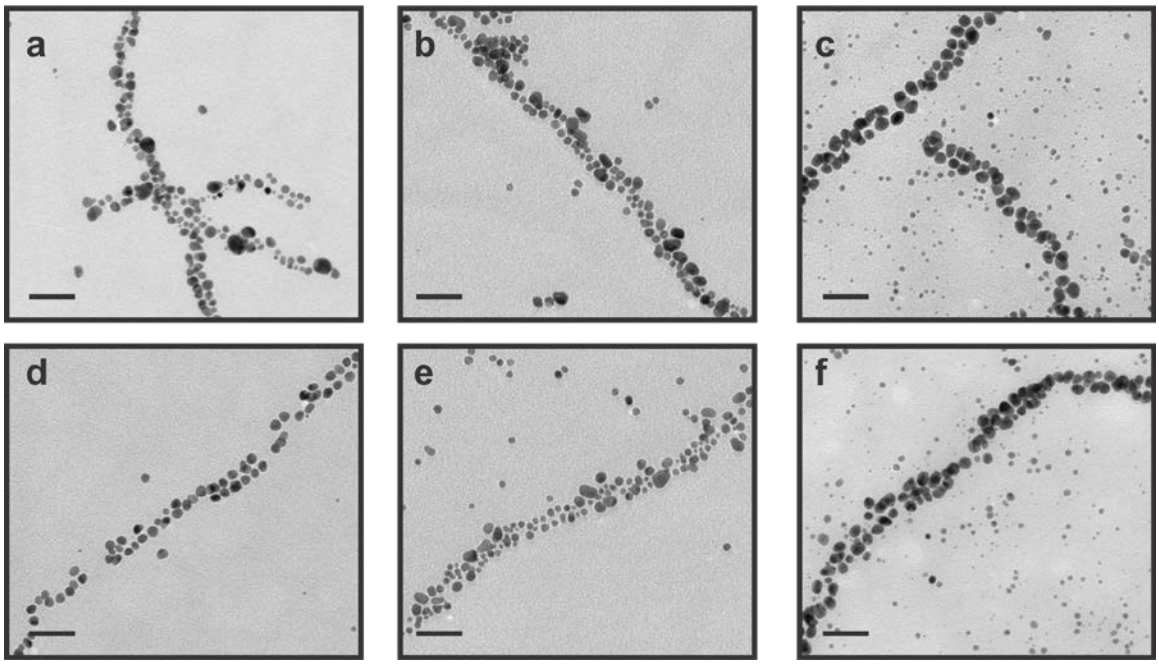

Figure S70. TEM images of irregular helical AuNP superstructures derived from (a, d) C_{18}-$(PEP_{Au}^{M,\ 7})_2$, (b, e) C_{18}-$(PEP_{Au}^{M,\ 9})_2$, (c, f) C_{18}-$(PEP_{Au}^{M,\ 11})_2$. Scale bar: 50 nm.

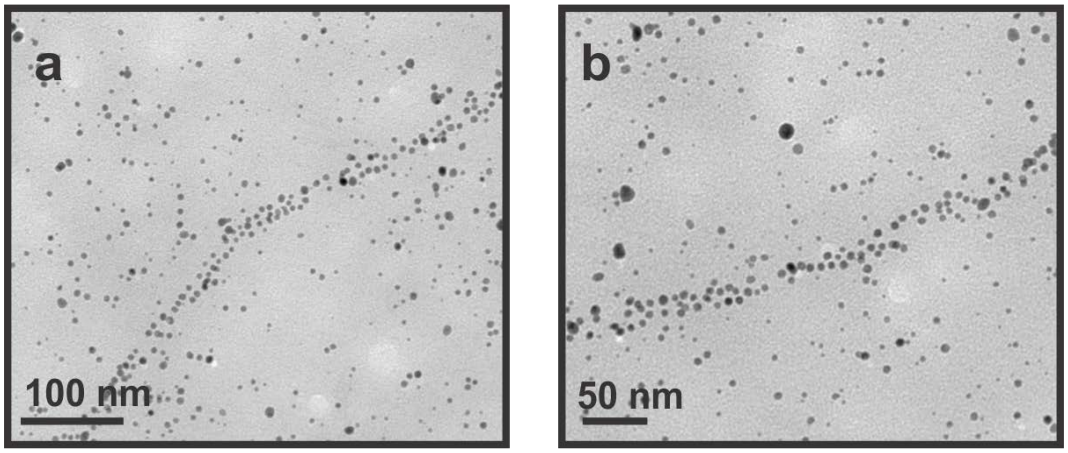

Figure S71. TEM analysis of irregular helical AuNP superstructures derived from C_{18}-$(PEP_{Au}^{M,\ 11})_2$. These structures represent a minor product.

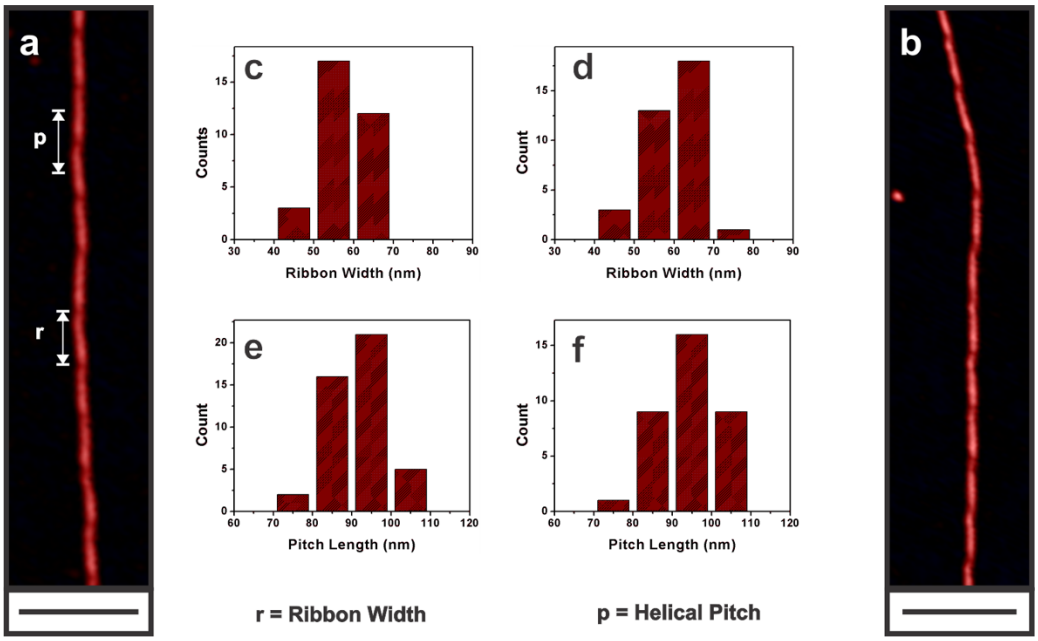

Figure S72. AFM analysis of helical ribbon fibers formed by (a) C_{18}-$(PEP_{Au}^{M\text{-}ox,\ 7})_2$ and (b) C_{18}-$(PEP_{Au}^{M\text{-}ox,\ 11})_2$. (c, d) Ribbon width distribution of helical ribbons derived from C_{18}-$(PEP_{Au}^{M\text{-}ox,\ 7})_2$ and C_{18}-$(PEP_{Au}^{M\text{-}ox,\ 11})_2$, respectively. (e, f) Pitch distribution of helical ribbons derived from C_{18}-$(PEP_{Au}^{M\text{-}ox,\ 7})_2$ and C_{18}-$(PEP_{Au}^{M\text{-}ox,\ 11})_2$, respectively. Scale bar: 200 nm.

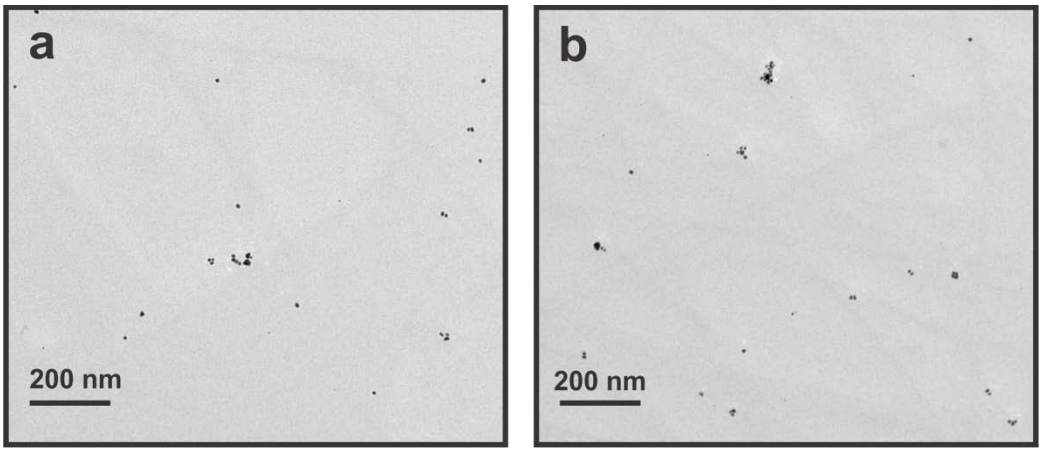

Figure S73. TEM images of unassembled AuNPs formed in the C_{18}-$(PEP_{Au}^{M\text{-}ox,\ 7})_2$-based superstructure synthesis.

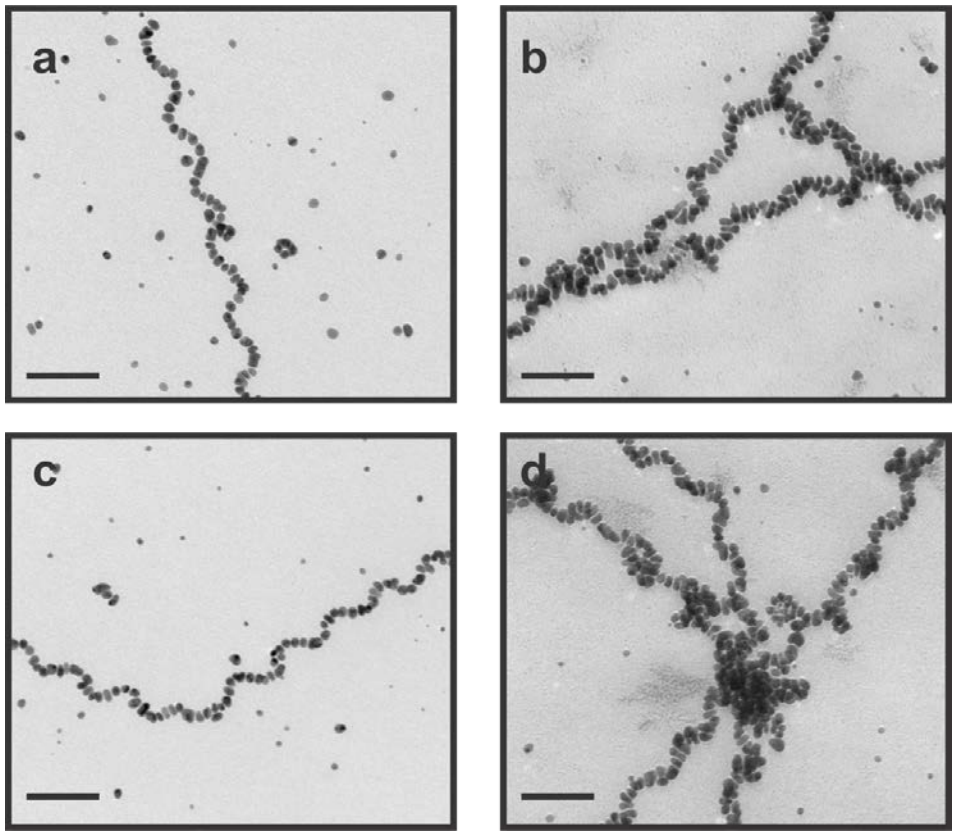

Figure S74. TEM analysis of single-helical superstructures formed by (a, c) C_{18}-$(PEP_{Au}{}^{M\text{-}ox,\,9})_2$ and (b, d) C_{18}-$(PEP_{Au}{}^{M\text{-}ox,\,11})_2$. Scale bar: 100 nm.

Additional Information on Computational Methodology

We performed REST-MD simulations for each of the six peptides ($PEP_{Au}^{M, 7}$, $PEP_{Au}^{M, 9}$, $PEP_{Au}^{M, 11}$, $PEP_{Au}^{M\text{-}ox, 7}$, $PEP_{Au}^{M\text{-}ox, 9}$, $PEP_{Au}^{M\text{-}ox, 11}$) both in the unadsorbed state and adsorbed at the aqueous Au(111) interface.

General Simulation Set-up Details: We used an orthorhombic periodic cell and periodic boundary conditions were applied in all three principal directions. All simulations were performed in the Canonical (NVT) ensemble, at a thermal temperature of 300K, maintained using the Nosé-Hoover thermostat,[137,138] with a coupling constant of τ = 0.2 ps. Newton's equations of motion were solved using an integration time-step of 1fs. Coordinates were saved every 1ps. Long-ranged electrostatic interactions were treated using Particle-mesh Ewald (PME),[139] with a cut-off at 11 Å, whereas a force-switched cut-off, starting at 9 Å and ending at 10 Å was used for the Lennard-Jones non-bonded interactions.

The GolP-CHARMM[99] force-field was used to model the Au slab. The peptides were described based on the CHARMM22* force-field[104,105] and water was described using the modified TIP3P[140,107] model. All Au atoms in the slab were held fixed in space during these simulations, with only the Au atom dipoles able to freely rotate. Random initial dipole positions were used throughout. Our recent tests indicate that there is very little difference between binding obtained using a rigid substrate, vs. using a slab where all atoms can move.[141]

Replica Exchange with Solute Tempering Molecular Dynamics (REST-MD) Simulations: Our simulation results comprise output from twelve simulations in total; six simulations for each of the peptides considered in this work, in both the surface-adsorbed and unadsorbed states. For the surface-adsorbed simulations, our system comprised one peptide chain; a Au slab, five atomic layers thick, presenting the Au(111) surface on both slab facets; and ~6000

TIP3P water molecules. The dimensions of the simulation cell were ~ 58 × 61 × 68 Å, with the Au slab placed in the *x,y* plane. The dimension of the periodic cell perpendicular to the slab plane was adjusted such that the density of liquid water in the center of the space between the slab and its periodic image recovered the target density of bulk liquid water at 300 K using the modified TIP3P model. For the unadsorbed simulations, the setup was similar except that we used a cubic periodic simulation cell with ~6600 modified TIP3P water molecules.

We used the Gromacs software package, v5.1.3.[142] Full technical details of the Terakawa implementation[97] of REST have been given by us previously.[98] In our REST simulations, we spanned an 'effective temperature' window of 300-430K, using 16 replicas. The initial configurations for each replica spanned a wide range of conformations and secondary structures. The adsorbate structure for each replica was initially placed within ~5Å distance from the top surface of the Au slab. The 16 values of lambda used to scale our force-field were:

λj = 0.000, 0.057, 0.114, 0.177, 0.240, 0.310, 0.382, 0.458, 0.528, 0.597, 0.692, 0.750, 0.803, 0.855, 0.930, 1.000.

Prior to initiation of each REST-MD simulation, the 16 initial configurations were equilibrated at their target potential for 0.5 ns, with no exchange moves attempted during this time. During the REST simulations, the interval between exchange attempts was set to every 1 ps. All production REST simulations were run for a total of 15 $\times 10^6$ MD steps (15 ns).

REST MD Clustering Analysis: Detailed analysis was carried out on the constant-ensemble run that corresponded to an effective temperature of 300K (replica 0; herein referred to as the reference trajectory). We classified the Boltzmann-weighted ensemble of conformations from our reference trajectories into groups of "like structures", on the basis of similarity of their backbone structures. This was accomplished using the Daura clustering algorithm[143] with a root

mean-squared deviation (RMSD) cutoff between the positions all peptide backbone atoms of 2 Å. Our extensive experience based on clustering analyses of dodecapeptides informed our identification of this cutoff value. We performed our clustering analysis over the entire 15 ns trajectory in each case. This analysis yields several principal outputs; the number of clusters (i.e. the number of distinct peptide conformations), the population of each cluster in the ensemble, and the representative structure (*i.e.* cluster centroid) of each cluster.The population of a given cluster was calculated as the percentage fraction of the number of frames that were assigned membership of that cluster, divided by the total number of frames in the trajectory. The cluster with the largest population corresponds with the most likely structure of the peptide.

For our cross-cluster analysis, we compared the set of cluster centroid structures generated for two different peptides, based on the mathematical similarity of their backbone conformations. We accomplished this by alligning the backbone structure of each cluster centroid of peptide1 against the backbone structure of each cluster centroid of peptide2. Similarity was determined on the basis of the RMSD in backbone atom positions, with a "match" denoted as an RMSD of less than the clustering cutoff (2Å), and a "near match" corresponding to an RMSD of less than 2.5 Å. The analysis can identify if two peptides feature a similar set of backbone conformations (secondary structures).

REST MD Contact Residue Analysis: To quantify residue-surface contact for each reference trajectory, we calculated the distance between the topmost layer of the Au surface and each residue in the peptide sequence. For a residue to be determined as in contact with the surface, the residue-surface separation was required to be within a residue-specific distance cut-off. The cut-offs used here have been published elsewhere[101], along with the corresponding reference site for each residue. For methionine sulfoxide, we used the sulfur atom as the reference site and used

the same cut-off that was used for methionine.We calculated the percentage of frames in the reference trajectory for which each residue was found within the contact range of surface-residue separation.

First Principles Calculations: Plane-wave density functional theory calculations were carried out for dimethyl sulfoxide adsorbed onto the Au(111) surface in vacuo, using Quantum Espresso (version 5.2.0).[108] For consistency, we followed the same approach that was used to derive the GolP-CHARMM force-field. Three-dimensional periodic boundary conditions were employed using a $3 \times 3\sqrt{3}$ supercell (Au−Au lattice parameter of 2.93 Å[144]). A gold slab four atomic layers thick was used. Calculations were performed using vdW-DF[93,94,95] with the revPBE exchange-correlation functional[109] and ultrasoft pseudopotentials[145] (based on the PBE exchange-correlation functional[146]). Plane wave kinetic energies and electron densities were truncated at 25 and 200 Ry, respectively.

The optimal adsorbate−gold geometry was obtained by relaxing the structure of dimethyl sulfoxide when in close proximity to the surface (to a convergence criterion of 0.026 eV/Å). We used a vacuum thickness of 10 Å (perpendicular to the Au plane) to minimize interactions between periodic images, and a Monkhorst−Pack *k*-point mesh of 4 × 4 × 1 for the geometry optimization. The interaction energy, ΔE_{mol_Au}, was calculated using the supermolecule approach, according to:

$$\Delta E_{mol\_Au} = E_{mol\_Au} - E_{mol} - E_{Au}$$

where E_{mol_Au}, E_{mol}, and E_{Au} are the total energies of systems describing the small molecule adsorbed at the interface, the adsorbate only, and the gold slab only, respectively. A thicker vacuum layer of 15 Å and a finer Monkhorst−Pack *k*-point mesh of 6 × 8 × 1 was employed in the single-point energy calculation.

Appendix D

Supporting Information for Chapter 5: “Deliberate Introduction of Particle Anisotropy in Helical AuNP Superstructures”

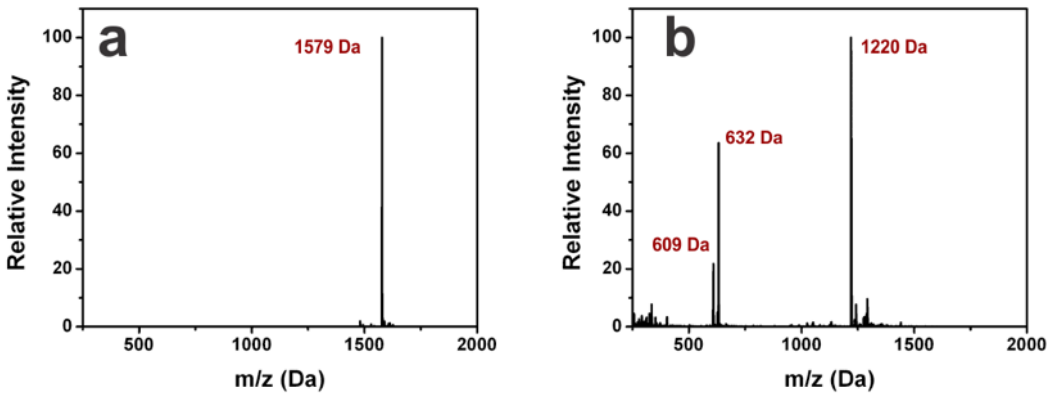

Figure S75. LC-MS characterization of C_{18}-$(PEP_{Au}^{M\text{-}ox})_2$ and PEP_{Au}. (a) Negative mode ionization spectra of C_{18}-$(PEP_{Au}^{M\text{-}ox})_2$ reveals m/z = 1578.8 Da which corresponds to $(M\text{-}2H^+)/2$ value. (b) Negative mode ionization spectrum of PEP_{Au} reveals three m/z values: 1220 Da which corresponds to $(M\text{-}H^+)$, 632 Da which correspond to $(M\text{-}H^+ + CH_3COO^-)/2$, and 609 Da which correspond to $(M\text{-}2H^+)/2$.

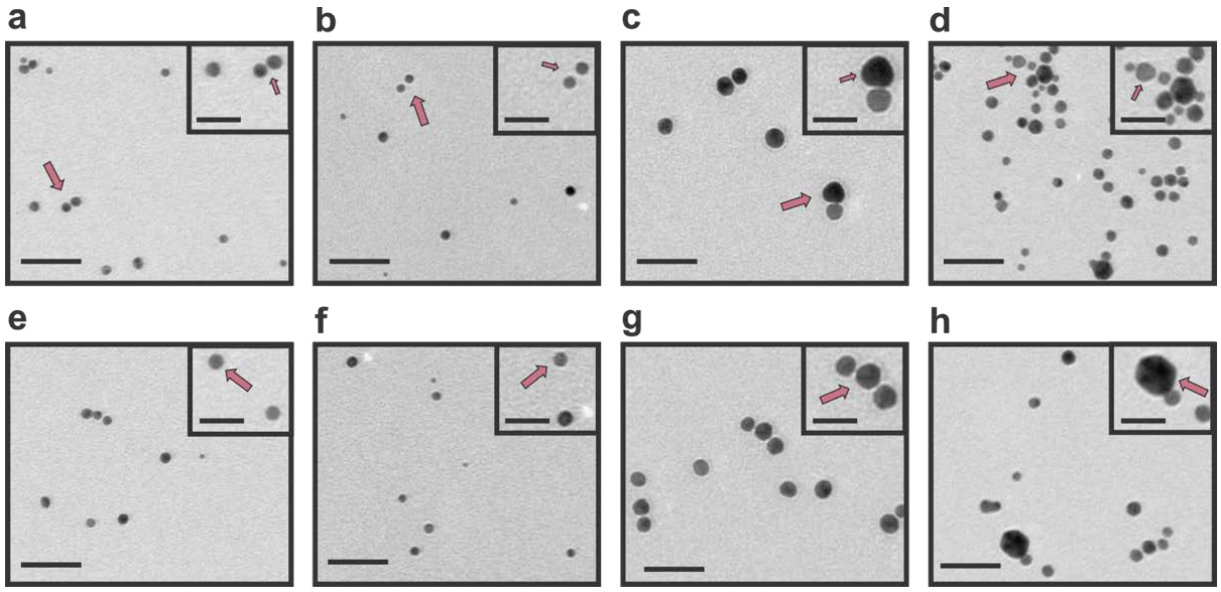

Figure S76. Effect of NH_4Br on the PEP_{Au}-mediated synthesis of AuNPs. AuNPs synthesized in the absence of NH_4Br (a, e), in the presence of 100 μM NH_4Br (b, f), 400 μM NH_4Br (c, g), and 1000 μM NH_4Br (d, h). Arrows in a, b, e, and f indicate spherical particles; arrows in c, d, g, and h indicate faceted anisotropic particles. Scale bar: 50 nm, inset scale bar: 25 nm.

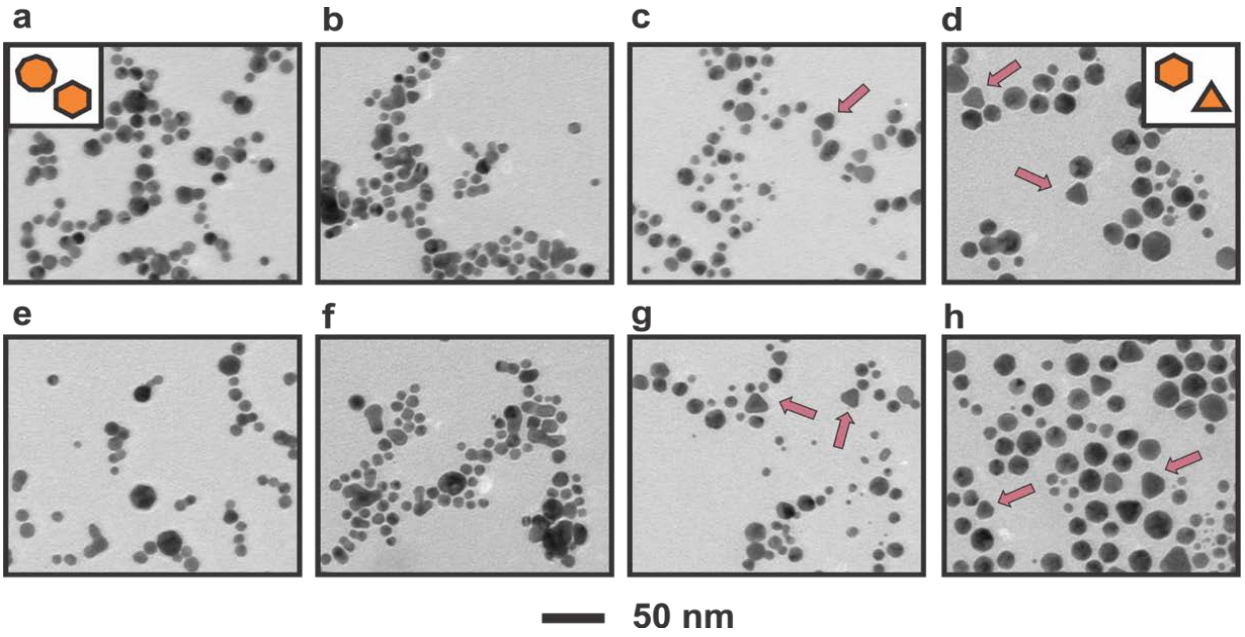

Figure S77. Effect of $C_{10\text{-}16}$TAB on the PEP_{Au}-mediated synthesis of AuNPs. AuNPs synthesized in the presence of 1000 μM C_{10}TAB (a, e), C_{12}TAB (b, f), C_{14}TAB (c, g), C_{16}TAB (d, h). Arrows indicate faceted prismatic particles.

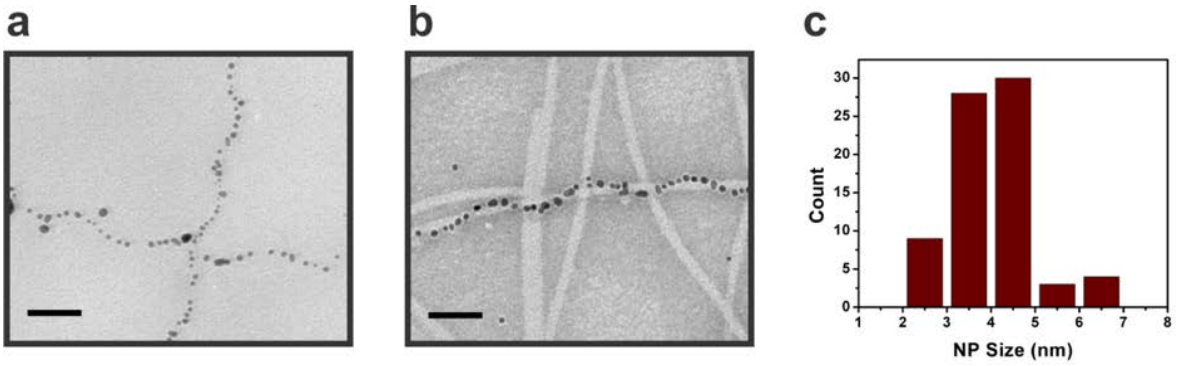

Figure S78. TEM images of AuNP single helices after a) 5 minute and b) 30 minute of reaction indicate spherical component particles. (c) Size distribution of component particles at the 5 minute timepoint. Scale bar: 50 nm.

.

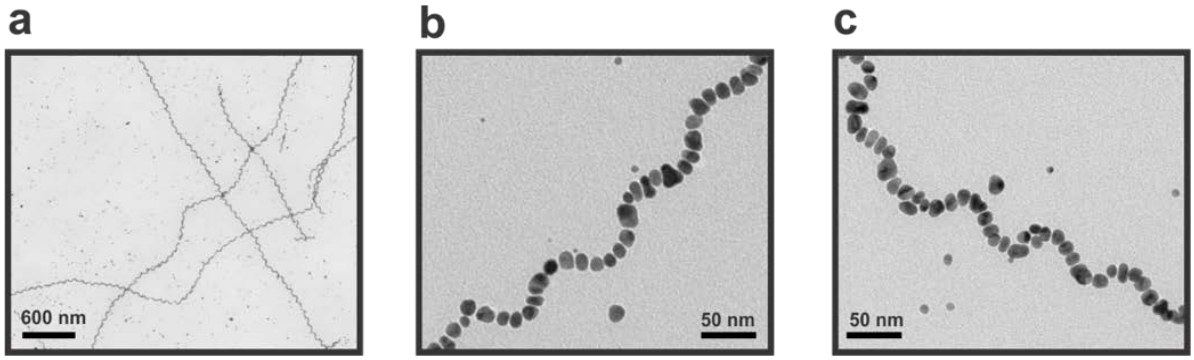

Figure S79. TEM images of AuNP single helices after 16 hours of reaction indicate oblong component particles.

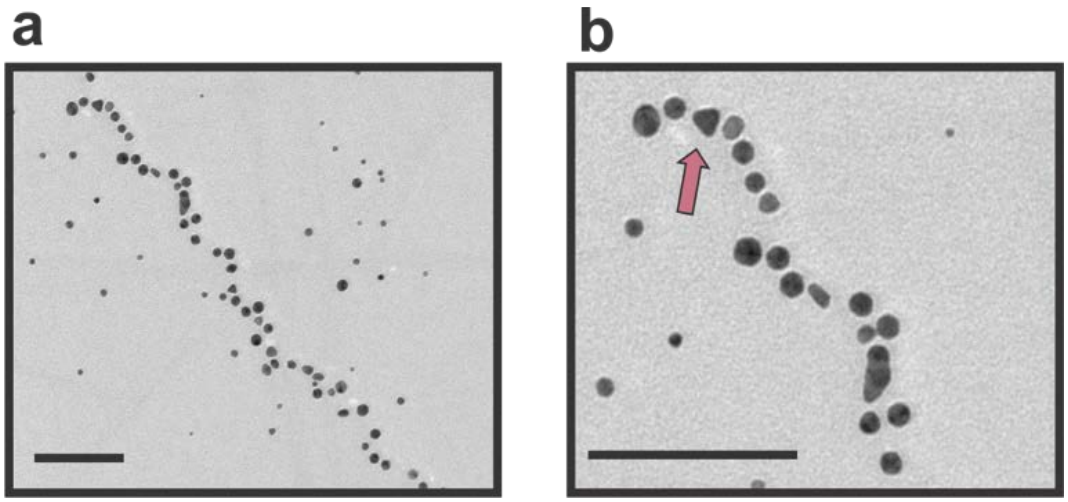

Figure S80. Effect of C_{10}TAB on C_{18}-$(PEP_{Au}{}^{M\text{-}ox})_2$-mediated assembly of AuNP single helices. Assemblies exhibit helical morphology. Few component particles exhibit prismatic shapes. Scale bar: 100 nm.

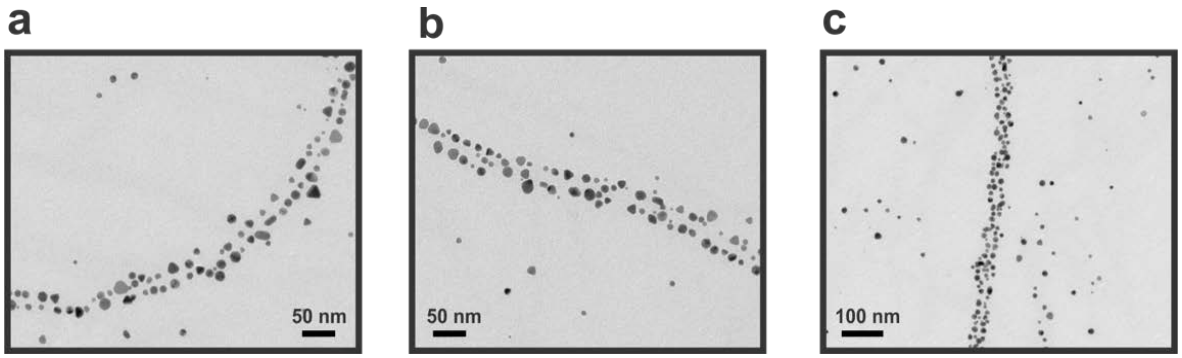

Figure S81. Effect of C_{16}TAB on C_{18}-$(PEP_{Au}^{M\text{-}ox})_2$-mediated assembly of AuNPs. Large number of component AuNPs exhibit prismatic shape.

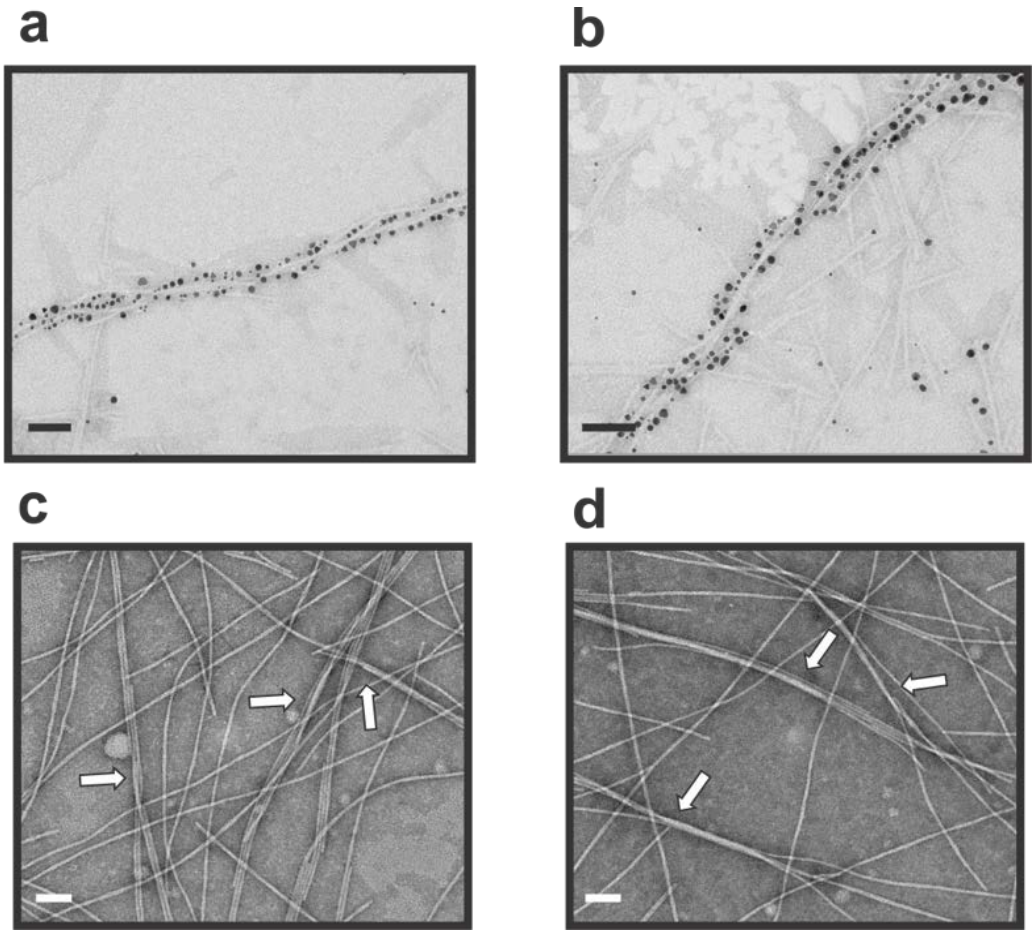

Figure S82. Negative staining analysis of C_{18}-$(PEP_{Au}{}^{M\text{-}ox})_2$ fiber bundles formed in the presence of 1000 μM C_{16}TAB. (a, b) TEM images of fiber bundles underlying the AuNP superstructures formed in the presence of C_{16}TAB. (c, d) TEM images of C_{18}-$(PEP_{Au}{}^{M\text{-}ox})_2$ fiber bundles formed in the presence of C_{16}TAB alone. Scale bar = 100 nm.

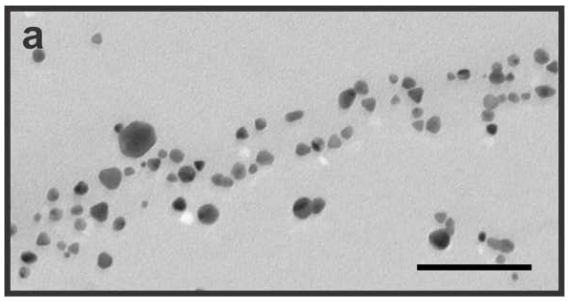

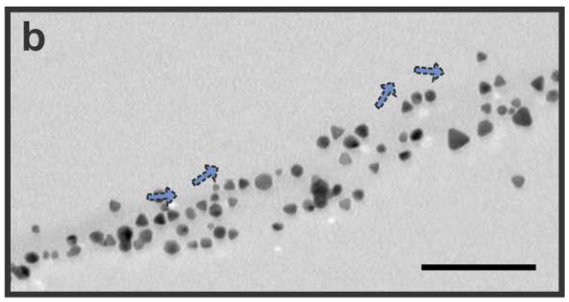

c

C_{16}TAB conc. (μM)	Spherical (%)	Anisotropic (%)
1000	~ 38.5 ± 2	~ 61 ± 3
2000	~ 31 ± 3	~ 68 ± 4

Figure S83. Effect of C_{16}TAB concentration on the morphology of AuNP superstructures and the percentage of spherical and anisotropic particles. (a, b) TEM images of AuNP superstructures prepared in the presence of 2000 μM C_{16}TAB (Scale bar: 100 nm). These superstructures display decreased helical morphology. Blue arrows show helical directionality. (c) Table comparing the percentage of spherical and anisotropic particles observed at 1000 μM and 2000 μM C_{16}TAB concentrations (based on ~200 counts).

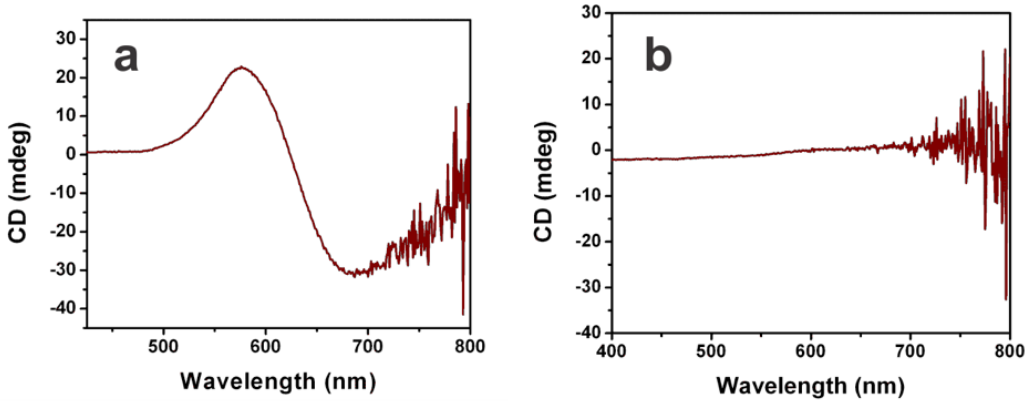

Figure S84. Chiroptical response of the AuNP assemblies. (a) Single-helical superstructures composed of oblong particles display strong chiroptical activity. (b) Intertwined helical superstructures comprising prismatic particles, prepared in the presence of C_{16}TAB, do not exhibit observable chiroptical activity.

Bibliography

1. Fujii, N.; Saito, T. *Chem. Rec.* **2004**, *4* (5), 267-278.

2. Pendry, J. B. *Science* **2004**, *306* (5700), 1353.

3. Gansel, J. K.; Thiel, M.; Rill, M. S.; Decker, M.; Bade, K.; Saile, V.; von Freymann, G.; Linden, S.; Wegener, M. *Science* **2009**, *325* (5947), 1513-1515.

4. Decker, M.; Klein, M. W.; Wegener, M.; Linden, S. *Opt. Lett.* **2007**, *32*, 856-858.

5. Smith, D. R.; Pendry, J. B.; Wiltshire, M. C. K. *Science* **2004**, *305*, 788-792.

6. Rogacheva, A. V.; Fedotov, V. A.; Schwanecke, A. S.; Zheludev, N. I. *Phys. Rev. Lett.* **2006**, *97*, 177401(1-4).

7. Pendry, J. B. *Phys. Rev. Lett.* **2000**, *85* (18), 3966-3969.

8. Zhu, Y.; Xu, L.; Ma, W.; Xu, Z.; Kuang, H.; Wang, L.; Xu, C. *Chem. Commun.* **2011**, *48*, 11889-11891.

9. Plum, E.; Zhou, J.; Dong, J.; Fedetov, V. A.; Koschny, T.; Soukoulis, C. M.; Zheludev, N. I. *Phys. Rev. B* **2009**, *79* (3), 035407(1-6).

10. Zhang, S.; Park, Y,-S.; Li, J.; Lu, X.; Zhang, W.; Zhang, X. *Phys. Rev. Lett.* **2009**, *102* (2), 023901.

11. Kumar, J.; Eraña., H.; López-Martínez, E.; Claes, N.; Martín, V. F.; Solís, D. M.; Bals, S.; Cortajarena, A. L.; Castilla, J.; Liz-Marzán, L. M. *Proc. Natl. Acad. Sci.* **2018**, *115* (13), 3225-3230.

12. Shukla, N. B., M. A.; Gellman, A. J., Enantioselective Separation on Chiral Au Nanoparticles. *J. Am. Chem. Soc.* **2010**, *132* (25), 8575-8580.

13. Sivaguru, J.; Poon, T.; Franz, R.; Jockusch, S.; Adam, W.; Turro, N. J. *J. Am. Chem. Soc.* **2004**, *126* (35), 10816-10817.

14. Maier, S. A. *Plasmonics: Fundamentals and Applications*. *Springer* **2007**.

15. Kelly, K. L.; Coronado, E.; Zhao, L.; Schatz, G. C. *J. Phys. Chem. B* **2003**, *107* (3), 668-677.

16. Lee, K.-S.; El-Sayed, M. A. *J. Phys.Chem. B* **2006**, *110* (39), 19220-19225.

17. Alivisatos, A. P. *Science* **1996**, *271* (5251), 933-937.

18. Fan, Z.; Govorov, A. O. *Nano Lett.* **2010**, *10* (7), 2580-2587.

19. Ben-Moshe, A.; Maoz, B. M.; Govorov, A. O.; Markovich, G. *Chem. Soc. Rev.* **2013**, *42* (16), 7028-7041.

20. Berova, N.; Di Bari, L.; Pescitelli, G. *Chem. Soc. Rev.* **2007**, *36*, 914-931.

21. Guerrero-Martínez, A., Auguié, B., Alonso-Gómez, J. L., Džolić, Z., Gómez-Graña, S., Žinić, M., Cid, M. M.; Liz-Marzán, L. M. *Angew. Chem. Int. Ed.* **2011**, *50*, 5499-5503.

22. Merg, A. D.; Boatz, J. C.; Mandal, A.; Zhao, G.; Mokashi-Punekar, S.; Liu, C.; Wang, X.; Zhang, P.; van der Wel, P. C. A.; Rosi, N. L. *J. Am. Chem. Soc.* **2016**, *138* (41), 13655-13663.

23. Burkett, S. L.; Mann.; S. *Chem. Commun.* **1996**, 321-322.

24. Sone, E. D.; Zubarev, E. R.; Stupp, S. I. *Angew. Chem. Int. Ed.* **2002**, *41*, 1705-1709.

25. Fu, X.; Wang, Y.; Huang, L.; Sha, Y.; Gui, L.; Lai, L.; Tang, Y. *Adv. Mater.* **2003**, *15*, 902–906.

26. Chen, C.-L.; Zhang, P.; Rosi, N. L. *J. Am. Chem. Soc.* **2008**, *130* (41), 13555-13557.

27. Mastroianni, A. J.; Claridge, S. A.; Alivisatos, A. P. *J. Am. Chem. Soc.* **2009**, *131* (24), 8455-8459.

28. Urban, M. J.; Dutta, P. K.; Wang, P.; Duan, X.; Shen, X.; Ding, B.; Ke, Y.; Liu, N. *J. Am. Chem. Soc.* **2016**, *138* (17), 5495-5498.

29. Wu, X.; Xu, L.; Ma, W.; Liu, L.; Kuang, H.; Kotov, N. A.; Xu, C. *Adv. Mater.* **2016**, *28* (28), 5907-5915.

30. Wu, X.; Xu, L.; Liu, L.; Ma, W.; Yin, H.; Kuang, H.; Wang, L.; Xu, C.; Kotov, N. A. *J. Am. Chem. Soc.* **2013**, *135* (49), 18629-18636.

31. Yan, W.; Xu, L.; Xu, C.; Ma, W.; Kuang, H.; Wang, L.; Kotov, N. A. *J. Am. Chem. Soc.* **2012**, *134* (36), 15114-15121.

32. Ma, W.; Xu, L.; de Moura, A. F.; Wu, X.; Kuang, H.; Xu, C.; Kotov, N. A. *Chem. Rev.* **2017**, *117* (12), 8041-8093.

33. Zhou, C.; Duan, X.; Liu, N. *Acc. Chem. Res.* **2017**, *50* (12), 2906-2914.

34. Sharma, J.; Chhabra, R.; Cheng, A.; Brownell, J.; Liu, Y.; Yan, H. *Science* **2009**, *323* (5910), 112-116.

35. Chen, W.; Bian, A.; Agarwal, A.; Liu, L.; Shen, H.; Wang, L.; Xu, C.; Kotov, N. *Nano. Lett.* **2009**, *9* (5), 2153-2159.

36. Govorov, A. O.; Gun'ko, Y. K.; Slocik, J. M.; Gerard, V. A.; Fan, Z.; Naik, R. R. *J. Mater. Chem.* **2011**, *21* (42), 16806-16818.

37. Fan, Z.; Govorov, A. O. *J. Phys. Chem. C* **2011**, *115* (27), 13254-13261.

38. Shen, X.; Song, C.; Wang, J.; Shi, D.; Wang, Z.; Liu, N.; Ding, B. *J. Am. Chem. Soc.* **2012**, *134* (1), 146-149.

39. Wang, Y.; Wang, Q.; Sun, H.; Zhang, W.; Chen, G.; Wang, Y.; Shen, X.; Han, Y.; Lu, X.; Chen, H. *J. Am. Chem. Soc.* **2011**, *133* (50), 20060-20063.

40. Kuzyk, A.; Schreiber, R.; Fan, Z.; Pardatscher, G.; Roller, E.-M.; Hogele, A.; Simmel, F. C.; Govorov, A. O.; Liedl, T. *Nature* **2012**, *483* (7389), 311-314.

41. Ma, W.; Kuang, H.; Xu, L.; Ding, L.; Xu, C.; Wang, L.; Kotov, N. A. *Nat. Commun.* **2013**, *4*, 2689.

42. Lan, X.; Chen, Z.; Dai, G.; Lu, X.; Ni, W.; Wang, Q. *J. Am. Chem. Soc.* **2013**, *135* (31), 11441-11444.

43. Shen, X.; Asenjo-Garcia, A.; Liu, Q.; Jiang, Q.; García de Abajo, F. J.; Liu, N.; Ding, B. *Nano Lett.* **2013**, *13* (5), 2128-2133.

44. Singh, G.; Chan, H.; Baskin, A.; Gelman, E.; Repnin, N.; Král, P.; Klajn, R. *Science* **2014**, *645*, 1149-1153.

45. Yeom, J.; Yeom, B.; Chan, H.; Smith, K. W.; Dominguez-Medina, S.; Bahng, J. H.; Zhao, G.; Chang, W,-S.; Chang, S,-J.; Chuvilin, A.; Melnikau, D.; Rogach, A. L.; Zhang, P.; Link, S.; Král, P.; Kotov, N. A. *Nat. Mater.* **2015**, *14*, 66-72.

46. Lu, X.; Song, D.-P.; Ribbe, A.; Watkins, J. J. *Macromolecules* **2017**, *50* (14), 5293-5300.

47. Hirai, K.; Yeom, B.; Sada, K. *ACS Nano* **2017**, *11* (6), 5309-5317.

48. Bai, P.; Yang, S.; Bao, W.; Kao, J.; Thorkelsson, K.; Salmeron, M.; Zhang, X.; Xu, T. *Nano. Lett.* **2017**, *17* (11), 6847-6854.

49. Chu, G.; Wang, X.; Chen, T.; Gao, J.; Gai, F.; Wang, Y.; Xu, Y. *ACS. Appl. Mater. Interfaces* **2015**, *7* (22), 11863-11870.

50. Song, C.; Blaber, M. G.; Zhao, G.; Zhang, P.; Fry, H. C.; Schatz, G. C.; Rosi, N. L. *Nano Lett*, **2013**, *13* (7), 3256-3261.

51. Eisenberg, D. *Proc. Natl. Acad. Sci. USA* **2003**, *100* (20), 11207-11210.

52. Adzhubei, A. A.; Sternberg, M. J. E.; Makarov, A. A. *J.Mol. Biol.* **2013**, *425* (12), 2100-2132.

53. Hartgerink, J. D.; Beniash, E.; Stupp, S. I. *Science* **2001**, *294* (5547), 1684.

54. Adler-Abramovich, L.; Gazit, E. *Chem. Soc. Rev.* **2014**, *43* (20), 6881-6893.

55. Hendricks, M. P.; Sato, K.; Palmer, L. C.; Stupp, S. I. *Acc. Chem. Res.* **2017**, *50* (10), 2440-2448.

56. Reches, M.; Gazit, E. *Science* **2003**, *300*, 625-627.

57. Yan, X.; Zhu, P.; Li, J. *Chem. Soc. Rev.* **2010**, *39*, 1877-1890.

58. Wadai, H.; Yamaguchi, K.-i.; Takahashi, S.; Kanno, T.; Kawai, T.; Naiki, H.; Goto, Y. *Biochemistry* **2005**, *44* (1), 157-164.

59. Sawaya, M. R.; Sambashivan, S.; Nelson, R.; Ivanova, M. I.; Sievers, S. A.; Apostol, M. I.; Thompson, M. J.; Balbirnie, M.; Wiltzius, J. J. W.; McFarlane, H. T.; Madsen, A. O.; Riekel, C.; Eisenberg, D. *Nature* **2007**, *447* (7143), 453-457.

60. Rubin, N.; Perugia, E.; Goldschmidt, M.; Fridkin, M.; Addadi, L. *J. Am. Chem. Soc.* **2008**, *130* (14), 4602-4603.

61. Lu, K.; Jacob, J.; Thiyagarajan, P.; Conticello, V.; Lynn, D. G. *J. Am. Chem. Soc.* **2003**, *125* (21), 6391-6393.

62. Morris, K. L.; Chen, L.; Raeburn, J.; Sellick, O. R.; Cotanda, P.; Paul, A.; Griffiths, P. C.; King, S. M.; O'Reilly, R. K.; Serpell, L. C.; Adams, D. J. *Nat. Commun.* **2013**, *4*, 1480.

63. Muraoka, T.; Cui, H.; Stupp, S. I. *J. Am. Chem. Soc.* **2008**, *130* (10), 2946-2947.

64. Kumar, M.; Ing, N. L.; Narang, V.; Wijerathne, N. K.; Hochbaum, A. I.; Ulijn, R. V. *Nat. Chem.* **2018**, *10*, 696-703.

65. Cha, J. N.; Shimizu, K.; Zhou, Y.; Christiansen, S. C.; Chmelka, B. F.; Stucky, G. D.; Morse, D. E. *Proc. Natl. Acad. Sci. USA* **1999**, *96* (2), 361-365.

66. Whaley, S. R.; English, D. S.; Hu, E. L.; Barbara, P. F.; Belcher, A. M. *Nature* **2000**, *405* (6787), 665-668.

67. Sarikaya, M.; Tamerler, C.; Jen, A. K.-Y.; Schulten, K.; Baneyx, F. *Nat. Mater.* **2003**, *2* (9), 577-585.

68. Slocik, J. M. Stone, M. O.; Naik, R. R. *Small* **2005**, *1*, 1048-1052.

69. Yu, J.; Becker, M. L.; Carri, G. A. *Langmuir* **2012**, *28*, 1408-1417.

70. Bedford, N. M.; Hughes, Z. E.; Tang, Z.; Li, Y.; Briggs, B. D.; Ren, Y.; Swihart, M. T.; Petkov, V. G.; Naik, R. R.; Knecht, M. R.; Walsh, T. R. *J. Am. Chem. Soc.* **2016**, *138* (2), 540-548.

71. Chen, C.-L.; Rosi, N. L. *J. Am. Chem. Soc.* **2010**, *132* (20), 6902-6903.

72. Hwang, L.; Zhao, G.; Zhang, P.; Rosi, N. L. *Small* **2011**, *7*, 1939-1942.

73. Song, C.; Wang, Y.; Rosi, N. L. *Angew. Chem. Int. Ed.* **2013**, *125*, 4085-4087.

74. Zhang, C.; Zhou, Y.; Merg, A.; Song, C.; Schatz, G. C.; Rosi, N. L. *Nanoscale* **2014**, *6* (21), 12328-12332.

75. Zhang, C.; Song, C.; Fry, H. C.; Rosi, N. L. *Chem. Eur. J.* **2014**, *20*, 941-945.

76. Guerrero-Martínez, A.; Alonso-Gómez, J. L.; Auguié, B.; Cid, M. M.; Liz-Marzán, L. M. *Nano Today* **2011**, *6* (4), 381-400.

77. Tang, L.; Li, S.; Xu, L.; Ma, W.; Kuang, H.; Wang, L.; Xu, C. *ACS Appl. Mater. Interfaces* **2015**, *7* (23), 12708-12712.

78. Zhao, Y.; Belkin, M. A.; Alù, A. *Nat. Commun.* **2012**, *3*, 870.

79. Lan, X.; Lu, X.; Shen, C.; Ke, Y.; Ni, W.; Wang, Q. *J. Am. Chem. Soc.* **2015**, *137* (1), 457-462.

80. Cecconello, A.; Kahn, J. S.; Lu, C.-H.; Khorashad, L. K.; Govorov, A. O.; Willner, I. *J. Am. Chem. Soc.* **2016**, *138* (31), 9895-9901.

81. Cui, H.; Webber, M. J.; Stupp, S. I. *Biopolymers* **2010**, *94*, 1-18.

82. Stendahl, J. C.; Rao, M. S.; Guler, M. O.; Stupp, S. I. *Adv. Funct. Mater.* **2006**, *16*, 499-508.

83. Paramonov, S. E.; Jun, H.-W.; Hartgerink, J. D. *J. Am. Chem. Soc.* **2006**, *128* (22), 7291-7298.

84. Jiang, H.; Guler, M. O.; Stupp, S. I. *Soft Matter* **2007**, *3* (4), 454-462.

85. Barth, A. *Biochim. Biophys. Acta, Bioenerg.* **2007**, *1767* (9), 1073-1101.

86. Heinz, H.; Farmer, B. L.; Pandey, R. B.; Slocik, J. M.; Patnaik, S. S.; Pachter, R.; Naik, R. R. *J. Am. Chem. Soc.* **2009**, *131* (28), 9704-9714.

87. Zanna, N.; Milli, L.; Del Secco, B.; Tomasini, C. *Org. Lett.* **2016**, *18* (7), 1662-1665.

88. Hartgerink, J. D.; Beniash, E.; Stupp, S. I. *Proc. Natl. Acad. Sci. USA* **2002**, *99* (8), 5133-5138.

89. Cui, H.; Cheetham, A. G.; Pashuck, E. T.; Stupp, S. I. *J. Am. Chem. Soc.* **2014**, *136* (35), 12461-12468.

90. Wang, S.-T.; Lin, Y.; Spencer, R. K.; Thomas, M. R.; Nguyen, A. I.; Amdursky, N.; Pashuck, E. T.; Skaalure, S. C.; Song, C. Y.; Parmar, P. A.; Morgan, R. M.; Ercius, P.; Aloni, S.; Zuckermann, R. N.; Stevens, M. M. *ACS Nano* **2017**, *11*, 8579-8589.

91. Manavalan, P.; Ponnuswamy, P. K. *Nature* **1978**, *275*, 673-674.

92. Merg, A. D.; Slocik, J.; Blaber, M. G.; Schatz, G. C.; Naik, R.; Rosi, N. L. *Langmuir* **2015**, *31* (34), 9492-9501.

93. Dion, M.; Rydberg, H.; Schroder, E.; Langreth, D. C.; Lundqvist, B. I. *Phys. Rev. Lett.* **2004**, *92*, 246401-1.

94. Thonhauser, T.; Cooper V. R.; Li, S.; Puzder, A.; Hyldgaard, P.; Langreth, D. C. *Phys. Rev. B* **2007**, *76*.

95. Roman-Perez, G.; Soler, J. M. *Phys. Rev. Lett.* **2009**, *103*.

96. Wright, L. B.; Rodger, P. M.; Walsh, T. R.; Corni, S. *J. Phys. Chem. C* **2013**, *117*, 24292-24306.

97. Terakawa, T.; Kameda, T.; Takada, S. *J. Comput. Chem.* **2010**, *32*, 1228-1234.

98. Wright, L. B.; Walsh T. R. *Phys. Chem. Chem. Phys* **2013**, *15*, 4715-4726.

99. Wright, L. B.; Rodger, P. M.; Corni, S.; Walsh, T. R. *J. Chem. Theory Comput.* **2013**, *9* (3), 1616-1630.

100. Wright, L. B.; Palafox-Hernandez, J. P.; Rodger, P. M.; Corni, S.; Walsh, T. R. *Chem. Sci.* **2015**, *2015*, 5204-5214.

101. Tang, Z.; Palafox-Hernandez, J. P.; Law, W.-C.; Hughes, Z. E.; Swihart, M. T.; Prasad, P. N.; Knecht, M. R.; Walsh, T. R. *ACS Nano* **2013**, *7*, 9632-9646.

102. Hughes, Z. E.; Nguyen, M. A.; Li, Y.; Swihart, M. T.; Walsh, T. R.; Knecht, M. R. *Nanoscale* **2017**, *9*, 421-432.

103. Hughes, Z. E.; Kochandra, R.; Walsh, T. R. *Langmuir* **2017**, *33*, 3742-3754.

104. MacKerell, A. D.; Bashford, D.; Bellott, M.; Dunbrack, R. L.; Evanseck, J. D.; Field, M. J.; Fischer, S.; Gao, J.; Guo, H.; Ha, S.; Joseph-McCarthy, D.; Kuchnir, L.; Kuczera, K.; Lau, F. T. K.; Mattos, C.; Michnick, S.; Ngo, T.; Nguyen, D. T.; Prodhom, B.; Reiher, W. E.; Roux, B.; Schlenkrich, M.; Smith, J. C.; Stote, R.; Straub, J.; Watanabe, M.; Wiórkiewicz-Kuczera, J.; Yin, D.; Karplus, M. *J. Phys. Chem. B* **1998**, *102* (18), 3586-3616.

105. Piana, S.; Lindorff-Larsen, K.; Shaw, D. E. *Biophys. J.* **2011**, *100*, L47-L49.

106. Jorgensen, W. L.; Chandrasekhar, J.; Madura, J. D.; Impey, R.W.; Klein, M. L. *J. Chem. Phys.* **1983**, *79*, 926-935.

107. Neria, E.; Fischer, S.; Karplus, M. *J. Chem. Phys.* **1996**, *105*, 1902.

108. Giannozzi, P.; Baroni, S.; Bonini, N.; Calandra, M.; Car, R.; Cavazzoni, C.; Ceresoli, D.; Chiarotti, G. L.; Cococcioni, M.; Dabo, I.; Corso, A. D.; de Gironcoli, S.; Fabris, S.; Fratesi, G.; Gebauer, R.; Gerstmann, U.; Gougoussis, C.; Kokalj, A.; Lazzeri, M.; Martin-Samos, L.; Marzari, N.; Mauri, F.; Mazzarello, R.; Paolini, S.; Pasquarello, A.; Paulatto, L.; Sbraccia, C.; Scandolo, S.; Sclauzero, G.; Seitsonen, A. P.; Smogunov, A.; Umari, P.; Wentzcovitch, R. M. *J. Phys. Condens. Matter* **2009**, *21*, 395502.

109. Hammer, B.; Hansen, L. B.; Norskov, J. K. *Phys. Rev. B* **1999**, *59*, 7413-7421.

110. Murphy, C. J.; Sahu, T. K.; Gole, A. M.; Orendorff, C. J.; Gao, J.; Gou, L; Hunyadi, S. E.; Li, T. *J. Phys. Chem. B* **2005**, *109* (29), 13857-13870.

111. Burrows, N. D.; Vartanian, A. M.; Abadeer, N. S.; Grzincic, E. M.; Jacob, L. M.; Lin, W.; Li, J.; Dennison, J. M.; Hinman, J. G.; Murphy, C. J. *J. Phys. Chem. Lett.* **2016**, *7* (4), 632-641.

112. Gole, A.; Murphy, C. J. *Chem. Mater.* **2004**, *16* (19), 3633-3640.

113. Nikoobakht, B.; Wang, Z. L.; El-Sayed, M. A. *J. Phys. Chem. B* **2000**, *104* (36), 8635-8640.

114. Ye, X.; Gao, Y.; Chen, J.; Reifsnyder, D. C.; Zheng, Chen.; Murray, C. B. *Nano Lett.* **2013**, *13* (5), 2163-2171.

115. Grzelczak, M.; Perez-Juste, J.; Mulvaney, P.; Liz-Marzán, L. M. *Chem. Rev.* **2008**, *37*, 1783-1791.

116. Millstone, J. E.; Hurst, S. J.; Métraux, G. S.; Cutler, J. I.; Mirkin, C. A. *Small* **2009**, *5* (6), 646-664.

117. Millstone, J. E.; Wei, W.; Jones, M. R.; Yoo, H.; Mirkin, C. A. *Nano Lett.* **2008**, *8* (8), 2526-2529.

118. Jin, R.; Cao, Y.; Mirkin, C. A.; Kelly, K. L.; Schatz, G. C.; Zheng, J. G. *Science* **2001**, *294* (5548), 1901-1903.

119. Lindquist, N. C.; Nagpal, P.; Lesuffleur, A.; Norris, D. J.; Oh, S.-H. *Nano Lett.* **2010**, *10* (4), 1369-1373.

120. Rosen, D. A.; Tao, A. R. *ACS Appl. Mater. Interfaces* **2014**, *6* (6), 4134-4142.

121. Camden, J. P.; Dieringer, J. A.; Wang, Y.; Masiello, D. J.; Marks, L. D.; Schatz, G. C.; Van Duyne, R. P. *J. Am. Chem. Soc.* **2008**, *130*, 12616-12617.

122. Kleinman, S. L.; Frontiera, R. R.; Henry, A.-I.; Dieringer, J. A.; Van Duyne, R. P. *Phys. Chem. Chem. Phys.* **2013**, *15*, 21-36.

123. Kim, J.; Song, X.; Ji, F.; Luo, B.; Ice, N. F.; Liu, Q.; Zhang, Q.; Chen, Q. *Nano Lett.* **2017**, *17* (5), 3270-3275.

124. Köker, T.; Tang, N.; Tian, C.; Zhang, W.; Wang, X.; Martel, R.; Pinaud, F. *Nature Commun.* **2018**, *9* (1), 607.

125. Christopher, P.; Linic, S. *J. Am. Chem. Soc.* **2008**, *130* (34), 11264-11265.

126. Wang, H.; Levin, C. S.; Halas, N. J. *J. Am. Chem. Soc.* **2005**, *127* (43), 14992-14993.

127. Ward, D. R.; Grady, N. K.; Levin, C. S.; Halas, N. J.; Wu, Y.; Nordlander, P.; Natelson, D. *Nano Lett.* **2007**, *7*, 1396-1400.

128. Qin, L.; Zou, S.; Xue, C.; Atkinson, A.; Schatz, G. C.; Mirkin, C. A. *Proc. Natl. Acad. Sci.USA* **2006**, *103*, 13300–13303.

129. Mirkin, C. A.; Letsinger, R. L.; Mucic, R. C.; Storhoff, J. J. *Nature* **1996**, *382*, 607-609.

130. Jain, P. K.; Eustis, S.; El-Sayed, M. A. *J. Phys. Chem. B* **2006**, *110* (37), 18243-18253.

131. Bae, Y.; Kim, N. H.; Kim, M.; Lee, K. Y.; Han, S. W. *J. Am. Chem. Soc.* **2008**, *130* (16), 5432-5433.

132. Jones, M. R.; Mirkin, C. A. *Angew. Chem. Int. Ed.* **2013**, *52* (10), 2886-2891.

133. Scarabelli, L.; Sanchez.-Iglesias, A.; Pérez-Juste, J.; Liz-Marzán, L. M. *J. Phys. Chem. Lett.* **2015**, *6* (21), 4270-4279.

134. Ruditskiy, A.; Xia, Y. *J. Am. Chem. Soc.* **2016**, *138* (9), 3161-3167.

135. Gao, J.; Bender, C. M.; Murphy, C. J. *Langmuir* **2003**, *19* (21), 9065-9070.

136. Millstone, J. E.; Métraux, G. S.; Mirkin, C. A. *Adv. Funct. Mater.* **2006**, *16* (9), 1209-1214.

137. Nosé, S. Mol. Phys. **1984**, *52*, 255-268.

138. Hoover, W. G. *Phys. Rev. A* **1985**, *31*, 1695-1697.

139. Darden, T.; York; D.; Pedersen, L. *J. Chem. Phys.* **1993**, *98*, 10089-10092.

140. Jorgensen, W. L.; Chandrasekhar, J.; Madura, J. D.; Impey, R.W.; Klein, M. L. *J. Chem. Phys.* **1983**, *79*, 926.

141. Wright, L. B.; Freeman, C. L.; Walsh, T. R. *Mol. Simulat.* **2013**, *39* (13), 1093-1102.

142. Abraham, M. J.; Murtola, T.; Schulz, R.; Pall, S; Smith, J. C.; Hess, B.; Lindahl, E. *Software X* **2015**, *1-2*, 19-25.

143. Daura, X., Gademann, K.; Jaun, B.; Seebach, D.; van Gunsteren, W. F.; Mark, A. E. *Angew. Chem. Int. Ed.* **1999**, *38*, 236-240.

144. Rosa, M.; Corni, S.; Di Felice, R. *J. Phys. Chem. C* **2012**, *116*, 21366-21373.

145. Vanderbilt, D. *Phys. Rev. B* **1990**, *41*, 7892-7895.

146. Perdew, J. P.; Burke, K.; Ernzerhof, M. *Phys. Rev. Lett.* **1996**, *77*, 3865-3868.